Single atoms on demand for cavity QED experiments

Dissertation

zur

Erlangung des Doktorgrades (Dr. rer. nat.)

der

Mathematisch-Naturwissenschaftlichen Fakultät

der

Rheinischen Friedrich-Wilhelms-Universität Bonn

vorgelegt von

Igor Dotsenko

aus

Cherkassy (Ukraine)

Bonn 2007

Angefertigt mit Genehmigung der Mathematisch-Naturwissenschaftlichen Fakultät

der Rheinischen Friedrich-Wilhelms-Universität Bonn

1. Referent: Prof. Dr. Dieter Meschede
2. Referent: Prof. Dr. Leonid Yatsenko

Tag der Promotion: 22.05.2007

Diese Dissertation ist auf dem Hochschulschriftenserver der ULB Bonn
`http://hss.ulb.uni-bonn.de/diss_online/` elektronisch publiziert

Abstract

Cavity quantum electrodynamics (cavity QED) describes electromagnetic fields in a confined space and the radiative properties of atoms in such fields. The simplest example of such system is a single atom interacting with one mode of a high-finesse resonator. Besides observation and exploration of fundamental quantum mechanical effects, this system bears a high potential for applications quantum information science such as, e.g., quantum logic gates, quantum communication and quantum teleportation.

In this thesis I present an experiment on the deterministic coupling of a single neutral atom to the mode of a high-finesse optical resonator. In Chapter 1 I describe our basic techniques for trapping and observing single cesium atoms. As a source of single atoms we use a high-gradient magneto-optical trap, which captures the atoms from background gas in a vacuum chamber and cools them down to millikelvin temperatures. The atoms are then transferred without loss into a standing-wave dipole trap, which provides a conservative potential required for experiments on atomic coherence such as quantum information processing and metrology on trapped atoms. Moreover, shifting the standing-wave pattern allows us to deterministically transport the atoms (Chapter 2). In combination with non-destructive fluorescence imaging of individual trapped atoms, this enables us to control their position with submicrometer precision over several millimeters along the dipole trap.

The cavity QED system can distinctly display quantum behaviour in the so-called strong coupling regime, i.e., when the coherent atom-cavity coupling rate dominates dissipation in the system. This sets the main requirements on the resonator's properties: small mode volume and high finesse. Chapter 3 is devoted to the manufacturing, assembling, and testing of an ultra-high finesse optical Fabry-Perot resonator, stabilized to the atomic transition. In Chapter 4 I present the transportation of single atoms into the cavity and their coupling to the cavity mode. The strong coupling manifests itself in a strong reduction of the cavity transmission probed by a weak external laser. The atoms remain trapped and coupled to the cavity mode for several seconds until we move them out of the cavity for final analysis of their number and position.

Parts of this thesis have been published in the following journal articles:

1. Y. Miroshnychenko, D. Schrader, S. Kuhr, W. Alt, I. Dotsenko, M. Khudaverdyan, A. Rauschenbeutel, and D. Meschede, *Continued imaging of the transport of a single neutral atom*, Optics Express **11**, 3498 (2003)

2. I. Dotsenko, W. Alt, M. Khudaverdyan, S. Kuhr, D. Meschede, Y. Miroshnychenko, D. Schrader, and A. Rauschenbeutel, *Submicrometer position control of single trapped neutral atoms*, Physical Review Letters **95**, 033002 (2005)

3. L. Förster, W. Alt, I. Dotsenko, M. Khudaverdyan, Y. Miroshnychenko, D. Meschede, S. Reick, and A. Rauschenbeutel, *Number-triggered loading and collisional redistribution of neutral atoms in a standing wave dipole trap*, New Journal of Physics **8**, 259 (2006)

Contents

List of Figures

List of Tables

Introduction

In 1946 Edward Purcell noticed that the rate of spontaneous emission of an atom can be significantly enhanced by coupling it to an electrical circuit resonant with the atomic radio-frequency transition [1]. This publication gave birth to a new field of research – cavity quantum electrodynamics (CQED), which describes the electromagnetic field in a confined space and the radiative properties of atoms in such field. Obviously, one of the simplest systems in the scope of CQED is a single atom interacting with a single photon in a cavity. The theory describing this system was first developed by Jaynes and Cummings in 1963 [2], providing the most basic model to CQED experiments.

The main obstacles in the experimental realization of a coupled atom-cavity system are spontaneous emission of the atom and damping of the cavity field. Thus, the most relevant regime for observing quantum phenomena of the atom-field dynamics is reached when the strength of the coherent atom-field coupling exceeds these dissipations. Fortunately, the tremendous progress in controlling single atoms as well as in manufacturing high-finesse cavities accomplished over the last 15 years has allowed experimentalists to achieve the strong coupling with single atoms in cavities in two spectral domains. At microwave frequencies highly excited Rydberg atoms are coupled to the field of a superconducting cavity with a very high Q-factor while crossing the cavity mode one by one [3, 4]. Strong coupling in the optical domain has been reached using ultra-cold ground-state atoms and cavities with small mode volume [5, 6].

About 10 years ago a particular interest in CQED systems arouse due to their possible applications in quantum information processing [7], where quantum concepts can lead to dramatic speed up in solving certain classes of computational problems, such as prime factoring [8] and database search [9]. Using individual atoms as carriers of quantum information (qubits), two-qubit logic operations can be performed in a cavity by the coherent exchange of cavity photon between the atoms [10]. Since a cavity emits in a well-defined mode and a radiated photon carries information on an atom, CQED systems could also be efficiently used for building quantum logic network [11]. Here, a photon emitted by the cavity transfers quantum information between qubits located at spatially separated nodes of a network.

Besides strong coupling, one of the most important requirement for using CQED systems for quantum information processing is permanent localization of single atoms in the cavity. The required degree of confinement can be provided with ions in ion traps [12]. Single neutral atoms can be trapped inside the cavity by using intra-cavity dipole traps [13], external dipole traps [14], or near-resonant cavity fields [15, 16]. Besides two-qubit

quantum gates, the realization of a quantum computer also requires the ability to initialize and to measure the states of the qubits [17]. We have already demonstrated that a string of neutral atoms stored in a standing-wave dipole trap can serve as a quantum register, where atomic qubits can be individually addressed and coherently manipulated much faster than the relevant decoherence times [18]. Besides, we are able to transport the atoms over several millimeters while partly retaining (single-atom) quantum coherence [19].

Till recently the two basic approaches to deliver single ground-state atoms into a cavity have been either to let them freely fall from a magneto-optical trap (MOT) [20], or to eject them from below by means of an atomic fountain [21]. In order to increase the efficiency of the atom delivery, one can use a dipole trap beam for guiding atoms between a MOT and a cavity while confining them transversally [22, 14]. Recently, the submicron positioning of single atoms inside a microcavity has been demonstrated using a standing-wave trap [14]. However, this experiment does provide neither the possibility to prepare quantum states of atoms before placing them into the cavity nor to analyze their final states.

In this thesis I present an experiment on the deterministic coupling of a single neutral atom to a mode of a high-finesse optical resonator. A desired number of ultra-cold cesium atoms (from 1 to 20) is prepared in a MOT and then transferred without loss into a standing-wave dipole trap. This trap provides a conservative potential required for experiments on quantum information as well as a tight confinement of atoms. Our approach for controlling the position of individual atoms is based on the "optical conveyor belt" technique [23, 24]. Combining it with fluorescence imaging of single trapped atoms, I have measured and controlled their position with submicrometer precision [25, 26]. The optical cavity I have assembled is composed of two mirrors of high reflectivity placed close to each other and is stabilized to the atomic transition. A finesse of about a million and a small mode volume enable us to operate the atom-cavity system in the strong-coupling regime. I was able to couple single atoms to the cavity mode on demand. Together with the possibility to prepare their initial states as well as to analyze their final states, this work represents an important step towards deterministic quantum computing with neutral atoms [27].

Chapter 1

Trapping and observing single atoms

1.1 Introduction

To perform any experiment on single atoms we need a set of tools providing a necessary degree of control over them. Moreover, the atoms should be well isolated from environment, which, permanently probing the atom system, would lead to its decoherence and thus would complicate the study of any coherent process. A widely used approach overcoming this problem is to experiment with atoms in vacuum or in dilute gases instead of in and on solids or liquids. However, high velocities at room or even cryogenic temperatures prevent long observation times of flying atoms.

The great breakthrough in atom studies has been made with the invention of laser cooling [28, 29, 30] and magneto-optical trapping of atoms [31]. This allowed not only cooling of atomic species to sub-millikelvin temperatures but also storing them for many seconds and even minutes. The creation of Bose-Einstein condensate became the triumph of these developments [32, 33]. However, although a magneto-optical trap (MOT) allows us to efficiently capture, cool, and store even single atoms [34, 35, 36], it does not completely solve the problem of the isolation of atoms from the environment and does not allow us to store atoms in a specific quantum state since the operation of the MOT is based on nearly-resonant scattering of the MOT lasers.

In contrast to MOTs, conservative dipole traps rely on off-resonant interaction of polarizable particles with the laser field [37, 38] resulting in low light scattering. Also known as optical tweezers [39], they are successfully used in different research areas ranging from biology to nanofabrication for the precise manipulation of various dielectric particles: from microspheres and biological cells to DNA and single atoms. Another application of dipole traps is to form optical lattices by the interference of laser beams. They are extensively used for studying quantum gases [40], in quantum information processing [41], in metrology [42], etc. We have experimentally shown that a standing-wave dipole trap preserves the atomic coherence [19] and can be used as a holder of a quantum register for storing quantum information [18].

Spatial information on trapped atoms is essential for realizing complete control over them. The observation of atoms in optical and magnetic traps is typically performed via fluorescence imaging, in contrast to, e.g., atomic force and scanning tunnelling microscopy used for imaging atoms on surfaces of solids [43]. The first image of an individual atomic particle in a trap was obtained by recording the fluorescence from a single barium ion [44]. Nowadays we are able to non-destructively observe individual neutral atoms in the dipole trap for more than a minute [45].

1.2 A single-atom magneto-optical trap

The considerable progress in atomic physics observed over the last two decades would have hardly been possible without the invention of the laser cooling techniques allowing us to slow down, cool, and even Bose condense atomic gases. Proposed about 30 years ago by T. Hänsch and A. Shawlow [28], the three-dimensional laser cooling of atoms has been first experimentally realized by S. Chu [30] in 1985. By adding an inhomogeneous magnetic field, resulting in a position-dependent radiation pressure, the first magneto-optical trapping of atoms has been demonstrated two years later [31]. Since then, magneto-optical traps became a widely used tool for cooling atoms down to sub-millikelvin temperatures and keeping them trapped for long times. We use a specially designed MOT as a source of single cold cesium atoms for our experiments. The high-gradient magnetic field assists us in trapping single or few atoms, whereas the MOT fluorescence allows us to infer their exact number in real time.

1.2.1 Principle of operation

The MOT's speciality is the simultaneous cooling and trapping of neutral atoms [46, 47]. Its operation relies on a velocity-dependent cooling force and a position-dependent restoring force providing spatial confinement of the atoms. The cooling is realized by three orthogonal pairs of counter-propagating laser beams which are slightly red-detuned from the atomic transition frequency. An atom moving at the intersection of the beams preferentially absorbs photons from the beam opposite to its direction of motion, frequency of which is Doppler-shifted closer to the atomic resonance. Since the subsequent spontaneous emission is in random direction, it does not change the average momentum of the atom and the total momentum transfer from the laser field to the atom is opposite to the direction of the atomic motion. Therefore this configuration of the laser beams called "optical molasses" results in an effective friction force cooling the atom.

Even at rest, the atom is continuously excited by the near-resonant laser field followed by photon emission in a random direction causing atom heating. The equilibrium temperature between the molasses cooling and the heating by the spontaneous emission is called the Doppler temperature and is given by

$$T_{\mathrm{D}} = \frac{\hbar\,\Gamma}{2k_{\mathrm{B}}}\ , \tag{1.1}$$

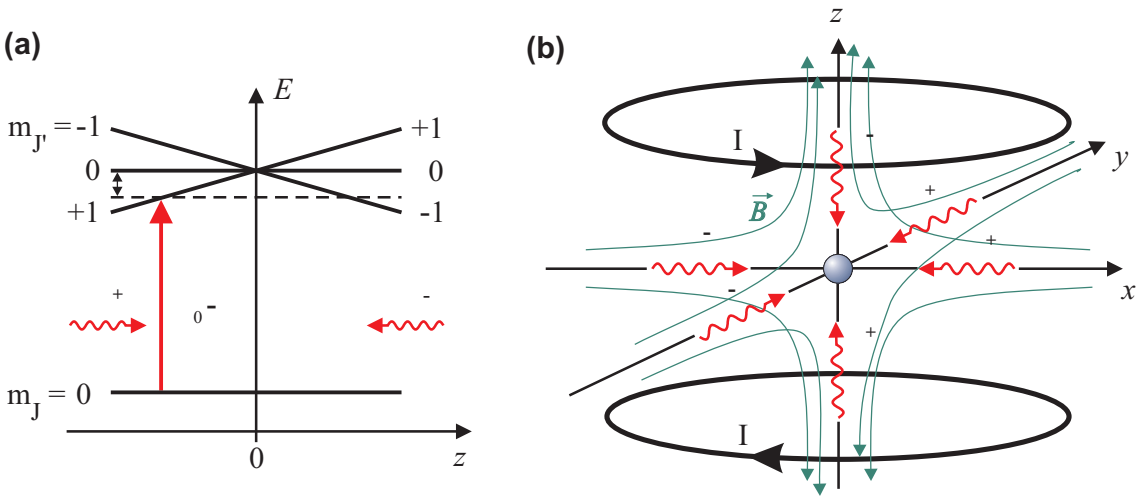

Figure 1.1: Principle of operation of a magneto-optical trap. (a) Simplified level scheme of an atom interacting with two counter-propagating red-detuned laser beams with opposite circular polarization. The linear magnetic field gradient lifts the degeneracy of the excited state. If the atom is displaced from the trap center, it becomes resonant with the laser beam pushing it back to the zero of the field. (b) A three-dimensional MOT uses a pair of coils in anti-Helmholtz configuration producing a quadrupole field and a three-dimensional optical molasses.

where Γ is the spontaneous emission rate from the excited state and k_B is the Boltzmann constant. For a cesium atom, $\Gamma = 2\pi \times 5.22$ MHz and $T_D = 125\,\mu$K.

Trapping of atoms at a specific position requires a position-dependent force. For this purpose a quadrupole magnetic field is added which vanishes at the center of the optical molasses and increases linearly in all directions. The magnetic field lifts the degeneracy of the upper level with respect to the Zeeman sublevels resulting in a level splitting proportional to the distance of the atom to the magnetic zero point, i.e. the trap center. This is illustrated in Fig. 1.1(a) in one dimension for the case of a $J = 0 \leftrightarrow J' = 1$ transition. If the red-detuned counter-propagating laser beams have opposite circular polarizations, a stationary atom displaced from the zero point is shifted closer into resonance with that laser beam which pushes it back to the center. Thus, the atom experiences a restoring force to the trap center. This principle can be easily generalized to the three-dimensional case shown in Fig. 1.1(b). As a result, the radiation force in the MOT simultaneously pushes the atom to the center of the MOT and cools it there. Moreover, the multi-level structure of the atom can allow sub-Doppler cooling mechanisms resulting in temperatures lower than T_D [48, 49], which will be not discussed here.

1.2.2 Experimental setup

The first single-atom MOT in our group was constructed in 1996 [36]. The details of the modified MOT setup permitting more flexibility in the observation and manipulation of the atoms have been described extensively in previous theses of the group [50, 51]. Here, I

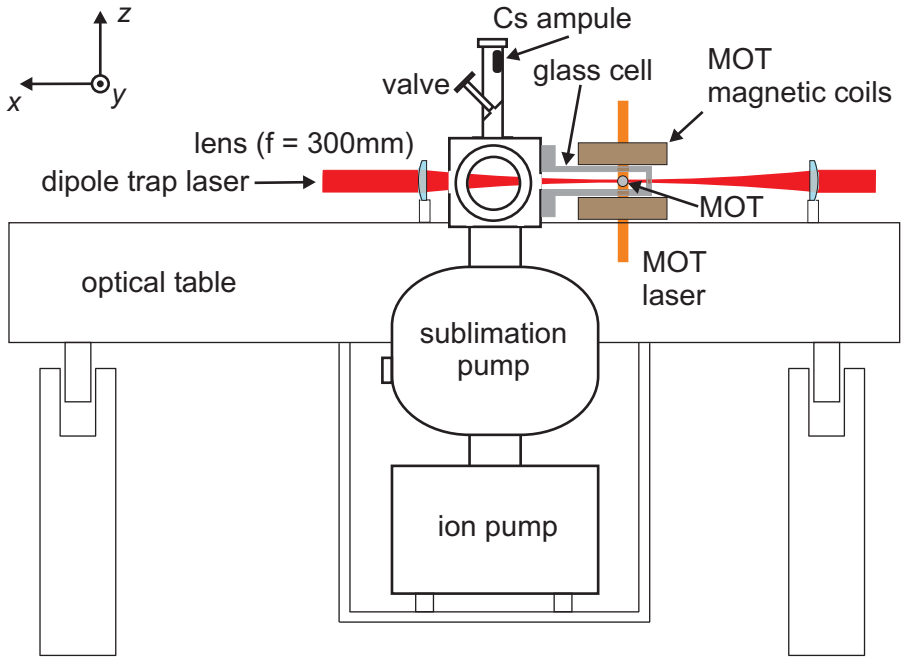

Figure 1.2: Side view of an optical table with the vacuum system and the optical traps.

only present the most important components which are relevant for this thesis. The basic experimental setup is schematically shown in Figs. 1.2 and 1.4.

Vacuum system

Our vacuum system fulfills two main requirements for experimenting with trapped atoms: It provides an ultra-high vacuum guaranteeing long storage times and permits optimal optical access from outside for flexible observation and manipulation of atoms. All our experiments are performed inside a compact $3 \times 3 \times 12.5\,\mathrm{cm}^3$ glass cell with 5 mm thick walls, see Fig. 1.2. It is connected to the vacuum steel cube to which the pumps and the cesium reservoir are attached. The constantly operating ion pump provides an ultra-high vacuum in the glass cell with a pressure of less than 10^{-10} mbar. An additional titanium sublimation pump is mainly used for reaching the initial low pressures inside the newly closed vacuum chamber, e.g., after installation of a cavity inside the cell, see Sec. 3.3.1.

Laser system

In contrast to the simplified level structure used in Fig. 1.1(a), the D_2 transition in a cesium atom used for cooling and trapping has a rich spectrum, schematically shown in Fig. 1.3. As the MOT cooling transition we use the cycling transition $F = 4 \rightarrow F' = 5$. Since the atom can be off-resonantly excited to the $F' = 4$ level, from where it may spontaneously decay into the $F = 3$ ground state, we apply an additional repumping laser resonant with the transition $F = 3 \rightarrow F' = 4$ to pump the atom back into the cooling cycle.

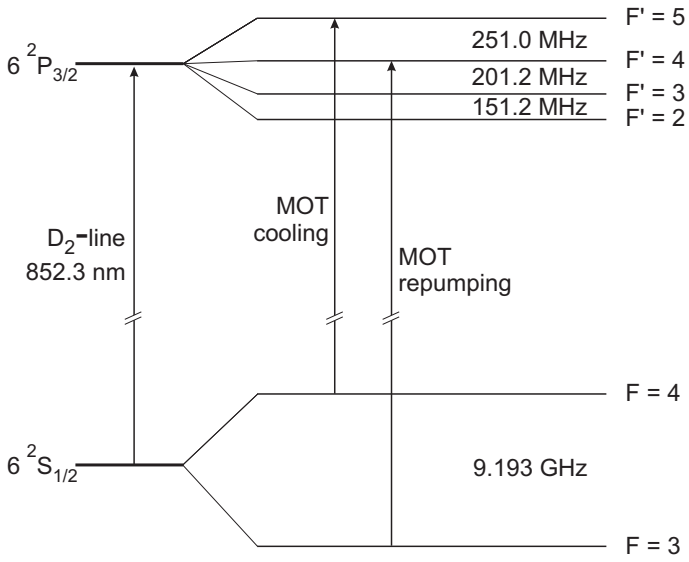

Figure 1.3: Hyperfine structure of the cesium D_2 transition. Shown are the transitions used for cooling and repumping in the MOT.

Both cooling and repumping lasers are diode lasers set up in Littrow configuration [52]. Their frequencies are actively stabilized onto atomic resonance frequencies by polarization spectroscopy [51]. The probe laser is locked to the crossover transition $F = 4 \rightarrow F' = 3/5$, which is red-detuned by -225 MHz from the cycling transition. An acousto-optic modulator (AOM) in double pass configuration shifts the laser frequency by 2×110 MHz towards the atomic resonance. As a result, the cooling laser is red-detuned from the cooling transition by approximately Γ, which is required for optimal Doppler cooling. In addition, this AOM is also used to control the laser power and frequency for illuminating atoms in the dipole trap, see Sec. 1.5. The repumping laser is directly stabilized to the $F = 3 \rightarrow F' = 4$ transition.

Both lasers with their spectroscopies are set up on a separate optical table, and we use optical fibers to transfer the laser light to the main table, shown in Fig. 1.2. Here, the cooling laser is split into three beams, which are shined from three different direction into the center of the quadrupole field and then retro-reflected. Thus, the six beams intersect in one point in the glass cell providing a 3-D optical molasses. The beam diameter is about 2 mm with a typical power of $100 - 200\,\mu$W per beam. The MOT repumping laser is linearly polarized and is shined into the MOT along the glass cell.

Magnetic coils

The high field gradient of the MOT is produced by a pair of water cooled magnetic coils, set in anti-Helmholtz configuration along the z axis and placed above and below the glass cell, see Fig. 1.2. In all experiments described in this thesis we use a gradient of $\partial B/\partial z = 300$ G/cm provided by a current of 15 A, which can be switched on and off within about 30 ms.

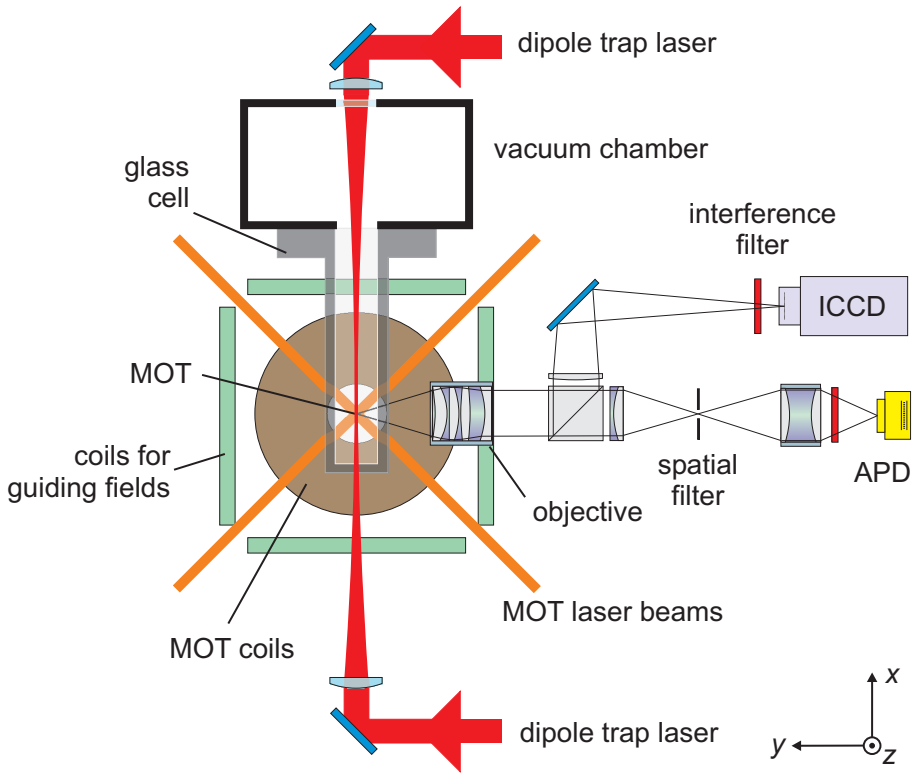

Figure 1.4: Schematic experimental setup of MOT, dipole trap, and imaging system (top view). The MOT consists of three pairs of counter-propagating laser beams and the coil pair (along z) providing the quadrupole field. Both dipole trap lasers are focussed into the MOT in the center of the glass cell. The fluorescence light from the MOT is collected and collimated by imaging optics. One part is spatially and spectrally filtered and focussed onto an avalanche photodiode (APD), the other part is sent to an intensified CCD camera (ICCD) after spectral filtering. Three pairs of orthogonal coils are used for applying guiding magnetic fields. Beams and coils along z direction are not shown.

Three orthogonal pairs of coils placed around the glass cell, see Fig. 1.4, compensate DC-magnetic fields in three dimensions. In addition, they are used for applying guiding magnetic fields of up to several Gauss used in Sec. 4.5.5.

1.2.3 Fluorescence detection of single atoms

To observe the trapped atoms in the MOT we use two detectors, see Fig. 1.4. An avalanche photodiode (APD) operated in single-photon counting mode allows us to determine their exact number and an intensified CCD camera (ICCD) provides spatial information. In order to efficiently collect and collimate extremely low levels of fluorescence light from single trapped atoms we use a home-built diffraction-limited objective with a numerical aperture of NA = 0.29 [53]. The collimated light is then equally divided into two parts by a beam-splitter: the reflected part is imaged onto the ICCD with a magnification of about

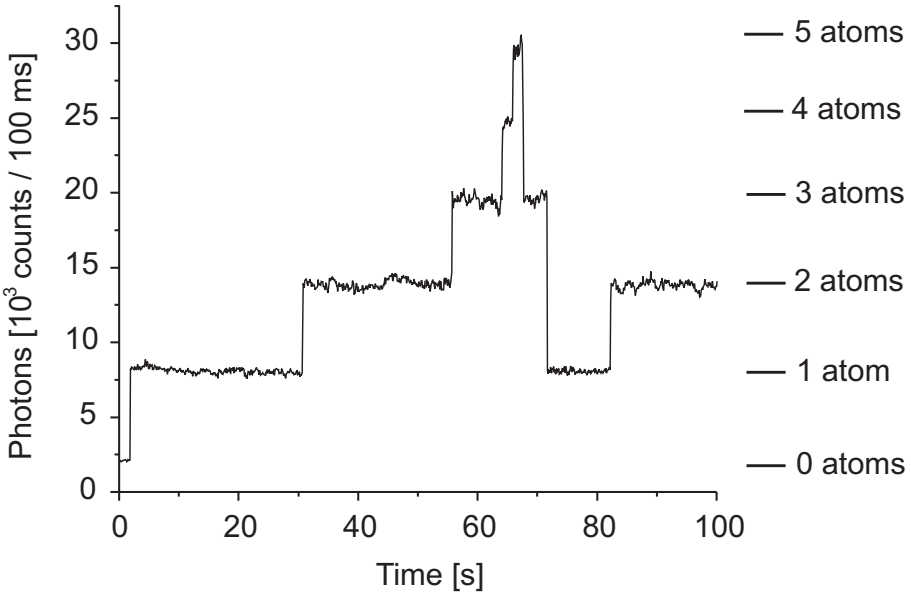

Figure 1.5: APD signal of the MOT fluorescence. Each trapped atom contributes the same amount of fluorescence to the signal, allowing us to determine their exact number. When an atom enters or leaves the trap, the count rate instantaneously increases or decreases accordingly.

14.0 (see Sec. 1.5) and the transmitted light is focused onto the APD (EG&G, model SPCM-200). To reduce the stray light background, the collected light is spectrally filtered by an interference filter. In addition, the light sent to the APD is filtered spatially with a pinhole. By taking into account the numerical aperture of the objective, the transmission of the interference filter, and the quantum efficiency of the APD, the overall detection efficiency with the APD is $\eta = 8 \times 10^{-3}$. Typically, we obtain a count rate of $3 \times 10^4\,\mathrm{s}^{-1}$ per atom.

A typical APD signal of the MOT fluorescence is shown in Fig. 1.5. The step-like form of the count rate indicates the instantaneous capture and loss of the atoms. Since each atom contributes the same amount of fluorescence to the APD signal, we can use the MOT fluorescence to infer the exact number of trapped atoms within typically 20 ms.

1.3 A standing-wave optical dipole trap

Optical dipole traps rely on the electric dipole interaction of polarizable particles (e.g., neutral atoms) with far-detuned light. The corresponding dipole force arises from the interaction of the induced dipole moment with the gradient of the light field [54]. Since the optical excitation in these traps can be kept very low, they provide a nearly conservative trapping potential favourable for experiments on quantum state manipulation. We use a standing-wave configuration of the dipole trap providing tight axial confinement of atoms and allowing their position control.

1.3.1 Dipole potential

There are several different approaches to treat the dipole force [38]. Here I recall only the classical model, which provides a simple description of the dipole interaction and its basic properties, namely the dipole potential and the scattering rate, relevant to our experiments. The predictions of this model are good approximations to the exact solution given by the quantum-mechanical treatment.

In the following we consider an atom as a charged harmonic oscillator driven by a classical electromagnetic field $\mathbf{E}(t) = \mathbf{E}_0 \exp(-i\omega t) + \text{c.c.}$ Given α the atomic polarizability, the field induces an electric dipole moment $\mathbf{d}(t) = \alpha \mathbf{E}(t)$ which evolves according to the equation of motion

$$\ddot{\mathbf{d}}(t) + \Gamma \dot{\mathbf{d}}(t) + \omega_0^2 \mathbf{d}(t) = \frac{e^2}{m_e} \mathbf{E}(t). \tag{1.2}$$

Here, m_e and e are the mass and the charge of the electron, ω_0 is the atomic resonance frequency, and Γ is the damping rate due to the radiative energy loss given by

$$\Gamma = \frac{e^2 \omega^2}{6\pi \epsilon_0 m_e c^3} \ . \tag{1.3}$$

Integration of equation (1.2) yields the complex polarizability depending on the driving frequency

$$\alpha(\omega) = \frac{e^2}{m_e} \frac{1}{\omega_0^2 - \omega^2 - i\omega\Gamma} \ . \tag{1.4}$$

The dipole potential is the interaction energy of the induced dipole moment and the electric field given by

$$U_{\text{dip}}(\boldsymbol{r}) = -\frac{1}{2} \langle \mathbf{d} \cdot \mathbf{E} \rangle = -\frac{1}{2\epsilon_0 c} \text{Re}(\alpha) I(\boldsymbol{r}) \tag{1.5}$$

where the angular brackets denote the time average over one oscillation period and the field intensity is $I(\mathbf{r}) = 2c\epsilon_0 |\mathbf{E}_0|^2$. The dipole trap depth is thus proportional to the intensity $I(\boldsymbol{r})$ and to the real part of the polarizability, which describes the in-phase component of the atomic dipole moment. The dipole force results from the gradient of the interaction potential $\mathbf{F}_{\text{dip}}(\mathbf{r}) = -\nabla U_{\text{dip}}(\mathbf{r})$.

The scattering rate is determined by the amount of power absorbed from the driving field, $P_{\text{abs}}(\mathbf{r})$, divided by the energy per photon, $\hbar\omega$:

$$R_{\text{sc}}(\mathbf{r}) = \frac{P_{\text{abs}}(\mathbf{r})}{\hbar\omega} = \frac{\langle \dot{\mathbf{d}} \cdot \mathbf{E} \rangle}{\hbar\omega} = \frac{1}{\hbar\epsilon_0 c} \text{Im}(\alpha) I(\mathbf{r}). \tag{1.6}$$

In the regime of large detuning $|\omega - \omega_0| \gg \Gamma$ equations (1.5) and (1.6) can be approximated by

$$U_{\text{dip}}(\mathbf{r}) = \frac{\hbar\Gamma}{8} \frac{\Gamma}{\Delta'} \frac{I(\mathbf{r})}{I_0} , \tag{1.7}$$

$$R_{\text{sc}}(\mathbf{r}) = \frac{\Gamma}{8} \left(\frac{\Gamma}{\Delta'} \right)^2 \frac{I(\mathbf{r})}{I_0} \tag{1.8}$$

$$= \frac{\Gamma}{\hbar\Delta'} U_{\text{dip}}(\mathbf{r}) . \tag{1.9}$$

where

$$\frac{1}{\Delta'} = \frac{1}{\omega - \omega_0} + \frac{1}{\omega + \omega_0} \,. \tag{1.10}$$

and I_0 is the saturation intensity given by

$$I_0 = \frac{\pi h \Gamma c}{3\lambda^3} \,. \tag{1.11}$$

In the case of a cesium atom, $I_0 = 11\,\mathrm{W/m^2}$. If the light detuning from the atomic resonance, $\Delta = \omega - \omega_0$, is much smaller than the atomic frequency, we can apply the rotating-wave approximation and neglect the term with the sum of optical frequencies $\omega + \omega_0$ in equation (1.10) leading to $\Delta' \approx \Delta$.

If the dipole trap laser is red-detuned from the atomic resonance, i.e. $\Delta < 0$, the dipole potential given by equation (1.7) is negative, so that the atom is attracted to the regions of high light intensities. For the case of a blue-detuned laser ($\Delta > 0$), the interaction energy is positive and thus the atoms are repelled from the light field. The relation (1.9) shows that the scattering rate can be minimized by using large laser detunings while compensating the decreasing trap depth by higher light intensities.

1.3.2 Multi-level cesium atom

The classical model does not take into account the atomic multi-level structure. Still, we can independently apply the classical treatment to each individual transition and add up the outcomes weighted with the corresponding transition's oscillator strength [51]. As a result, considering both contributions from the D_1 and D_2 transitions of a cesium atom (see Fig. A.1), we can introduce the "effective" laser detuning

$$\frac{1}{\Delta_{\mathrm{eff}}} = \frac{1}{3}\left(\frac{1}{\Delta_{\mathrm{D1}}} + \frac{2}{\Delta_{\mathrm{D2}}}\right) \tag{1.12}$$

and still use expressions (1.7) and (1.8) for calculating the trap depth and the scattering rate after replacing Δ' by Δ_{eff}.

A full quantum mechanical treatment of a cesium atom in a far-detuned dipole trap, which takes into account atomic fine, hyperfine, and Zeeman states (see Appendix A for the relevant states of cesium), can be found in Ref. [55]. It provides ac Stark shifts (also called "light shifts") for each atomic level depending on the polarization of the laser light.

1.3.3 Standing-wave trap

A widely used geometric configuration of dipole traps is based on a single strongly focused laser beam. To achieve a tighter trap confinement, we use a standing-wave dipole trap formed by the interference of two counter-propagating laser beams. The beams have equal intensities, equal optical frequencies, and parallel linear polarizations. Neglecting the Guoy phase and the curvature of the wavefronts of the Gaussian beams, the resulting dipole potential is

$$U(x,y,z) = -U_0 \frac{w_0^2}{w^2(x)} \exp\left[-\frac{2(y^2+z^2)}{w^2(x)}\right] \cos^2\left(\frac{2\pi}{\lambda}x\right), \tag{1.13}$$

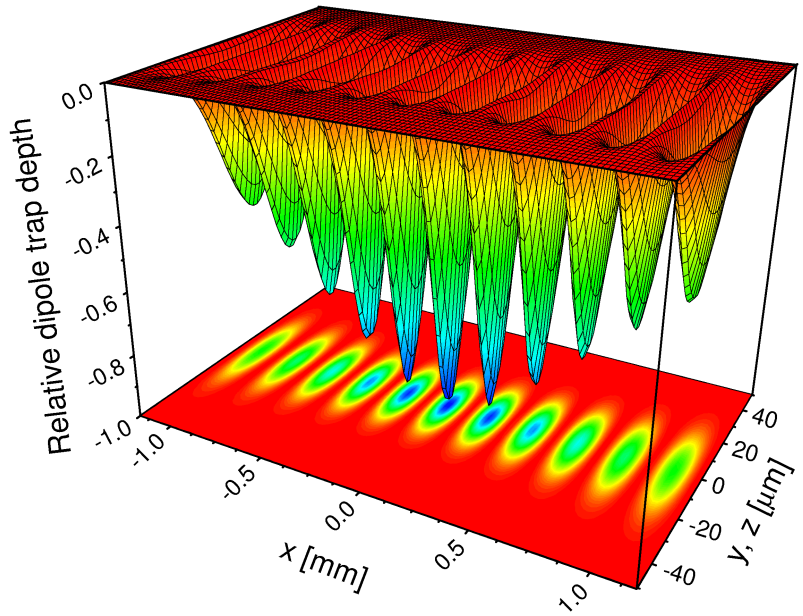

Figure 1.6: Three-dimensional view of the standing-wave dipole potential for the beam waist of $w_0 = 19\,\mu$m. In x-direction, the wavelength has been stretched by a factor of 400 to show the individual potential wells where atoms can be trapped.

with the beam waist w_0, the beam radius $w(x) = w_0(1 + x^2/z_\mathrm{R}^2)^{1/2}$, and the Rayleigh range $z_\mathrm{R} = \pi w_0^2/\lambda$. Here we consider the standing wave to be oriented along x direction. The maximum trap depth reads

$$U_0 = \frac{\hbar\Gamma}{8}\frac{I_\mathrm{max}}{I_0}\frac{\Gamma}{|\Delta_\mathrm{eff}|}\,, \tag{1.14}$$

where the peak intensity is

$$I_\mathrm{max} = \frac{4P}{\pi w_0^2} \tag{1.15}$$

with P the total optical power of the beams. Figure 1.6 shows the trapping potential for $w_0 = 19\,\mu$m.

Being trapped in the dipole trap, an atom oscillates inside its potential wells in both axial and radial directions. If the atomic temperature is much smaller than the trap depth, the trapping potential can be approximated by a harmonic one resulting in the respective oscillation frequencies

$$\Omega_\mathrm{ax} = 2\pi\sqrt{\frac{2U_0}{m\lambda^2}}\,, \tag{1.16}$$

$$\Omega_\mathrm{rad} = \sqrt{\frac{4U_0}{mw_0^2}}\,, \tag{1.17}$$

where m denotes the atomic mass of cesium.

1.3.4 Experimental setup

Nd:YAG laser

In all previous experiments with the standing-wave dipole trap performed in our group [50, 51, 55] as well as in Chapter 2 of this thesis we have used a Nd:YAG laser as a dipole trap laser. It is an industrial, high power cw laser (Quantronix, model 116EF-OCW-10) with a wavelength of $\lambda = 1064$ nm and a maximum output power of 10 W. The output light has linear polarization and a Gaussian TEM_{00} transverse mode profile. The laser operates on 4–5 longitudinal modes with a spacing of 196 MHz. This corresponds to a coherence length of about 30 cm ensuring a high-contrast interference pattern of the standing-wave dipole trap inside the glass cell.

The output beam is split into two parts, which are then focused to the MOT center from opposite sites, as shown in Fig. 1.4. Typically we get 2 W of total optical power inside the glass cell. The beam waist of 19 μm and the trap depth of $U_0/k_\mathrm{B} = 0.8$ mK are inferred by measuring the oscillation frequencies of the trap [55]: $\Omega_\mathrm{ax} = 2\pi \times (265 \pm 8)$ kHz for $P_\mathrm{YAG} = 1.56$ W and $\Omega_\mathrm{rad} = 2\pi \times (3.6 \pm 0.2)$ kHz for $P_\mathrm{YAG} = 1.8$ W. The measured U_0 is only about 40 % of that expected from equation (1.7). This discrepancy can be explained by aberrations and diffraction in the dipole trap optics increasing the beam waist and decreasing the beam power. The scattering rate at the trap minimum of $R_\mathrm{sc} = 9\,\mathrm{s}^{-1}$ is directly obtained from the trap depth according to equation (1.9).

Yb:YAG laser

The old Nd:YAG laser has served us well during many years. However, our new experiments set more stringent requirements on the dipole trap laser. For instance, we have observed that the multi-mode structure of the Nd:YAG laser complicates the illumination of atoms (see Sec. 1.5). Besides, if using beams with a larger Rayleigh range necessary for transporting atoms over 5 mm distance into the cavity (see Sec. 3.4), the reduced beam intensity should be compensated by the increased power of the dipole trap laser in order to keep the trap depth reasonably large.

To get more optical power, we have replaced the Nd:YAG laser by an Yb:YAG disc laser (ELS, model VersaDisk-1030-10-SF) with a wavelength of $\lambda = 1030$ nm and a maximum output power of about 25 W, which was then used in all experiments in Chapters 3 and 4. However, before using the laser, we have slightly modified it to provide continuous single-mode operation and a higher temperature stability. The modifications have included water cooling of the whole laser head, the utilization of a scanning Fabry-Perot interferometer for monitoring the mode structure of the laser in real time, and the installation of a motorized holder for the outcoupling mirror allowing us to adjust the laser resonator without opening the laser cover each time when mode hopping is detected. As a result, the laser emits a single longitudinal mode with a stable output power of about 20 W, resulting in up to 5 W laser power in each DT beam before the glass cell. The modified dipole trap geometry adapted for the cavity experiments is described in Sec. 3.4 in connection with the cavity properties.

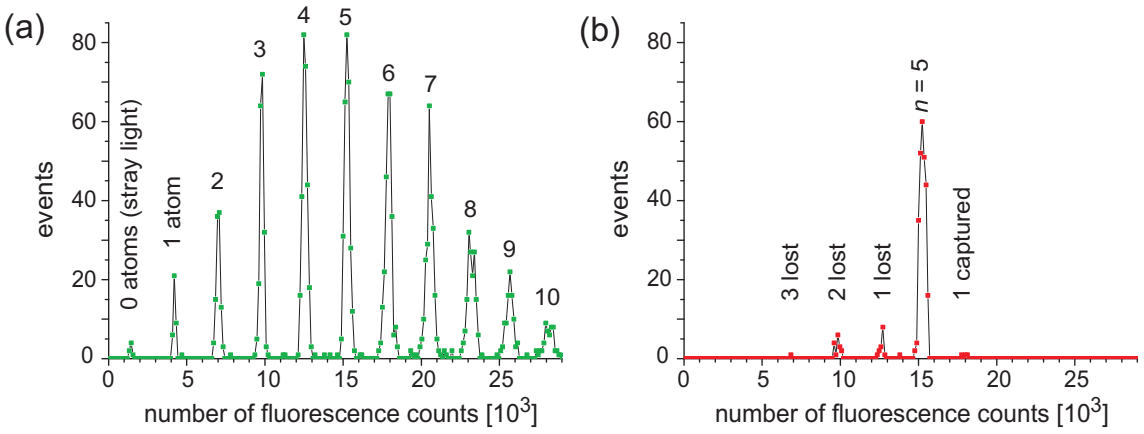

Figure 1.7: Histograms of fluorescence counts from the MOT integrated over 60 ms (bin size: 120 counts). Each peak corresponds to a specific number of trapped atoms. In panel (a), the fluorescence was measured directly after loading the MOT with five atoms on average. The actual number of atoms in the MOT follows Poissonian statistics to a good approximation, leading to the observed distribution of peak areas. For events where the software discriminator detected five atoms in the MOT, the atoms were transferred to the DT. These atoms were counted by transferring them back to the MOT where the fluorescence was measured a second time, leading to the final histogram in panel (b).

1.4 Loading of the DT with atoms

Transferring atoms between traps

The dipole trap is loaded with cold atoms from the MOT. For this purpose, both traps are simultaneously operated for several tens of milliseconds before we switch off the MOT. To transfer the atoms back into the MOT at the end of an experimental sequence, e.g., for counting them, we use the reverse procedure. Since the presence of the dipole trap shifts the atomic resonance, we change the parameters of the MOT cooling beams (power and frequency) by means of the AOM in order to better cool the atoms into the DT during their transfer. For small numbers of atoms (up to about 5) the transfer efficiency is better than 99 %. For larger atom numbers cold collisions between atoms occasionally loaded into the same potential well lead to their loss, thus reducing the transfer efficiency [56].

Number-triggered loading

The loading of the MOT is a statistical Poissonian process. Therefore, we cannot predict the exact number of atoms which will be trapped in the MOT and then transferred into the DT. However, in some applications it is necessary to have a predetermined number of atoms in the trap. For this purpose, we have developed a computer-controlled loading sequence that monitors the atom number via the MOT fluorescence level [56]. If the atom number is the desired one, the atoms are transferred into the DT and the main experimental sequence is started. If not, they are ejected from the MOT and the MOT is

reloaded. The whole "number-triggered loading" procedure runs in a fully automated way allowing us to perform the same experimental sequence many times with a preset initial number of atoms.

In order to correctly determine the number of trapped atoms, we integrate the MOT fluorescence (Fig. 1.5) over 60 ms. The corresponding histogram of fluorescence counts is shown in Fig. 1.7(a). Here, the MOT parameters are optimized to load on average 5 atoms. Each peak corresponds to a specific number of trapped atoms. As an example, Fig. 1.7(b) demonstrates the preparation of 5 atoms in the DT. To verify the atom number actually prepared in the DT, we transfer the atoms back into the MOT and count them again. The peak corresponding to five atoms comprises 88 % of all events. We define this percentage as the preparation efficiency for five atoms. In the other events, atoms have been lost or an additional atom has been captured.

To avoid the post-selection of experimental shots started with only one atom and to speed up data acquisition, we perform all experiments on transporting single atoms into the cavity, described in Sec. 4.5, with the number-triggered loading of the DT with one atom (the preparation efficiency of 97(±1) %). More details on the presented loading technique are described extensively in Ref. [56].

A similar feedback technique has been proposed in Ref. [57] for loading the MOT with single chromium atoms. Here, the MOT loading is actively suppressed or enhanced depending on the actual number of trapped atoms in order to have only one atom trapped. Another approach for preparing one atom in a tightly focused dipole trap is based on a "collisional blockade" mechanism, which locks the average number of loaded atom to 0.5 [58, 59].

Storage time

The measured lifetime of atoms in the dipole trap is about 25 s limited by background gas collisions. However, for the realization of the moving standing wave (see Sec. 2.4) the both dipole trap beams are sent through acousto-optic modulators (AOMs) to mutually detune their frequency. The phase noise of the dual-frequency generator, which drives both AOMs, results in heating and subsequent loss of trapped atoms, limiting the storage time to about 6 s. For an overview of various heating mechanisms in the DT see Ref. [51].

1.5 Imaging single atoms

Spatial information on the trapped atoms, such as their position and separations, is essential for many experiments with single or few atoms. It was a prerequisite for the individual addressing of the atoms and the realization of a neutral atom quantum register [18, 60]. The first visual evidence of the transport of single atoms with our "optical conveyor belt" (Sec. 2.4) was performed by continued imaging of the atoms while shifting the standing-wave pattern [45]. In this thesis I use the spatial information for sub-micrometer position control of single atoms, see Chapter 2 and Ref. [25], allowing deterministic atom-cavity coupling, see Chapter 4.

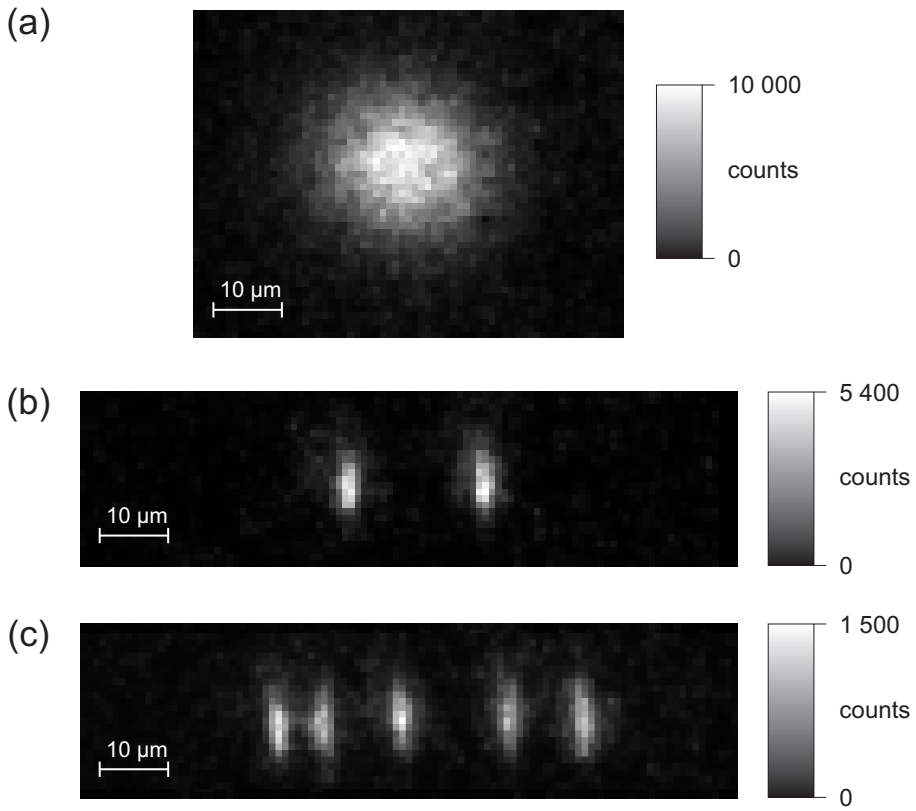

Figure 1.8: (a) CCD image of two atoms in the MOT with an exposure time of 1 s. The rms radius of the MOT inferred from the image is about 5 μm. (b) CCD image of two atoms in the DT illuminated by the optical molasses. (c) Five atoms in the DT.

Intensified CCD camera

Information on the position and/or distribution of the atoms in the trap is obtained from their fluorescence image recorded by a CCD camera (Roper Scientific, PI-MAX:1K). Combined with the image intensifier (Roper Scientific, GEN III HQ) it has a quantum efficiency of approximately 10 % at 852 nm. One detected photon generates on average 350 counts on the CCD chip (1024×1024 pixel large), and one $13\,\mu\text{m} \times 13\,\mu\text{m}$ CCD pixel corresponds to $0.9328(\pm 0.0004)\,\mu$m in the object plane (see Sec. 2.6). The read-out noise is about 80 counts per pixel. For more details on the ICCD camera see Ref. [61].

Illumination of atoms

Due to the low scattering rate in the far-detuned dipole trap, direct imaging of trapped atoms in the DT is not possible. Therefore, we illuminate them with near-resonant three-dimensional optical molasses formed by the MOT cooling lasers acting like a flash of a conventional camera. Besides the illumination, the molasses provides cooling of the trapped atoms counteracting heating through photon scattering, resulting in an atom

temperature of about 70 μK. Note that this cooling also counteracts the heating of atoms due to phase-noise of the frequency generator driving our "optical conveyor belt" for transporting atoms, see Sec. 2.4. Intensity and detuning of the illuminating beams are optimized to exclude losses of atoms, to prevent them from hopping between different potential wells of the DT, and to provide high contrast of the imaged atoms [55]. As a result, we can non-destructively observe single atoms for about half a minute limited only by atom losses due to background gas collisions [45].

Figure 1.8(b) shows an image of two atoms in the DT with an exposure time of 1 s. The horizontal width of the fluorescence spot of 1.5 μm rms is determined by the resolution of the imaging optics. It is larger than the periodicity $\lambda/2 \approx 0.5\,\mu$m of the standing-wave trap and thus does not allow us to resolve atoms trapped in adjacent potential wells. The vertical width of the fluorescence spot, i.e. perpendicular to the DT axis, is essentially defined by the spread of the Gaussian thermal wave packet of the atom in the radial direction of the trap due to its radial oscillation. In Sec. 2.2 I describe how we infer the position of optically resolved atoms along the trap axis with sub-micrometer precision by analyzing their fluorescence image.

1.6 Conclusion

In this Chapter I have presented a set of tools for preparing and controlling single caesium atoms required for our experiments. A high-gradient magneto-optical trap cools atoms from background gas in a vacuum glass cell and confines them to a volume of about 5 μm radius. The exact number of trapped atoms is then inferred from the MOT fluorescence light.

To provide a conservative trap required for any experiments on atomic coherence, including cavity QED measurements, we use a standing-wave dipole trap allowing us to store the atoms for long times without significant photon scattering and mixing of quantum states. Besides, its standing-wave structure provides a tight sub-micrometer confinement of atoms along the trap axis and enables us to transport the atoms, as will be described in Chapter 2. The atoms can be transferred between the two trap with almost unity efficiency. Molasses cooling with the MOT beams allows us to image single atoms in the dipole trap using an intensified CCD camera. This gives us spatial information on the atoms necessary for deterministic atom manipulation.

To overcome the Poissonian statistics of the atom loading and to prepare a desired number of atoms in the DT for a planned experiment, we have implemented a feedback mechanism for the number-triggered loading of the dipole trap. It repeatedly loads the MOT until the desired number of atoms is captured and only then transfers them into the dipole trap. In Sec. 4.5 we use this method for the efficient preparation of one atom in the dipole trap.

Chapter 2

Submicrometer position control of single atoms

2.1 Introduction

Precision position measurement and localization of atoms is of great interest for numerous applications and has been achieved in and on solids using, e.g., scanning tunnelling microscopy [43], atomic force microscopy [62], or electron energy-loss spectroscopy imaging [63]. However, if the application requires long coherence times, as is the case in quantum information processing or for frequency standards, the atoms should be well isolated from their environment. This situation is realized for ions in ion traps, freely moving neutral atoms, or neutral atoms trapped in optical dipole traps. For the case of ions, positions [64, 65] and distances [66] have been optically measured and controlled with a sub-optical wavelength precision. Similar precision has been reached in an all-optical position measurement of freely moving atoms [67]. Dipole traps, operated as optical tweezers, have been used to precisely control the position of individual neutral atoms [23, 68]. To my knowledge, however, a nanometric position and distance measurement has so far not been achieved in this case. Such a control of the relative and absolute position of single trapped neutral atoms, however, is an important prerequisite for cavity quantum electrodynamics experiments, allowing us to deterministically place an atom precisely at the point of the maximum atom-photon coupling inside the cavity.

In this chapter I describe the methods developed for measuring and controlling the position of single neutral atoms stored in a standing-wave optical dipole trap. The main results presented here are published in Ref. [25]. The positions of the atoms are inferred from their fluorescence using high resolution imaging optics in combination with an intensified CCD camera. The absolute position of individual atoms along the DT is measured with a precision of 143 nm, see Sec. 2.2. The relative position of the atoms, i.e. their separation, is determined more accurately by averaging over many measurements, yielding an uncertainty of 21 nm, see Sec. 2.3. Due to this high resolution, we can resolve the discreteness of the distribution of interatomic distances in the standing-wave potential, even though our DT is formed by a Nd:YAG laser with potential wells separated by only

$\lambda/2 = 532$ nm. This resolution allows us to determine the exact number of potential wells between simultaneously trapped atoms. Combining an initial position measurement with a controlled transport of single atoms over macroscopic distances by means of our "optical conveyor belt" technique [23, 24], described in Sec. 2.4, we transport individual atoms to a predetermined position along the DT axis with an accuracy of 300 nm, thereby demonstrating a high degree of control of the absolute position of an atom, see Sec. 2.5.

2.2 Measurement of the position of an atom

In order to obtain fluorescence images of the atoms in the DT, we illuminate them with a near-resonant three-dimensional optical molasses, see Sec. 1.5 and Fig. 2.1(a). An ICCD image of a single atom stored in the DT with an exposure time of 1 s is shown in Fig. 2.1(b). This exposure time is much longer than the timescale of the thermal position fluctuations of the atom inside the trap. Therefore, the vertical width of the fluorescence spot, i.e. perpendicular to the DT axis, is essentially defined by the spread of the Gaussian thermal wave packet of the atom in the radial direction of the trap, which depends on the trap depth and the atom temperature.[1] In the axial direction of the DT, the wave packet has a much smaller $1/\sqrt{e}$-halfwidth of only $\Delta x_{\mathrm{therm}} = 35$–$50$ nm for the typical depth of the DT of 1–2 mK. In addition to these thermal fluctuations, the axial position of the standing wave itself is fluctuating by $\sigma_{\mathrm{fluct}}(1\,\mathrm{s}) = 42(\pm 13)$ nm during the 1 s exposure time due to drifts and acoustic vibrations of the optical setup (see below). The horizontal $1/\sqrt{e}$-halfwidth of the detected fluorescence peak, $w_{\mathrm{ax}} = 1.30(\pm 0.15)\ \mu$m, is much larger and is caused by diffraction within the imaging optics and a slight blurring in the intensification process of the ICCD [51]. Compared to the point spread function of our imaging system, $\Delta x_{\mathrm{therm}}$ and σ_{fluct} have thus a negligible effect on w_{ax}. In the following I define the atomic positions as the center of the Gaussian thermal wave packets of the atoms.

Line spread function

The ICCD image is characterized by its intensity distribution $I(\tilde{x}, \tilde{y})$, where $\tilde{x}$ and $\tilde{y}$ are spatial coordinates on the CCD ship. It is related to the real object $O(x, y)$, i.e. to the distribution of an incoherent light source in the object plane of the camera, by the convolution with the point spread function, $PSF(\tilde{x}, \tilde{y}; x, y)$, of the imaging system as follows (see e.g. [69, 70])

$$I(\tilde{x}, \tilde{y}) = \iint PSF(\tilde{x}, \tilde{y}; x, y)\ O(x, y)\, dx\, dy + N(\tilde{x}, \tilde{y}), \tag{2.1}$$

[1] In the inverse problem the atom temperature can be determine by direct imaging the atom in the trap and measuring its spatial distribution [51].

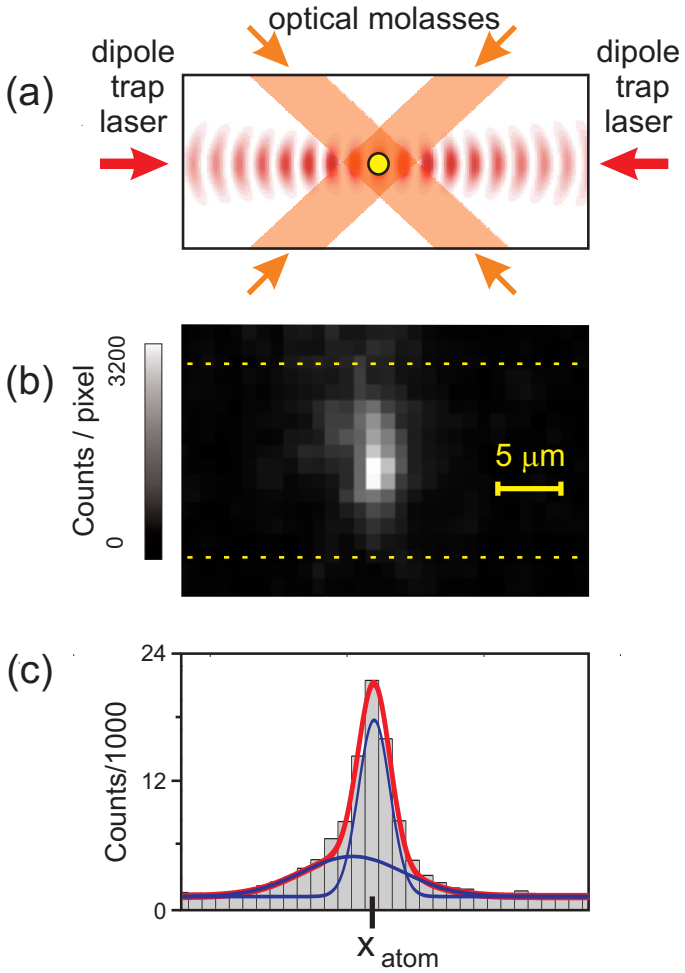

Figure 2.1: Determination of the position of a single trapped atom. (a) An atom stored in the standing-wave dipole trap is illuminated with an optical molasses (schematic drawing). (b) ICCD image of one atom stored in the DT with an exposure time of 1 s. The observed fluorescence spot corresponds to about 200 detected photons. (c) To determine the position of the atom along the DT axis, the pixel counts are binned in the vertical direction. In order to reduce background noise, the summation is only performed over the narrow vertical region shown by dashed lines in (b). The thick solid line corresponds to the line spread function of our imaging optics and reveals the absolute position x_{atom} of the atom. The thin lines are two Gaussians composing the fit function, see text for details.

where $N(\tilde{x}, \tilde{y})$ denotes additive noise. The trapping potentials as seen from the side, and thus our time-averaged fluorescing atoms, have a slit-like form.[2] Since we are interested only in the *horizontal* position $\tilde{x}_{\mathrm{atom}}$ of the fluorescence peak on the ICCD image, we bin

[2] The extent of the atomic cloud along the optical axis is within the depth of focus of about $\pm 6\,\mu$m of the imaging system [51].

$I(\tilde{x}_i, \tilde{y}_j)$ in the vertical direction and get

$$I(\tilde{x}_i) = \sum_j I(\tilde{x}_i, \tilde{y}_j), \tag{2.2}$$

with $\tilde{x}_i$ and $\tilde{y}_j$ denoting the horizontal and vertical position of pixel $\{i, j\}$, respectively. Then, equation (2.1) can be reduced to the one-dimensional one:

$$I(\tilde{x}) = \int LSF(\tilde{x}, x)\ O(x)\, dx + N(\tilde{x}), \tag{2.3}$$

where the imaging process is characterized by the line spread function (LSF) of our imaging optics. For the slit-like object the function $O(x)$ is a δ-function at position x_{atom}. If the imaging system is space invariant, the LSF depends only on the difference $(\tilde{x} - \tilde{x}_{\text{atom}})$. Neglecting noise for the moment, this yields

$$I(\tilde{x}) \propto LSF(\tilde{x} - \tilde{x}_{\text{atom}})\ . \tag{2.4}$$

The object coordinate x_{atom} and the image coordinate $\tilde{x}_{\text{atom}}$ are connected by the relation

$$x_{\text{atom}} = \frac{\tilde{x}_{\text{atom}} - \widetilde{\mathcal{O}}_x}{M}\ , \tag{2.5}$$

where $\widetilde{\mathcal{O}}_x$ is the image coordinate of the origin and M is the magnification of our imaging optics. In general, $\widetilde{\mathcal{O}}_x$ and M have to be calibrated from independent measurements. The precise calibration of M is described in Sec. 2.6. The choice of $\widetilde{\mathcal{O}}_x$ strongly depends on the planned experiment. For instance, in the experiments on addressing individual atoms in a magnetic field gradient [18, 60], the origin can be defined as the point of zero magnetic field. In the present case, however, no physical point in space is singled out as an origin, therefore we arbitrarily set $\widetilde{\mathcal{O}}_x \equiv 0$, i.e. we assign the origin to the left-most CCD pixel.

In principle, the LSF could be determined by modelling the imaging process. However, the modelling requires the precise knowledge of the properties of all optical elements in the optical path as well as of their positions, which is a non-trivial task if we aim at a satisfactory result. Therefore, we determine the form of our LSF experimentally by analyzing about 100 images of single atoms. We have found that the LSF is position-independent, which proves the assumption of the space-invariant imaging system. It is well approximated by a sum of two Gaussians with a ratio of 4.4:1 in heights and 1:3.2 in widths, with a slight horizontal offset with respect to each other, shown in Fig. 2.1(c). In the following, I define $\tilde{x}_{\text{atom}}$ as the position of the maximum of this LSF. In our experiment, it is determined by fitting a simple Gaussian to the fluorescence peak. This procedure has been chosen because it can be carried out in a fast automated way, yielding information about the atomic position during the running experimental sequence. The study on the precise analysis of binned, normally distributed data performed in Ref. [71] shows that the simple Gaussian fit gives the undistorted information on the peak position as long as the peak covers at least three bins, which is the case here. In addition, our simulations taking into account the experimental LSF and the finite bin size show a constant position offset of 42 nm of the fitted center of the Gaussian with respect to the maximum of the LSF, due to the slight asymmetry of our LSF. This offset only leads to a global shift of $\widetilde{\mathcal{O}}_x$ and is thus irrelevant for our analysis.

Statistical error

Since our ICCD is a photon counting device, the basic noise source in determining x_{atom} is the Poissonian fluctuations of the number of photons detected per pixel. The statistical error of the mean position of spatially normally distributed counts on the CCD image is given by

$$\Delta x_{\mathrm{stat}} = \frac{w_{\mathrm{ax}}}{\sqrt{N_{\mathrm{ph}}}} \ , \tag{2.6}$$

where N_{ph} is the number of photons detected per atom. Strictly speaking, equation (2.6) is only valid for a spatial Gaussian distribution of detected photons with an infinitely small bin size. In our experiments with the non-Gaussian LSF and the finite bin size we determine the position and the width of the peak by fitting the binned counts with the Gaussian function. To find the statistical error in this case, we have performed numerical simulation taking into account the experimental LSF and the finite bin size. We have simulated the arrival of N_{ph} photons onto the CCD chip with the LSF distribution, binned them with an arbitrary shift of the bin mask relative to the simulated peak, fitted the binned counts with the Gaussian function, and determined the deviation of the fitted peak center from the real one. The whole procedure was repeated many times to reduce statistical error. The spread of the measured deviations gave us the statistical error of the position detection, which is 1.44 times larger than that given by expression (2.6). Thus, our method allows us to determine the fitted peak center x_{atom} with a statistical error of

$$\Delta x_{\mathrm{stat}} = \frac{1.44\, w_{\mathrm{ax}}}{\sqrt{N_{\mathrm{ph}}}} \ . \tag{2.7}$$

In the experiment the value of N_{ph} depends on the illumination parameters. Here, $N_{\mathrm{ph}} = 200(\pm 30)$ photons per second per atom, so that $\Delta x_{\mathrm{stat}} = 130(\pm 20)$ nm.

Background noise

In addition to the statistical error, two further sources influence the precision of the position detection: the background noise of our ICCD image, described in detail in Ref. [61], and the position fluctuations of the DT. The background in Fig. 2.1 originates in about equal proportions from stray light and from the read-out process of the ICCD, yielding a total offset of 2300(±300) counts per bin for 1 s exposure time. The numerical analysis of the influence of this background on the measured atom position Δx_{atom} reveals that the noise of 300 counts per bin introduces an additional uncertainty of $\Delta x_{\mathrm{backgr}} = 15$ nm to the fitted peak center.

Fluctuations of the trap

The atom position is subject to position fluctuations of the interference pattern of the DT, σ_{fluct}. Since σ_{fluct} cannot be extracted from the ICCD image, we determine it in an independent measurement. For this purpose, we mutually detune the two trap beams by 1.2 MHz and overlap them on a fast photodiode as shown in Fig. 2.2(a). From the phase

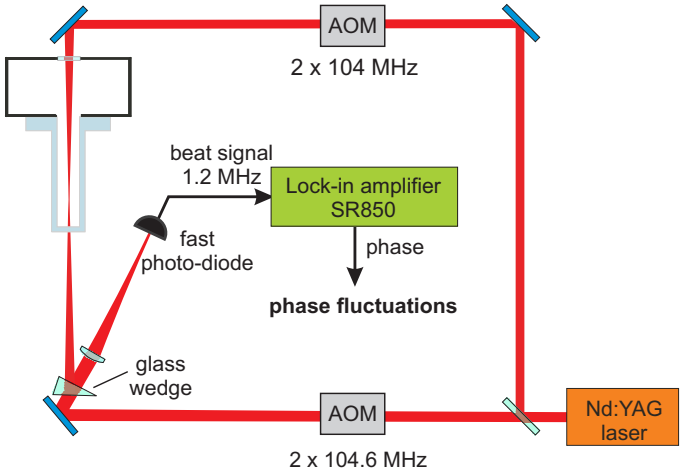

(a) Experimental setup.

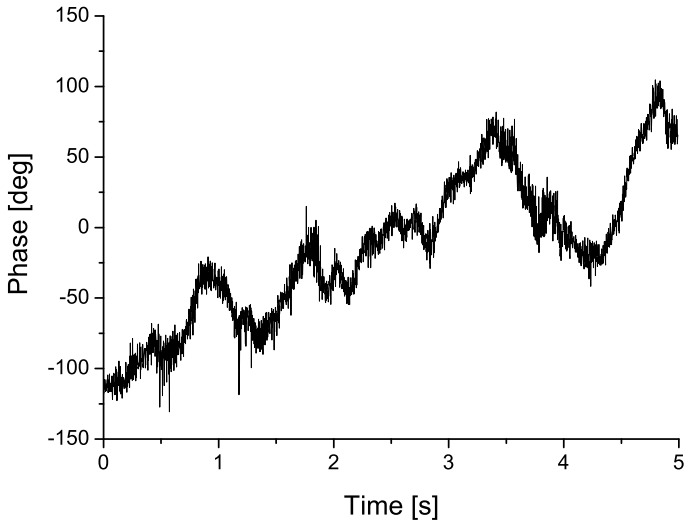

(b) Typical phase variation of the trap.

Figure 2.2: Measurement of the phase variations of the standing-wave dipole trap.

of the resulting beat note we infer the phase variations $\phi(t)$ of the standing wave with a 300 kHz bandwidth, see Fig. 2.2(b). The standard deviation of $\phi(t)$ during the time interval τ, $\sigma_\phi(\tau)$, is directly related to the position fluctuations of the DT during this period by $\sigma_{\text{fluct}}(\tau) = \lambda/2 \cdot \sigma_\phi(\tau)/2\pi$. We have found that $\sigma_{\text{fluct}}(1\,\text{s}) = 42(\pm 13)$ nm. The typical time dependence of $\phi(t)$ in Fig. 2.2(b) shows both fast fluctuations and slow drifts. However, most traces of $\phi(t)$ analyzed do not have significant drifts on the time scale of

one second. Thus, neglecting linear drifts in the following and using the approximation of Gaussian-distributed position fluctuations, which we have checked to be valid to better than 1 % in our case, the position uncertainty immediately after the 1 s exposure time is given by

$$\Delta x^2_{\mathrm{atom}}(1\,\mathrm{s}) = \Delta x^2_{\mathrm{stat}} + \Delta x^2_{\mathrm{backgr}} + \sigma^2_{\mathrm{fluct}}(1\,\mathrm{s}), \tag{2.8}$$

yielding $\Delta x_{\mathrm{atom}}(1\,\mathrm{s}) = 140(\pm 20)$ nm.

Finally, the read-out of the image and the data analysis take an additional 0.5 s during which x_{atom} is further subject to position fluctuations of the DT. This increases the error of the position measurement by $\sqrt{2}\sigma_{\mathrm{fluct}}(0.5\,\mathrm{s}) = 29\,\mathrm{nm}$,[3] which was determined similar to $\sigma_{\mathrm{fluct}}(1\,\mathrm{s})$. Thus, we can determine the absolute position of the trapped atom with a precision of

$$\Delta x_{\mathrm{atom}}(1.5\,\mathrm{s}) = 143(\pm 20)\,\mathrm{nm} \tag{2.9}$$

within 1.5 s (1 s exposure time plus 0.5 s read-out and data analysis). Our analysis shows that this precision cannot be significantly increased by extending the exposure time, because the benefit of the higher photon statistics for longer times is counteracted by the increasing influence of the DT drifts.

Summarizing, the main sources of noise influencing the precision of the position detection are listed below in Table 2.1.

Source of error		**Value**
statistical error	Δx_{stat}	130(±20) nm
CCD background noise	$\Delta x_{\mathrm{backgr}}$	15 nm
DT position fluctuations	$\sigma_{\mathrm{fluct}}(1.5\,\mathrm{s})$	51(±15) nm

Table 2.1: Sources of noise influencing the precision of the position detection.

2.3 Measurement of the separation between two atoms

While for some applications the absolute position of the atoms must be known to the highest possible precision, other experiments, like, e.g., controlled cold collisions between two atoms [72] possibly with subsequent generation of the entangled cluster states of many atoms [73, 74], require a precise knowledge of the separation d between atoms. In the following I show that in our experiment this separation can be determined more precisely than the absolute position of the individual atoms. The reason is that DT position fluctuations equally affect all simultaneously trapped atoms and therefore do not change the separation between them. Thus, this distance can be averaged over many measurements

[3] We have introduced a factor of $\sqrt{2}$, since we are interesting not in the distribution of data points around the mean value during the considered time interval, but in the deviation of the very last point from the very first one.

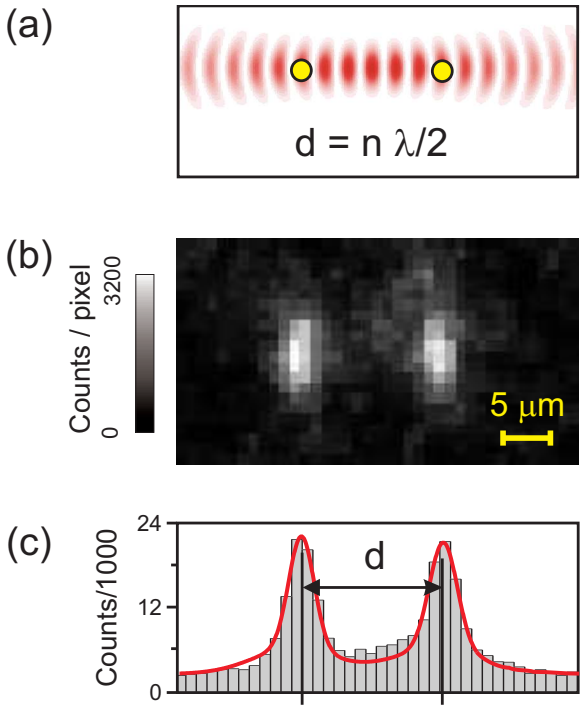

Figure 2.3: Determination of the distance between atoms. (a) Two atoms in the standing-wave dipole trap have a separation of $n\lambda/2$ with n integer. (b) After loading the atoms into the DT, we take camera pictures of them. (c) From each picture we determine the positions of the atoms and their separation d. Averaging over many measurements of d for the same pair of atoms reduces the statistical error and allows us to infer n.

providing much higher precision than for the absolute position. As a result, the obtained precision allows us to resolve the standing-wave structure of our DT and to determine the exact number of potential wells between two optically resolved atoms, a situation that so far seemingly required much longer (e.g., CO_2) trapping laser wavelengths [75].

Distance measurement from a single image

To study the atomic separations in our dipole trap, we first load it with two atoms from the MOT, see Fig. 2.3(a). Normally, the atoms transferred from the MOT are distributed over $\sigma_{\mathrm{MOT}} = 5\,\mu$m along the DT axis, resulting in a spread of the distances of $\sqrt{2}\sigma_{\mathrm{MOT}} \approx 7\,\mu$m. In order to increase the mean separation between the atoms we let them freely expand along the dipole trap by switching off one of the DT laser beams for 0.5 ms eliminating the standing-wave structure for that time interval. Following this expansion the atoms are now distributed over roughly $50\,\mu$m in the standing-wave trap.

Next, we take a camera picture of the atom pair, see Fig. 2.3(b). In these experiments, we detect $N_{\mathrm{ph}} = 270(\pm 30)$ photons per second per atom. From each picture we determine the distance d between the atoms, see Fig. 2.3(c). For this purpose, we fit the fluorescence

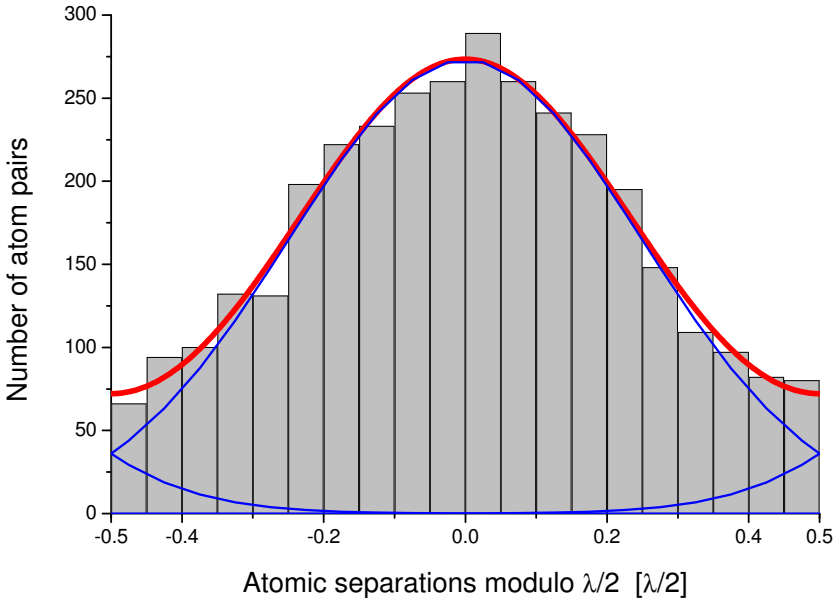

Figure 2.4: Histogram of the measured distances modulo $\lambda/2$ (see equation (2.10). The thick curve is a fit to the data with a sum of three equal Gaussians at the positions 0 and $\pm\lambda/2$. The individual Gaussians are shown as thin curves. Their width of $\Delta d = 132(\pm 5)$ nm determines the precision of the distance measurement.

peaks with the experimentally established line spread function. For the case of partially overlapping fluorescence spots ($d \lesssim 10$ μm), this method yields more precise results for the two positions than fitting simple Gaussians. For $d \lesssim 4$ μm the increasing overlap reduces the precision of the position determination. We have therefore restricted our investigations to the case where the atoms are separated by more than 4 μm. After all, we have accumulated more than 3000 images with two atoms, each providing us with a measured atomic separation d_i.

Being trapped in the standing-wave potential, the atoms are always separated by a distance equal to an integer multiple of $\lambda/2$. Using this fact, we construct a new data set $\{d_i'\}$ by applying the following rule:

$$d_i' = \begin{cases} d_i \bmod_{\lambda/2}, & \text{if } 0 \le d_i \bmod_{\lambda/2} < \lambda/4 \\ d_i \bmod_{\lambda/2} - \lambda/2, & \text{if } \lambda/4 \le d_i \bmod_{\lambda/2} < \lambda/2 \end{cases} \tag{2.10}$$

Here, in order to get the distribution symmetric around zero, I calculate the data points d_i modulo $\lambda/2$ and shift them by $\lambda/2$ if $d_i \bmod_{\lambda/2} > \lambda/4$. The histogram of the new distribution $\{d_i'\}$ with a bin size of $\lambda/40$ is shown in Fig. 2.4. It is centered at 0 and is confined in a range $(-\lambda/4, \lambda/4)$.[4] In the case of a perfect distance measurement, that is with zero uncertainty, the distribution $\{d_i'\}$ should have a δ-function-like form with all d_i'

[4]The precise calibration of the image scale is performed in Sec. 2.6 by centering the histogram of the measured distances at zero.

equal zero. On the other hand, if the precision of the distance measurement is much worse than the $\lambda/2$ periodicity of the trap, the constructed distribution should appear flat.

In order to extract the distance uncertainty from $\{d_i'\}$, we fit the histogram of Fig. 2.4 with a sum of three equal Gaussians (i.e. of the same height and width) centered at positions $-\lambda/2$, 0, and $\lambda/2$, respectively. The individual Gaussian functions are shown in Fig. 2.4 as the thin lines, whereas their sum is shown by the thick line. The central Gaussian distribution corresponds to those measured separations d_i^{meas}, from which the actual separations d_i^{actual} between atoms can be found as the nearest multiple of $\lambda/2$ to d_i^{meas}. This means that the separation d_i^{actual} can be determined correctly for these measurement events. The two other Gaussians centered at $\pm\lambda/2$ denote events for which d_i^{actual} will be determined wrong by $\pm\lambda/2$, respectively. Consequently, the reliability of our distance measurement is found by integrating the normalized central Gaussian function from $-\lambda/4$ to $\lambda/4$ and thus equals 95.6 %. Therefore, only in 4.4 % of cases the determined separation is wrong by one potential well.

The precision of our distance measurement is given by the width of the fitted Gaussians of $\Delta d^{\text{meas}} = 132(\pm 5)$ nm. Since the DT position fluctuations does not affect the distance measurement, the uncertainty of the separation d between two atoms determined from *one* picture should be $\Delta d^{\text{expect}} = \sqrt{2}\,(\Delta x_{\text{stat}}^2 + \Delta x_{\text{backgr}}^2)^{1/2} = 160(\pm 20)$ nm. Here, Δx_{stat} is calculated from equation (2.7) for $N_{\text{ph}} = 270$ photons. The observed discrepancy between the measured and expected values may come from smaller DT fluctuations during taking data as compared to previous experimental days as well as from different illumination parameters resulting in a larger number of detected photons per atom, thus reducing Δx_{stat}.

Resolving the standing-wave structure

The advantage of the distance measurement compared to the position detection is that the atomic separations are not influenced by the fluctuations of the dipole trap. This allows us to reduce the statistical error in the determination of d by averaging the results from N_{pic} images of *the same* atom pair. The reduced statistical error of the mean value $\bar{d}$ then reads

$$\Delta\bar{d} = \frac{\Delta d}{\sqrt{N_{\text{pic}}}}\ . \tag{2.11}$$

For instance, by averaging over only two images the reliability of the distance measurement can be increased up to 99.6 %, which is enough for most of the feasible experiments with single atoms.

In the next experiment we determine the atomic separation by averaging over more than 9 images of the same atoms. In this case, the probability of a wrong determination of n should theoretically be less than 2.0×10^{-10}. The measurement procedure is the same as before, but instead of one picture, we take at least $N_{\text{pic}} = 10$ successive camera pictures of the same atom pair before one of the two atoms leaves the trap. For each pair of atoms we then calculate the mean value $\bar{d}$ and the standard deviation Δd of the measured distances. Since d can now be measured with a precision $\Delta\bar{d} \ll \lambda/2$, its distribution should therefore reveal the standing-wave structure of the DT. Indeed, the $\lambda/2$ period is strikingly apparent

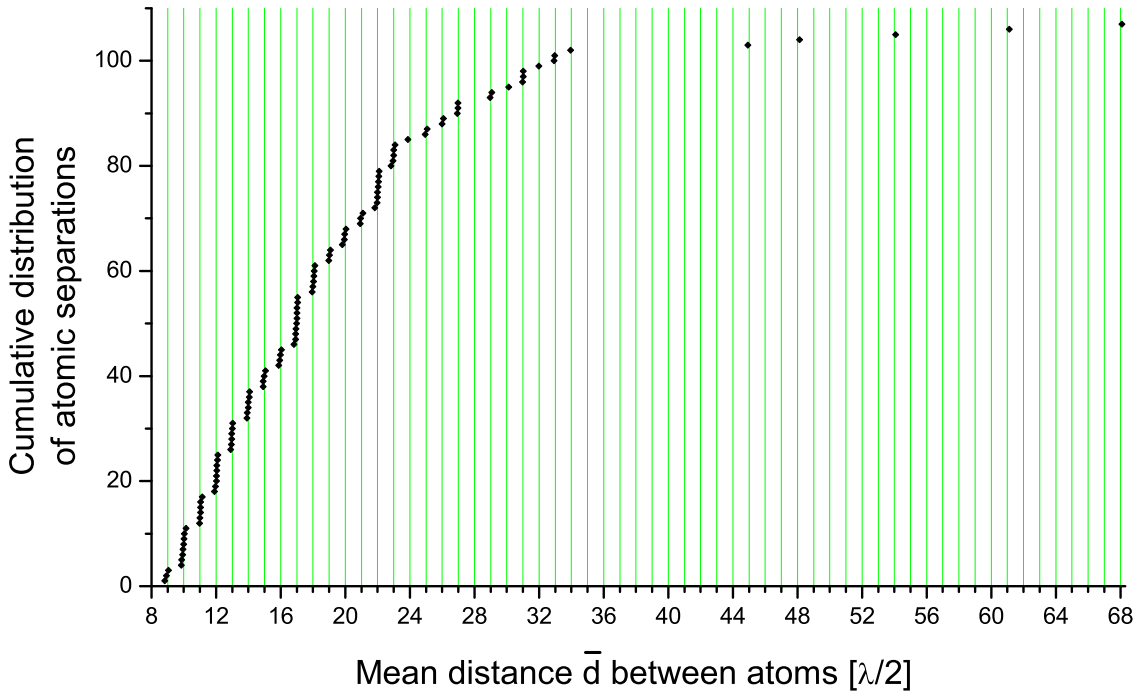

Figure 2.5: Cumulative distribution of separations between atoms in the dipole trap measured with the scheme presented in Fig. 2.3. In order to resolve the periodic structure of the trap, we reduce the statistical error in the measurement of the atomic separation by averaging over more than 9 distance measurements for each atom pair. The discretization of the distances to $n\lambda/2$ is clearly visible in the data. Our resolution is thus sufficient to determine the exact number of potential wells between any two optically resolved atoms.

in Fig. 2.5 which shows the cumulative distribution of averaged distances $\bar{d}$ between atoms measured with about 100 atom pairs.

By analogy with single distance measurements, we can now map the measured $\{\bar{d}_i\}$ to the new data set $\{\bar{d}'_i\}$ using equation (2.10). The corresponding peaked histogram with a bin size of $\lambda/40$ is presented in Fig. 2.6. As compared to the distribution in Fig. 2.4 constructed from single distance measurements, the averaging has significantly improved the resolution of our distance measurement, which can be directly inferred from the finite width of the histogram, yielding $\Delta\bar{d}^{\,\mathrm{meas}} = 21(\pm 1)$ nm. The expected value $\Delta\bar{d}^{\,\mathrm{expect}}$ for the measurement precision can be found using equation (2.11). In the current experiment the mean value of $\{1/\sqrt{N_{\mathrm{pic},i}}\} = 0.198$, where $N_{\mathrm{pic},i}$ denotes the number of pictures taken for the i-th atom pair. Using $\Delta d^{\,\mathrm{meas}} = 132(\pm 5)$ nm, this results in $\Delta\bar{d}^{\,\mathrm{expect}} = 26(\pm 1)$ nm, which agrees reasonably with $\Delta\bar{d}^{\,\mathrm{meas}}$.

Discussion

Due to the thermal position fluctuations of the atoms inside the potential wells, the *instantaneous* distance d_{inst} between the atoms is known with a lower precision of

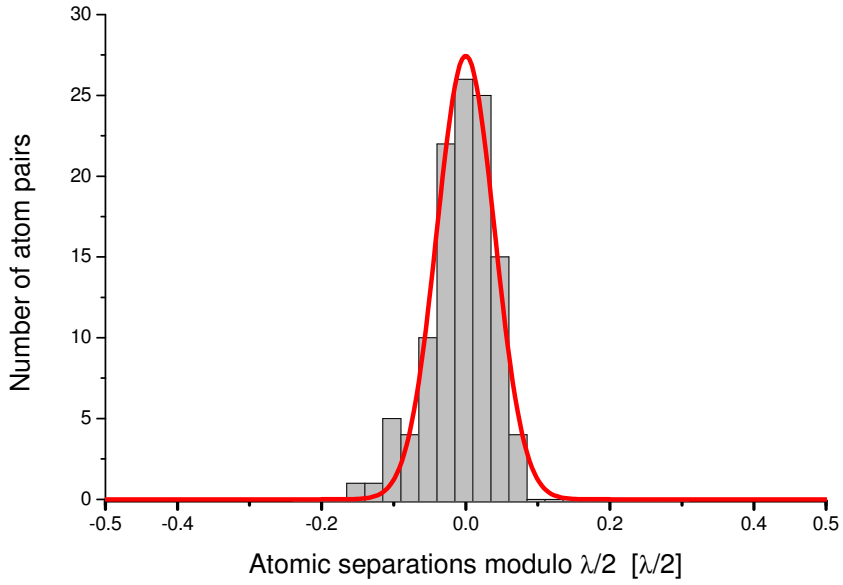

Figure 2.6: Histogram of the atomic separations averaged over more than 9 measurements each and calculated modulo $\lambda/2$. The data analyzed are the one from Fig. 2.5.

$\Delta d_{\mathrm{inst}} = (\Delta\bar{d}^2 + 2\Delta x_{\mathrm{therm}}^2)^{1/2}$. In the axial direction of the DT, the Gaussian thermal wave packet of the atom has a $1/\sqrt{e}$-halfwidth of about $\Delta x_{\mathrm{therm}} = 35$–$50$ nm, depending on the depth of the DT and the atomic temperature. In our case $\Delta\bar{d} < \sqrt{2}\Delta x_{\mathrm{therm}}$, so that we have reached the fundamental limit for determining d_{inst}. This limit is intrinsic to our method because the back-action of the measurement does result in heating of the atoms to a finite temperature of approximately 70 μK due to photon scattering.

Finally, since we can resolve the standing-wave structure of our DT and determine the number n of potential wells between any optically resolved trapped atoms, we know the separation between the centers of their thermal wave packets *exactly*, even despite of finite measured width $\Delta\bar{d}$ of the distribution $\{\bar{d}_i'\}$. Note that it is sufficient to average the measured atomic separation over two measurements to achieve this absolute precision.

2.4 The optical conveyor belt

Many planned experiments, and first of all those on accurate placing a single atom into the mode of a high-finesse cavity, require a microscopic position control of the trapped atom over macroscopic distances. For this purpose we use an optical conveyor belt technique [23, 24], allowing us to move the atom along the trap axis over millimeter distances with a sub-micrometer precision [25]. Since the atoms in our experiments are held at the intensity maxima of the optical light field, created by interfering two counter-propagating laser beams, their transportation can be achieved by moving the corresponding standing-wave interference structure. In our experiment this motion is realized by mutually detuning the

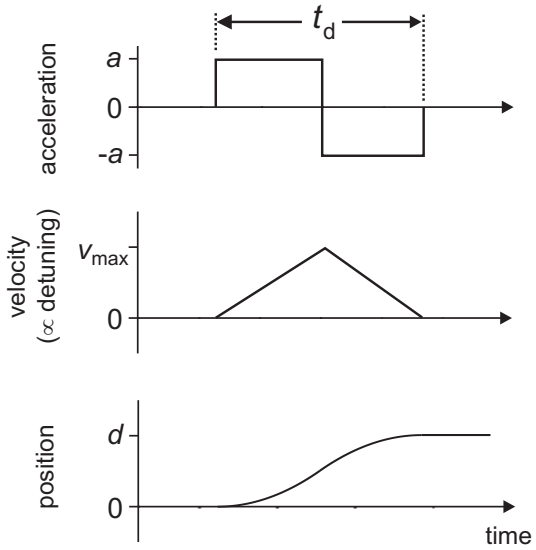

Figure 2.7: Time dependence of the main transportation parameters. In order to transport an atom over the distance d, we expose it to constant acceleration and deceleration a. The velocity is ramped from 0 to $v_{\max} = at_{\mathrm{d}}/2$ and back to 0.

frequencies of the two trapping lasers.

A moving standing wave

Our "optical conveyor belt" consists of a standing-wave dipole trap made of two counter-propagating laser beams. Motion of the interference pattern along the trap axis is achieved by mutually detuning the laser beams. The time-dependent potential of a standing-wave trap made of two Gaussian beams of frequencies ν_1 and ν_2 reads

$$U(x,y,z,t) = -U_0 \frac{w_0^2}{w^2(x)} \exp\left[-\frac{2(y^2+z^2)}{w^2(x)}\right] \cos^2\left(\pi\Delta\nu t - \frac{2\pi}{\lambda}x\right) \tag{2.12}$$

with $\Delta\nu = \nu_1 - \nu_2$ the frequency difference between the two beams. If the two frequencies are equal, $\Delta\nu = 0$, we get a stationary standing-wave dipole trap of equation (1.13).

The mutual detuning $\Delta\nu \neq 0$ causes the standing wave to move along its optical axis at the constant velocity of

$$v = \frac{\lambda\,\Delta\nu}{2}. \tag{2.13}$$

To smoothly transport a trapped atom over a distance d, the interference pattern is first uniformly accelerated along the first half of d and then uniformly decelerated along the second half with acceleration a, see Fig. 2.7. For this purpose, the frequency difference $\Delta\nu$ is linearly swept from 0 to $\Delta\nu_{\max}$ and then back to 0. Thus, during the transport duration t_{d}, the velocity changes from 0 to $v_{\max} = \lambda\Delta\nu_{\max}/2 = at_{\mathrm{d}}/2$ and back to 0.

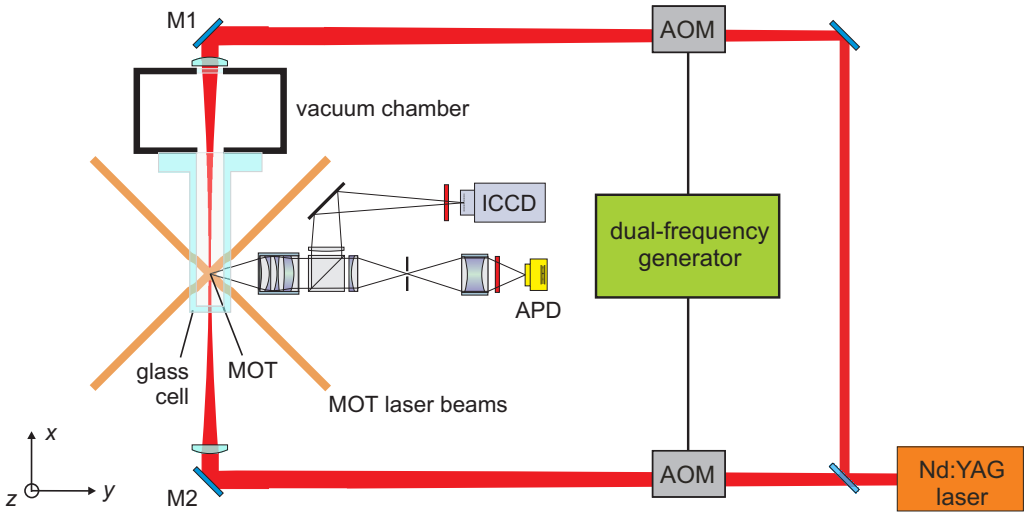

Figure 2.8: Experimental setup of the optical conveyor belt (schematic top view). The standing-wave dipole trap is displaced axially by frequency-shifting its laser beams by means of acousto-optic modulators (AOMs). Both modulators are set up in double-pass configuration (not shown here) and are driven by a phase-synchronous dual-frequency RF generator. By synchronously tilting mirrors M1 and M2, the dipole trap axis is translated radially.

Experimental realization

In the experiment, the frequencies of the two laser beams constituting our dipole trap are controlled by means of acousto-optic modulators (AOMs) installed in each beam as depicted in Fig. 2.8. The AOMs are set up in double-pass configuration to avoid beam walk-off during frequency shifts. The modulators operate at a center frequency of $f_0 \approx 100$ MHz. Since the relative phase of the AOMs is directly translated to the spatial phase of the standing wave, the frequency sweep during the transport should be phase-continuous.

To drive the AOMs, we use a custom built dual-frequency synthesizer with two phase-synchronized RF outputs (APE Berlin, model DFD 100). For each transportation the generator is programmed with a set of the sweep parameters such as the center frequency, f_0, the maximum frequency detuning, $\Delta f_{\max}$, and the sweep duration, $\tau_{\text{sweep}} = t_{\text{d}}/2$, using an RS232 interface. The reprogramming of the synthesizer takes about 0.5 s, and the prepared frequency sweep is generated after externally triggering the DFD.

Transportation parameters

Due to the double-pass configuration of the AOMs, the frequency difference Δf between the two outputs of the DFD is translated to an optical detuning of the trapping beams of $\Delta\nu = 2\,\Delta f$. The acceleration during the ramped transport thus reads

$$a = \pm\frac{2\lambda\ \Delta f_{\max}}{t_{\text{d}}} \tag{2.14}$$

and the standing-wave structure is displaced by the distance

$$d = \frac{a\, t_\mathrm{d}^2}{4} \ . \tag{2.15}$$

The constant acceleration of the standing-wave dipole trap results in a tilted standing-wave potential seen by trapped atoms [24], thus reducing the effective depth of the potential wells. For a typical trap depth of $U_0 = 1$ mK, the maximum acceleration, for which the atoms can be still trapped in the reduced potential, is limited to about $10^5\,\mathrm{m/s^2}$. Therefore, for the position control experiments in Sec. 2.2 we keep the acceleration fixed at $a = \pm 1000\,\mathrm{m/s^2}$ and vary the sweep duration and the maximum frequency detuning depending on the required transportation distance d:

$$\Delta f_\mathrm{max} = \frac{\sqrt{a\, d}}{\lambda} \qquad \text{and} \qquad \tau_\mathrm{sweep} = \sqrt{\frac{d}{a}} \ . \tag{2.16}$$

In the experiments on deterministic coupling of single atoms to the mode of a high-finesse cavity, presented in Chapter 4, the arrival time of each atom into the cavity should be known exactly, regardless of its initial position. Therefore, to make the time synchronization of different parts of these experiments easier, they are carried out with a fixed transport duration of $t_\mathrm{d} = 4$ ms. For the mean transportation distance of 4.6 mm (distance between the MOT and the cavity mode, see Sec. 3.3.1) this results in the acceleration of $a \approx 10^3\,\mathrm{m/s^2}$. The sweep parameters of the frequency synthesizer are then calculated as

$$\Delta f_\mathrm{max} = \frac{2\, d}{t_\mathrm{d}\, \lambda} \qquad \text{and} \qquad \tau_\mathrm{sweep} = \frac{t_\mathrm{d}}{2} \ . \tag{2.17}$$

Radial transport of atoms

For some experiments in Chapter 4, we need to precisely control the position of the dipole trap axis relative to the cavity mode. Technically, it is easier to displace the dipole trap rather than to move the massive cavity holder. The displacement of the standing wave in two radial directions, i.e. in the horizontal direction perpendicular to the trap axis and in the vertical direction, is realized by synchronously tilting the mirrors M1 and M2, see Fig. 2.8, mounted on piezo-electric actuators, around the corresponding axes. For tilt angles below 0.1 mrad, the variation of the interference pattern at the location of the MOT is small and to a good approximation a pure radial translation is realized. Using this method, we can move atoms by a distance of about 40 μm, limited by the dynamic range of the actuators, in both radial directions within typically 50 ms, limited by their bandwidth.

2.5 Active position control

Using our scheme to precisely measure the position of an atom, we can now actively control its absolute position along the DT axis. This is realized by transporting the atom to

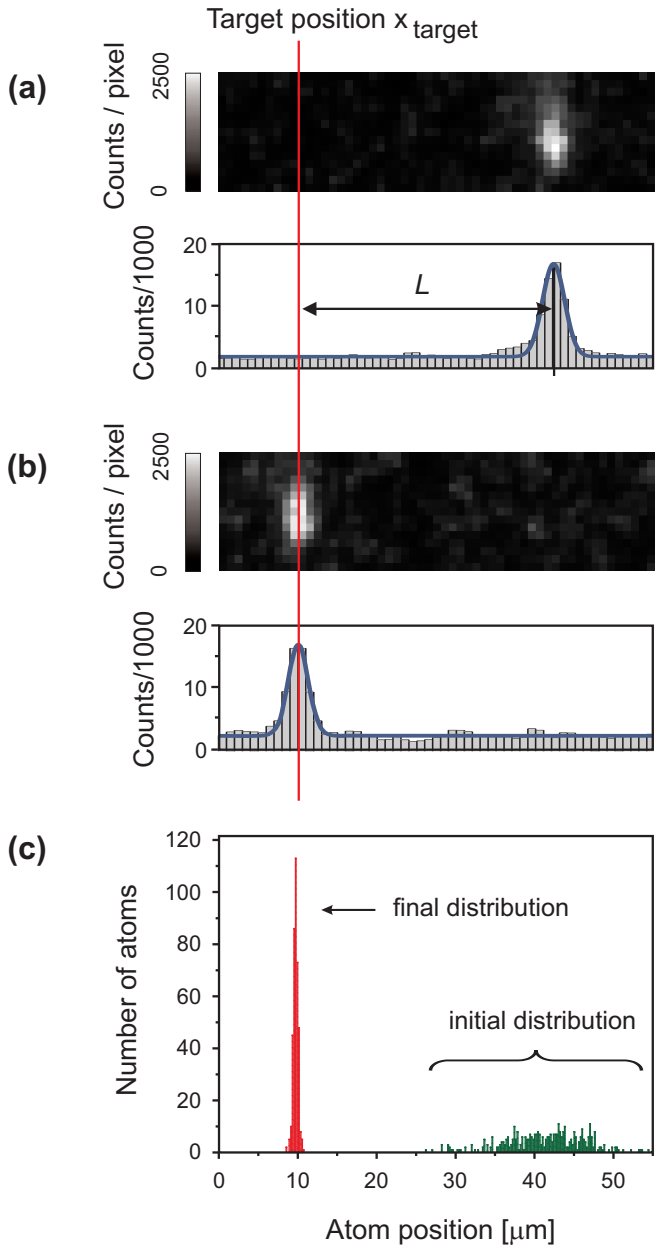

Figure 2.9: Absolute position control of single trapped atoms. To transport an atom to a predetermined target position at $x_{\mathrm{target}} = 9.5\,\mu$m, we first determine its initial position and calculate the distance L to the target position (a). Then we transport the atom and take a second camera picture (b). The histogram in (c) shows the accumulative data of about 400 experiments carried out with one single atom at a time. Transfer of the atoms from the MOT to the DT yields the broad distribution on the right (standard deviation 5.0 μm). The atoms are transported to the target position x_{target} with a precision of 300 nm (narrow distribution on the left).

a predetermined position x_{target} by means of our optical conveyor belt. The following experiment demonstrates our position control technique. Initially, we determine the position of the atom and its distance L from x_{target} from an ICCD image, see Fig. 2.9(a). Then, the DFD is programmed with a set of sweep parameters corresponding to the desired transportation distance L with a fixed acceleration of $a = 1000$ m/s^2. After programming the DFD, it is triggered to start moving the atom. To confirm the successful transport to x_{target}, we take a second image of the atom and measure its final position, see Fig. 2.9(b). The experiment is repeated in a completely automated way many times. Finally we post-select and analyze about 400 experimental shots with a single atom each.[5]

Because the atoms are randomly loaded from the MOT into the DT, the distribution of their initial positions, see Fig. 2.9(c), has a standard deviation of $5.0(\pm 0.3)\,\mu$m, corresponding to the MOT radius. After the transport, the width of the distribution of the final positions is drastically reduced to $\sigma_{\text{control}} = 300(\pm 15)$ nm. This width is limited by the errors in determining the final and initial position of the atom, by the DT position drifts, σ_{drift}, during the typical time of 1.5 s between the two successive exposure intervals, and by the transportation error, σ_{transp}, resulting from a sort of the discretization error (round-off error) of the DFD. From the above DT phase measurement we find $\sigma_{\text{drift}} = 140(\pm 20)$ nm. Assuming that

$$\sigma_{\text{control}} = \sqrt{2\Delta x_{\text{stat}}^2 + \sigma_{\text{drift}}^2 + \sigma_{\text{transp}}^2}\,, \tag{2.18}$$

we calculate $\sigma_{\text{transp}} = 190(\pm 25)$ nm, comparable to the statistical error.

In addition to statistical errors, the accuracy of the position control is subject to systematic errors. The predominant systematic error of this measurement stemmed from the calibration of our length scale. In the present case, a relative calibration error of 0.4 % resulted in a 120 nm shift of the final positions with respect to the target position after a transport over $L \approx 30\,\mu$m. However, this error can be reduced by improving the accuracy of the calibration, see next section.

2.6 Calibration of the image scale

The spatial information on trapped atoms is obtained from CCD images and thus is originally expressed in length units of CCD pixels. All experiments presented in the current chapter are performed on atoms located in the object plane of the imaging optics. Their analysis would be impossible without precise calibration of the image scale, that is the precise correspondence between the measured dimension $\tilde{d}$[pixel] on a CCD image and the real dimension $d[\mu\text{m}]$ at the location of the atoms:

$$d[\mu\text{m}] = \alpha \left[\frac{\mu\text{m}}{\text{pixel}}\right] \tilde{d}[\text{pixel}]. \tag{2.19}$$

The calibration parameter α depends on the magnification of the imaging optics, M, and the linear size of a CCD pixel, a_{pixel}, as $\alpha = a_{\text{pixel}}/M$. The pixel size of our ICCD

[5] These experiments have been performed before the implementation of the controlled loading of the DT with only one atom, described in Sec. 1.4.

camera is $a_{\text{pixel}} = 13\,\mu\text{m}$ and the designed magnification of the system is $M = 14(\pm 1)$, resulting in

$$\alpha_{\text{magnif}} = 0.93(\pm 0.07)\ \mu\text{m/pixel}. \tag{2.20}$$

The obtained precision is not sufficient for our data analysis, since for a length of $100\,\mu\text{m}$ we already get a $7\,\mu\text{m}$ uncertainty. Therefore, we have developed several other calibration methods offering better precision.

Using a constant transport of atoms

This calibration method is based on a transport of a single atom over a known distance $d[\mu\text{m}]$, while measuring its initial and final positions from the CCD image and determining the corresponding transportation distance $\tilde{d}[\text{pixel}]$. After transporting 45 single atoms we have determined a calibration parameter of

$$\alpha_{\text{trans}} = 0.931(\pm 0.004)\ \mu\text{m/pixel}. \tag{2.21}$$

The main sources of error are the same as those of the position control experiment in Sec. 2.5, namely a statistical error of two position measurements and the fluctuations of the dipole trap between two images. Besides, this calibration method also relies on a faultless operation of the dual-frequency synthesizer driving our conveyor belt. Its internal data digitalization can in particular result in a systematical error, which might in general be dependent on the transportation distance. To eliminate this problem, the calibration should be performed for different transportation distances, making this method more complicated.

Using the periodicity of the DT potential

Analyzing the histogram of distances

To perform a precise scale calibration, we analyze the measured atomic separations. Due to the standing-wave structure of our dipole trap, the real atomic separations exactly equal integer multiples of $\lambda/2$. In Sec. 2.3 we have constructed an auxiliary data set $\{d_i'\}$ using equation (2.10) by calculating modulo $\lambda/2$ of atomic separations $\{d_i\}$. The properties of the new set strongly depend on the calibration α, since it was used for calculating the parent data set $\{d_i\}$ in units of $[\mu\text{m}]$ from atomic separations initially measured in pixels.

As can be seen from the histogram in Fig. 2.4, the optimal calibration parameter α_0 results in the distribution $\{d_i'\}$ centered at zero and having the smallest width. Therefore, we calculate a mean and a standard deviation of $\{d_i'\}$ for different α. The corresponding dependencies, obtained from about 3000 atomic separations,[6] are presented in Fig. 2.10. The optimal calibration α_0 is then found at a position of the mean $\overline{\{d_i'\}} = 0$ and of the standard deviation $\sigma(\{d_i'\}) = \min$. The obtained results are listed in a table below.

[6] This data set is the same one as used in Sec. 2.3 for analyzing the periodicity of the dipole trap.

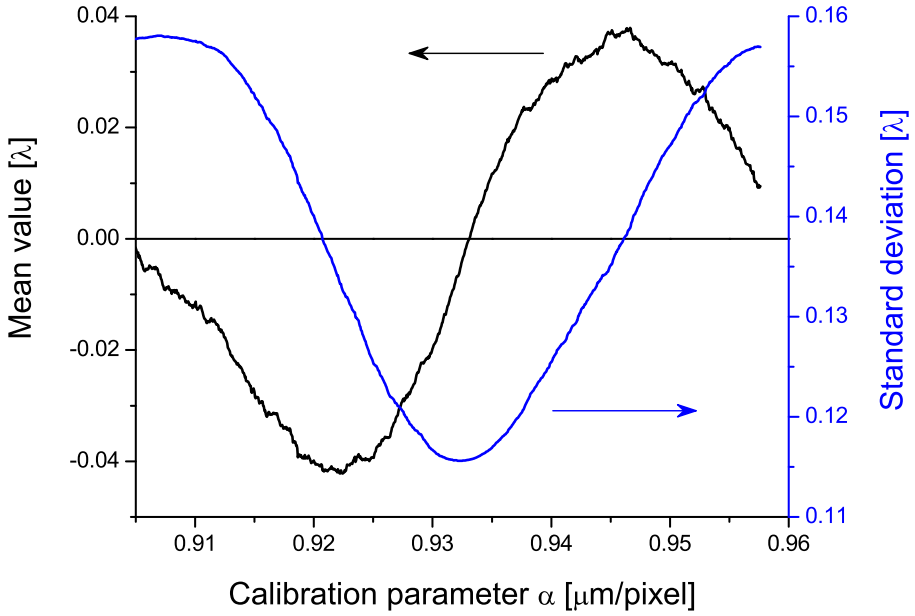

Figure 2.10: Calibration of the image scale using atomic separations calculated modulo $\lambda/2$. Shown are the mean value and the standard deviation of the atomic separations $\{d_i'\}$ modulo $\lambda/2$ (see equation (2.10)) for different calibration parameters α. The optimal α_0 corresponds to zero of the mean value and a minimum of the standard deviation.

Measure	α_0 [μm/pixel]
mean value	0.9331 ± 0.0002
standard deviation	0.9325 ± 0.0002

The statistical error, which is mainly due to the finite size N of the set $\{d_i\}$, is estimated by calculating values of α_0 from 20 randomly selected subsets of $N/2$ distances. If their standard deviation is denoted by $\sigma_{N/2}$, the statistical error for the whole set of distances is then given by $\sigma_N = \sigma_{N/2}/\sqrt{2}$.

We set the final value of α by averaging over two results obtained from different criteria:

$$\alpha_{\text{modulo}} = 0.9328(\pm 0.0002)\ \mu\text{m/pixel}\ . \tag{2.22}$$

Fourier transformation of the atomic separations

An alternative approach to investigate the periodicity in the data set $\{d_i\}$ is based on a Fourier analysis of the measured atomic separations [76]. For this purpose, we consider the periodic distribution function

$$f(x) = \frac{1}{N}\sum_{i=1}^{N}\delta(d_i - x), \tag{2.23}$$

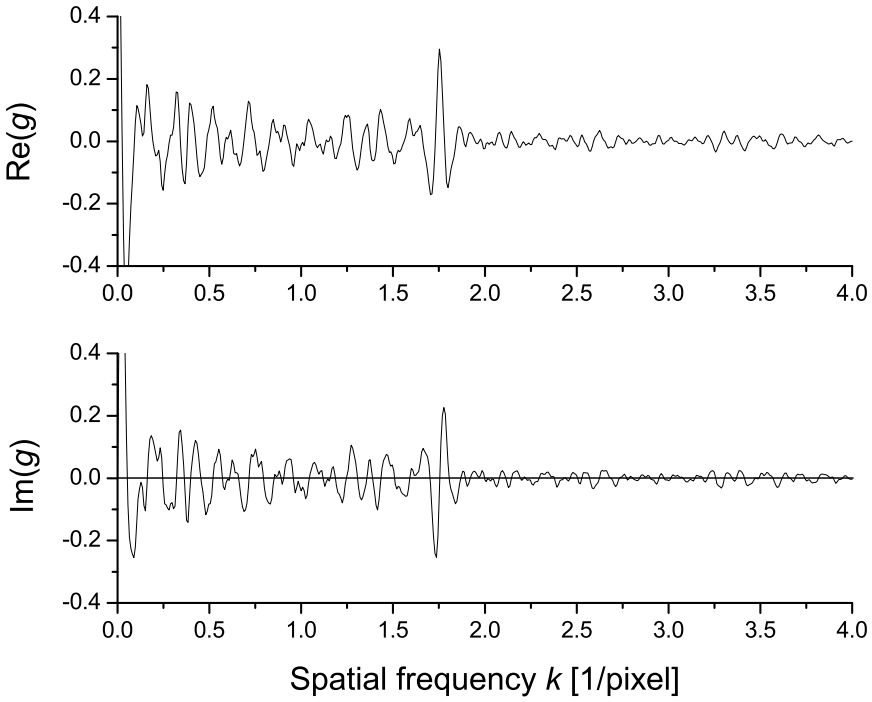

Figure 2.11: Fourier transformation of the distribution of atomic separations.

built by summing over delta functions at the measured atomic separations d_i[pixel]. To find its period, corresponding to the $\lambda/2$ periodicity of the atomic separations, we calculate its Fourier transform

$$g(k) = \frac{1}{\sqrt{2\pi}} \int_{-\infty}^{\infty} f(x)\, e^{\,2\pi i k x} dx = \frac{1}{\sqrt{2\pi}\, N} \sum_{i=1}^{N} e^{\,2\pi i k d_i}. \tag{2.24}$$

The real, Re(g), and imaginary, Im(g), parts of the Fourier transform of $f(x)$ are shown in Fig. 2.11. The analyzed atomic separations are the same as used in the previous calibration method. The spatial frequency k_0, which corresponds to the periodicity of the DT, shows up as a peak in Re(g) and as a zero crossing in Im(g). The calibration parameter α is then found as

$$\alpha = k_0\, \lambda/2. \tag{2.25}$$

The results of this calibration method are listed in a table below.

Measure	α [μm/pixel]
real part	0.9326 ± 0.0002
imaginary part	0.9331 ± 0.0002

The statistical error of α is estimated in the same way as in the previous calibration method using the same subsets of $N/2$ distances. After averaging over the two α's, the

final calibration parameter reads

$$\alpha_{\text{Fourier}} = 0.9329(\pm 0.0002)\ \mu\text{m/pixel}. \tag{2.26}$$

The two calibration methods using the histogram analysis and the Fourier transform are mathematically closely related. Their similarity is indicated by the fact that the calibration error as well as the discrepancy between the two measures used for determining α are the same for both methods.

Summarizing, we have developed several different methods for calibrating the CCD image scale. While providing different precision, they all result in the same calibration parameter α within their individual uncertainties. The method based on transporting single atoms is fast, but it appears to be an order of magnitude less precise than two other procedures utilizing the discreteness of the atomic separations. They both result in the same high precision for determining α of about $0.02,\%$. However, the more involved analysis of atomic separations require a larger data set as compared to the transport method.

Note that for technical reasons the magnification of our imaging system was approximately doubled before performing the set of experiments described in Chapter 4. This yields the new calibration of the CCD image of $\alpha_{\text{Chapter 4}} = 0.4967(\pm 0.0002)\,\mu\text{m/pixel}$ found by performing Fourier analysis of atomic separations and used in the rest of my thesis. This modification by no means changes the main results of the present chapter.

2.7 Conclusion and discussion

In this chapter I have presented a detection scheme for the absolute and relative position of individual atoms stored in our standing-wave dipole trap, yielding nanometric resolution. This scheme allows us to resolve the 532 nm-period standing-wave structure of our dipole trap and to measure the exact number of potential wells separating simultaneously trapped atoms. We have furthermore used our position detection scheme to transport an atom to a predetermined position with a sub-optical wavelength accuracy of 300 nm.

These results represent an important step towards experiments in which the relative or absolute position of single atoms has to be controlled to a high degree. In Chapter 4, this technique is used to transport individual atoms over several millimeter distances and to deterministically couple them to the mode of a high-Q optical resonator.

Furthermore, knowing the exact number of potential wells separating the atoms, we can now control this parameter by placing atoms into specific potential wells of our standing wave using additional optical tweezers [26]. Finally, the demonstrated high degree of control allows us to transport two individual atoms into one potential well in order to induce cold collisions between them [77].

Chapter 3

The high-finesse optical resonator

The heart of any cavity QED experiment is a resonator for confining and storing light. In this chapter, I first describe the high-reflectivity mirrors, which were specially designed and manufactured to meet the requirements for our planned cavity QED experiments with optically trapped cesium atoms. Several techniques for their characterization and analysis as well as the corresponding results are presented. The second part of the chapter is dedicated to assembling, locking, and studying the high-finesse optical cavity, the particular properties of which render it compatible with the current atom-trapping experimental setup. This cavity is used in the experiments on coupling single atoms to a cavity mode as described in Chapter 4.

3.1 An optical resonator for cavity QED experiments

Strong coupling in cavity QED

For exploring coherent atom-photon interaction the coupling between atom and cavity field should be strong compared to all losses (dissipations) in the system, see Fig. 3.1. The coupling rate, g, for a given atomic transition with the dipole moment, d, is proportional to the electric field strength, E, for a single photon, resulting in [78]

$$g = \frac{d\,E}{\hbar} = d\sqrt{\frac{\omega_0}{2\hbar\epsilon_0 V}}\,, \tag{3.1}$$

see also Sec. 4.2.1. The atom-photon coupling can be therefore increased by decreasing the cavity mode volume, V, providing better confinement for the light field.

The main sources of energy dissipation in an atom-cavity system are the atomic dipole decay rate, γ, and the cavity field decay rate, κ. The first occurs due to spontaneous emission of an atom into modes of the electromagnetic field other than the cavity mode. The other source of dissipation is based on leakage and absorption of cavity photons due to non-perfect, lossy mirrors. This cavity loss rate can be kept small by utilizing mirrors with the highest possible reflectivity.

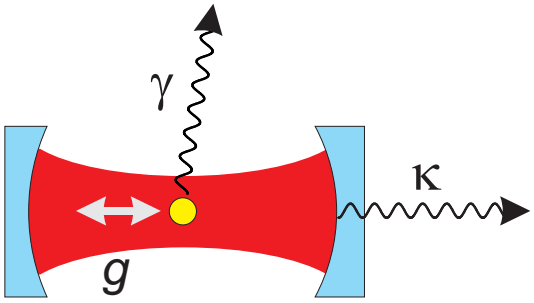

Figure 3.1: Basic elements and rates in a cavity QED system. An atom is coupled to an electromagnetic mode of a cavity, built of i.e. two mirrors. In the strong coupling regime, the atom-photon coupling rate, g, is larger than the atomic dipole decay rate, γ, and the cavity field decay rate, κ.

If the condition $g \gg (\gamma, \kappa)$ is satisfied, we get into the so-called strong coupling regime, which allows us to study coherent energy evolution in the coupled atom-cavity system and to explore cavity QED effects while neglecting all sources of energy dissipation. As a measure of a coupling strength compared to dissipation we can use the single-atom cooperativity parameter, defined as

$$C_1 = \frac{g^2}{2\kappa\gamma}\,. \tag{3.2}$$

In the strong coupling regime, $C_1 \gg 1$.

Mode volume

I consider in the following a symmetric Fabry-Perot resonator built of two opposing concave mirrors, as schematically depicted in Fig. 3.1. The electromagnetic mode inside such a cavity has a Gaussian standing-wave profile described by a spatial function

$$\psi(\vec{r}) = \exp\left[-\frac{x^2+y^2}{w_0^2}\right] \sin\left(\frac{2\pi z}{\lambda}\right), \tag{3.3}$$

where w_0 is the mode waist. Here, the divergence of the Gaussian mode for the short cavity (i.e. if the cavity length is smaller than the Rayleigh range of the Gaussian mode) has been neglected. The mode volume V of the electromagnetic field is obtained by spatially integrating $|\psi(\vec{r})|^2$, yielding for the fundamental TEM_{00} mode

$$V = \frac{\pi w_0^2}{4} L\,, \tag{3.4}$$

where L denotes the cavity length. If the cavity is made of equal concave mirrors with a radius of curvature R, its waist equals [79]

$$w_0 = \sqrt{\frac{\lambda}{\pi}\sqrt{\frac{L}{2}\left(R-\frac{L}{2}\right)}}\,. \tag{3.5}$$

Combining equations (3.4) and (3.5), we get

$$V = \frac{\lambda}{8}\sqrt{L^3(2R - L)}\,. \tag{3.6}$$

For $R \gg L$, which is justified for our short cavities (see Sec. 3.3), equation (3.6) leads to

$$V \propto R^{1/2}\, L^{3/2}. \tag{3.7}$$

Thus, the mode volume can be reduced either by shortening a cavity length or by using mirrors with larger surface curvature $1/R$.

Radius of curvature

Taking into account equations (3.1) and (3.7), the atom-cavity coupling scales as $g \propto R^{-1/4}$. Since κ is inverse proportional to the cavity finesse $\mathcal{F}$, see equation (3.12), the dependence of the cooperativity parameter on $\mathcal{F}$ and the mirror radius of curvature reads $C_1 \propto \mathcal{F}/\sqrt{R}$. Thus, the natural way to increase C_1 is to use mirrors with smaller radius of curvature.

However, technical difficulties in polishing mirror substrates with small radii prevent one to achieve small scattering losses and thus a high mirror reflectivity. For instance, the $\mathcal{F} = 10^5$ finesse of our first high-reflectivity mirrors [80, 81] having a radius of curvature of $R = 1$ cm was limited mainly by their surface quality. Thus, after discussions with mirror manufacturers on possible trade-offs between the small R and the large $\mathcal{F}$, we decided on using mirrors with $R = 5$ cm, expecting to get better surface quality of the glass substrates and finally to achieve a finesse of about one million. In this case, by changing from a cavity with $R = 1$ cm and $\mathcal{F} = 10^5$ to a cavity with $R = 5$ cm and $\mathcal{F} = 10^6$, we expect an increase of the cooperativity parameter by more than a factor of 4.

Cavity length and mirror shape

Another way to increase the coupling g is to reduce the cavity length. However, the planned QED experiments require the laser beams forming the dipole trap to pass between the cavity mirrors and cross the cavity mode. This sets the lower limit on the cavity clearance (the distance between mirror edges) of about 150 μm for a waist of the trapping beams of $w_{0,\,\mathrm{DT}} = 35$–40 μm, see Sec. 1.3. In this case the dipole trap beams are clipped by the mirrors at $2w_{0,\,\mathrm{DT}}$.

Since the mirrors are spherical, there is an indentation from the mirror edges to their center. Thus, the gap between edges, as seen by the dipole trap beams, is less than the real cavity length, L, occupied by the cavity mode. The reduction of the cavity clearance is

$$\Delta L = 2R - \sqrt{4R^2 - D^2} \tag{3.8}$$

with R and D denoting the radius of curvature and the mirror diameter, respectively. For instance, for $R = 5$ cm and $D = 3$ mm, $\Delta L = 45$ μm, thus significantly reducing the spacing between the mirror edges for a desired cavity length of $L = 150\,\mu$m.

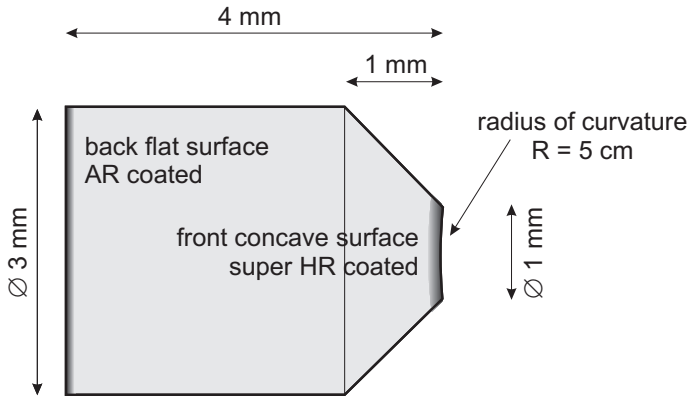

Figure 3.2: High-reflectivity mirror for cavity QED (side view).

The clearance of the cavity can be increased by using smaller mirrors. However, small substrates are difficult to handle. A solution is to turn relatively large substrates down to the desired diameter at the mirror face. For a coned mirror with $D = 1$ mm, $\Delta L = 5$ μm, much smaller than L. Besides, another advantage of a coned substrate shape is the possibility to place an assembled cavity closer to the MOT without blocking the MOT beams, as will be discussed in Sec. 3.3.1.

Note that if a mirror substrate is not symmetrically curved relative to its rotation axis, ΔL will be further increased. For the mirrors investigated in Sec. 3.2, the maximal observed offset of the center of the mirror curvature with respect to the substrate axis is 100 μm, resulting in additional decrease of the cavity clearance of about 1 μm.

Taking into account all presented arguments and drawing on experience of other research groups, we decided on the form of mirror substrates presented in Fig. 3.2. Here, the 3 mm substrates are turned down to a $D = 1$ mm diameter at the tip. The radius of curvature of the concave surface is 5 cm. For a cavity length of, e.g. 150 μm, the size of the TEM_{00} mode at the mirror surface is $w \approx 23$ μm $\ll D$, resulting in negligible diffraction losses due to the finite mirror aperture seen by the light.[1] For the cavity finesse of one million, the expected cooperativity parameter is $C_1^{\mathrm{expect}} = 134 \gg 1$.

3.2 High-reflectivity mirrors

3.2.1 Mirror design

A high-finesse cavity exhibits low photon losses, i.e. the mirror transmission, absorption, and scattering are kept at very low level. Therefore, the two most important issues to be concerned while manufacturing low-loss mirrors are a small roughness of the mirror surface and a special dielectric coating of ultra-high reflectivity.

[1] Diffraction losses reach 1 ppm for a mirror radius of $2.63\,w$, where w is the beam radius at the mirror surface.

Currently, the only company able to fabricate, coat, and cone high-reflectivity optical mirrors suitable for cavity QED experiments is the Research Electro-Optics Inc. (REO) in Boulder, Colorado. The mirror manufacturing process consists of the following steps: First, the substrates of BK7 glass are prepared in a cylindrical form with a diameter of 7.75 mm and a thickness of 4 mm. One side of the substrates is flat and the other side is superpolished to a concave surface with a radius of curvature of 5 cm. Then, the substrates are coated. A standard anti-reflection coating is applied to their flat back surface with measured reflectivity below 0.03 % at 852 nm and below 0.06 % at 836 nm (wavelengths of the probe and the lock laser, respectively, see Sec. 3.3.2). The high-reflecting coating of the curved face should provide a reflectivity of 99.99997 % (corresponding to a finesse of 10^6) and thus is more complex. It consists of 45 alternating dielectric layers of Ta_2O_5 ($n_{\text{high}} = 2.041$) and SiO_2 ($n_{\text{low}} = 1.455$), and each layer has an optical thickness of $\lambda/4$ at 875 nm.[2] Note that the coating is not centered at 852 nm (probe laser) in order to get a higher transmission at 836 nm (lock laser) making the cavity stabilization easier, see Sec. 3.3.2. The total physical thickness of the coating is about 5640 nm. In the last production stage, the coated substrates are turned down to a diameter of 3 mm, and then coned to 1 mm at the mirror tip.

3.2.2 Portable cavity ring-down setup

Collaboration with REO

High-finesse coned concave mirrors, used in cavity QED experiments, constitute the current technological state of the art that can be reached using special super-polishing and super-coating techniques. Since mirrors with $R = 5$ cm and $\mathcal{F} \approx 10^6$ were never produced and investigated before, REO could not guarantee a finesse of one million for the concave mirrors with the specified radius of curvature. For getting the highest achievable finesse, the mirror substrates should be tested after each intermediate manufacturing process. This would help REO to identify sources of errors and imperfections and to find out possible ways for optimization and improvement of different production steps. Besides, the final finesse measurement could be used to select the best mirrors with presumably $\mathcal{F} \gtrsim 10^6$.

A straight-forward way to determine the mirror reflectivity is to measure the fraction of light reflected off the mirror. However, achieving a high precision using this method becomes a non-trivial task due to a reduced signal-to-noise ratio if going to smaller mirror losses. Alternatively, the task of measuring the mirror reflectivity is equivalent to measuring the photon lifetime in a cavity composed of the mirrors under study. By using the cavity ring-down method (CRD, see below), the direct measurement of the cavity decay time for a cavity of a known length allows us to deduce the cavity losses and, therefore, its finesse.

We reached an agreement with REO, where I had to assist them in testing the mirror substrates by measuring the mirror reflectivity after each manufacturing step. This implied the verification of the actual finesse level achieved utilizing our CRD test setup furnished

[2] For a model of multi-layer dielectric coatings see [82, 83].

in REO's metrology lab. The CRD measurements at the specified wavelength had to be performed on all coated mirrors prior to the coning process as well as on the final reshaped mirrors. Moreover, upon delivery of the mirrors and the CRD setup from REO back to Bonn, I had to retest the mirrors and verify that the performance had not changed due to transport-induced damage. On its part, REO was responsible to fully characterize and analyze the mirror substrates prior to coating as well as to use the results of my finesse measurements for optimizing the coating, coning, and cleaning processes in order to get the best possible finesse. Besides, the manufacturer warranted that his packaging would protect the substrates and coatings such that the finesse would not be measurably reduced as a result of the shipment to Germany.

Cavity ring-down

The cavity finesse is defined as the ratio of the free spectral range (FSR) to the cavity full linewidth at half maximum (FWHM),

$$\mathcal{F} = \frac{\omega_{\mathrm{FSR}}}{\omega_{\mathrm{FWHM}}} \,. \tag{3.9}$$

The photon lifetime is connected to the cavity linewidth as

$$\tau = \frac{1}{\omega_{\mathrm{FWHM}}} \,. \tag{3.10}$$

Combining (3.9) and (3.10) and using the definition of ω_{FSR}, we get the basic formula of the CRD measurement:

$$\mathcal{F} = \frac{c\pi}{L}\tau \tag{3.11}$$

with the cavity length L. Since $\kappa = \omega_{\mathrm{FWHM}}/2$, the cavity field decay rate can then be found as

$$\kappa = \frac{1}{2\tau} \qquad \text{or} \qquad \kappa = \frac{c\pi}{2L\mathcal{F}} \,. \tag{3.12}$$

The photon lifetime can be directly inferred from the energy decay of the intracavity light field for a cavity initially filled with resonant light. The exponential decay is measured by observing the light lacking through the cavity mirror and is known as cavity ring-down. The first experiment on measuring decay time to determine cavity losses is presented in Ref. [84]. Measurement of ultra-low losses on mirrors, similar to those used in our experiment, was first performed in the group of Prof. Kimble [85].

A typical experimental procedure of the CRD measurement is the following: By scanning the cavity length, the cavity resonance frequency is tuned towards the laser frequency, until the cavity transmission starts to increase. If the transmitted intensity reaches a preset threshold level, an auxiliary electronics triggers an acousto-optic switch, which turns off the incident laser. The subsequent decay of the cavity output is detected by a fast photodetector and recorded on a digital storage oscilloscope.

Portable cavity ring-down setup

The portable and self-contained cavity ring-down setup enabling us to measure the transmission of both coned and unconed HR coated substrates at REO is based on that developed in our group by W. Rosenfeld [81] for testing the first REO mirrors ($R = 10$ cm, $\mathcal{F} \leq 10^5$), but extended to contain a diode laser and an AOM for fast switching a probe laser. In addition, the modified setup is compatible with testing large unconed mirror substrates and is supplemented with required electronics and power supplies.

A photo of the breadboard (size of 30 cm $\times$ 60 cm), containing the optical setup, as well as the corresponding schematic drawing is presented in Fig. 3.3. The key element of the setup is a mirror holder, developed and described in detail in Ref. [81]. It allows us to scan the cavity length without gluing or clamping the constituent mirrors. In the holder, the mirrors are placed face-to-face in a V-groove providing good coaxial alignment. In order to scan their distance, the two parts of the holder, each carrying one mirror, are connected by a piezo-electric transducer. By applying a voltage to it, the two holder halves are pushed apart, thus changing the cavity length. Besides small coned mirrors, the developed holder is also suitable for testing large mirror substrates of 7.5 mm in diameter before turning them down to 3 mm. This was necessary for comparing the mirror reflectivity before and after the coning process.

As a laser source for probing the cavity we use a home-made temperature-stabilized diode laser in Littrow configuration emitting at 852 nm. The short term frequency stability (at 1 ms) is expected to be 100 kHz. An optical isolator (OI) prevents optical feed-back to the laser diode and, thus, insures its stable operation. An acousto-optic modulator (AOM), operated in first order, is used for fast switching the incident laser off and on. By means of both a half-wave ($\lambda/2$) and a quarter-wave ($\lambda/4$) plate we can choose between different polarization modes of the (in general) birefringent cavity, see Sec. 3.2.4. The aperture (A), placed after the cavity holder, blocks stray light not coupled to the cavity mode. Next, the cavity output light is split on a beam splitter (BS) and send to two optical detectors: a CCD camera is used to monitor and to distinguish between different transversal modes of the cavity and, finally, an avalanche photodiode (APD) measures the cavity output light.

3.2.3 Reflectivity measurement

To determine the mirror quality, we perform a CRD measurement pairwise on all produced mirrors using our CRD setup. For this purpose, two mirrors are put into the mirror holder with a separation of 10 mm (estimated uncertainty is 5 %). The mode coupling of the incoming laser beam is optimized for the cavity TEM_{00} mode. For better signal-to-noise ratio, the cavity decay signal is averaged over about 20 single traces. A typical measurement result is shown in Fig. 3.4. Here, the measured decay time of 12.4 μs corresponds to a finesse of $\mathcal{F} = 1.17 \times 10^6$ and thus to cavity losses of $(1 - R) = \pi/\mathcal{F} = 2.7$ ppm. The estimated error is about 5 % resulting from the uncertainty of the cavity length. The switching time of the incident laser as well as the rise- and fall times of the APD have

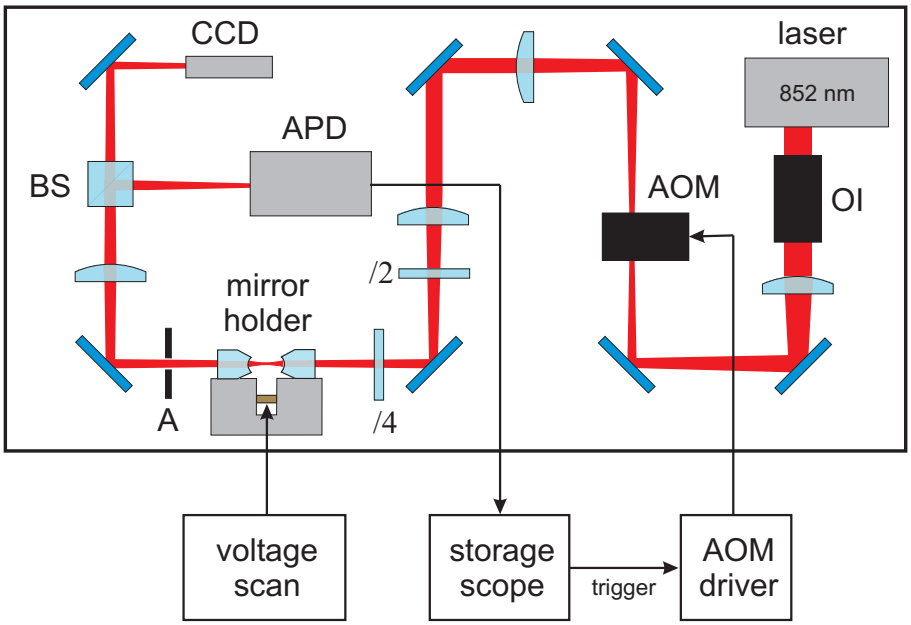

(a) Scheme of the setup.

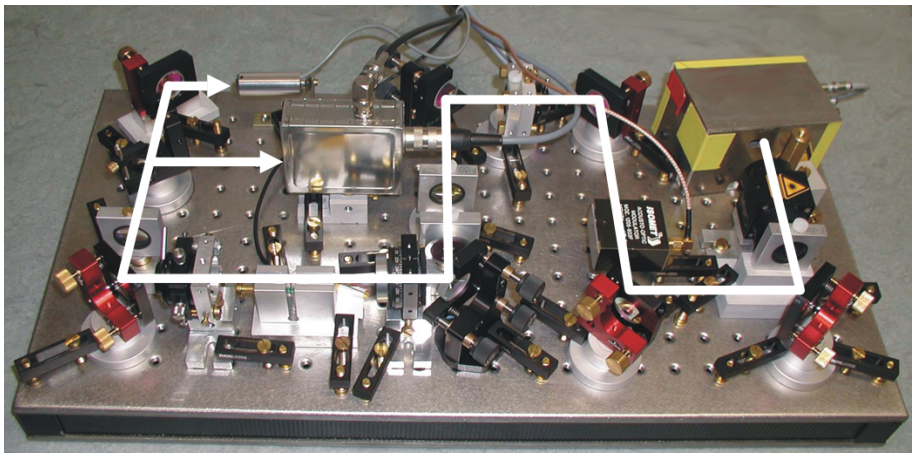

(b) Photo of the setup.

Figure 3.3: Portable cavity ring-down setup. Laser: diode laser at 852 nm, OI: optical isolator, AOM: acousto-optic modulator, $\lambda/2$ and $\lambda/4$: half- and quarter-wave plate, respectively, A: aperture, BS: beam-splitter, APD: avalanche photodiode, CCD: CCD camera. For better guidance, the arrangement of optical elements in (a) and (b) is the same. The white line in (b) follows the laser beam path. The size of the optical breadboard is 30×60 cm^2.

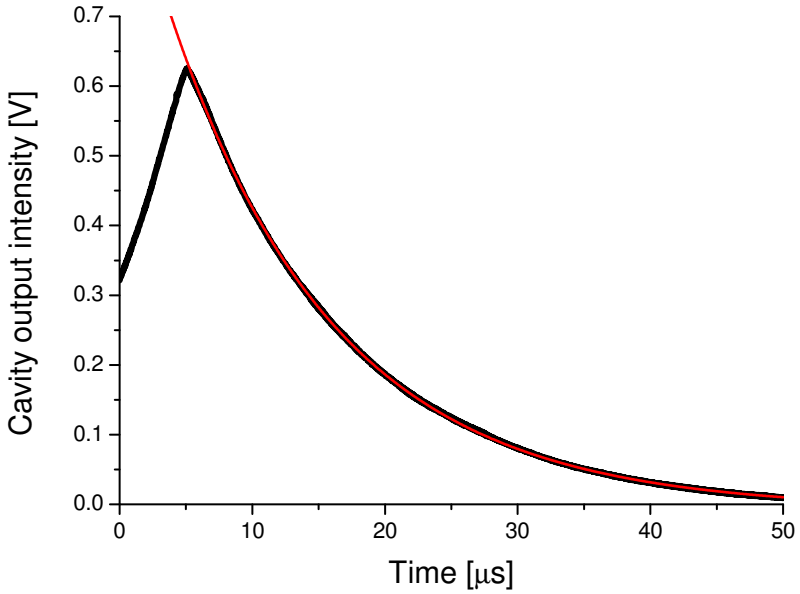

Figure 3.4: Cavity ring-down signal. At time 0 μs the cavity transmission exceeds a trigger threshold and after a delay of about a 5 μs the incident laser is turned off. After that the intracavity light field starts to leak out. The thick curve is an average over about 20 single traces detected by the APD. The thin line is an exponential fit to the data (starting from 5 μs), yielding a decay time of $\tau = 12.4$ μs and, thus, a finesse of $\mathcal{F} = 1.17 \times 10^6$ for a 1 cm-long cavity.

been measured independently and are found to be in the sub-microsecond range, thus not effecting the measured photon lifetime.

The measured cavity decay time alone does not provide information about individual mirrors, but only about the cavity as a whole. Moreover, the measured losses characterize not the entire mirror surface, but only the small spot probed by the cavity mode. In case of inhomogeneous cavity losses (due to, e.g., varying roughness of the surface or local damages of the coating) the measured finesse may strongly vary from point to point. Thus, the finesse of a finally assembled cavity may be in general different from the one measured before.

In order to eliminate these difficulties, we have tested the mirrors after different coating, coning, or cleaning runs in the following way. For each mirror pair we performed several CRD measurements with different relative orientations of the mirrors in order to investigate the spatial inhomogeneity of the cavity losses. Each mirror was investigated several times in different pairs enabling us to determine its individual properties.

As a result of the successful cooperation with REO, which included CRD measurements on all mirrors after each intermediate step in their manufacturing, we got a set of about 10 high-reflectivity mirrors, any two of each can constitute a cavity with a finesse of about 10^6. Further investigation of the mirror properties was continued in our laboratory after the selected mirrors had been delivered to Bonn.

3.2.4 Mirror birefringence

Origin of the birefringence

In general, all optical elements exhibit some degree of birefringence, even if their materials do not show inherent birefringent properties. This effect may come from slight deviation of the optical system from a perfect circularly symmetric one, for instance, because of its geometrical form or stress tension in a bulk material.

The high-reflecting coating might also possess some birefringence depending on the coating process, e.g., on the orientation of a mirror substrate in a coating chamber which might result in a slight asymmetry of the coating. Usually, the birefringent phase shift in this case is negligibly small and cannot be directly observed or measured. But in a high-finesse cavity the light field probes the coating many times resulting in a dramatic enhancement of any small phase shift, making the cavity birefringence significant. If a mirror is glued onto a holder, the induced mechanical stress in its substrate transmits to the coated surface resulting in an additional stress-induced birefringence [82], which can be much larger than the inherent birefringence of the coating. This effect, essential for assembled cavities, will be investigated in Sec. 3.3.4.

The cavity birefringence can, in principle, also be caused by the mirror substrates. However, the resonant intra-cavity light field penetrates only through a few top-most coating layers and thus cannot effectively probe the substrate material. The light resonantly transmitted by the cavity passes through both glass substrates only once and thus does not accumulate enough phase shift to be detected.

Mode splitting

The relative phase shift δ between two orthogonal polarization modes (λ_a, λ_b), which is acquired on each round trip in the cavity, defines a frequency splitting between these modes, $\nu_{\mathrm{split}} = \nu_b - \nu_a$ [86]. Thus, the birefringence appears as a splitting of the cavity transmission line. Since the round-trip phase shift for a mode λ_i is given by

$$\delta_i = 2\pi \frac{2L}{\lambda_i} \ , \tag{3.13}$$

the mode splitting is proportional to δ and reads

$$\nu_{\mathrm{split}} = \frac{\delta}{2\pi} \frac{c}{2L} \ . \tag{3.14}$$

Here, L denotes the cavity length.

The relevance of this mode splitting can be determined by comparing it to the cavity linewidth. Since $\nu_{\mathrm{FWHM}} = \nu_{\mathrm{FSR}}/\mathcal{F} = c/(2L\mathcal{F})$, the ratio of the mode splitting to the cavity linewidth reads

$$\frac{\nu_{\mathrm{split}}}{\nu_{\mathrm{FWHM}}} = \frac{\delta}{2\pi} \mathcal{F} \ . \tag{3.15}$$

It becomes clear, that for a high finesse of $\mathcal{F} = 10^6$ even a tiny phase shift of $\delta = 10^{-5}$ can be readily observed.

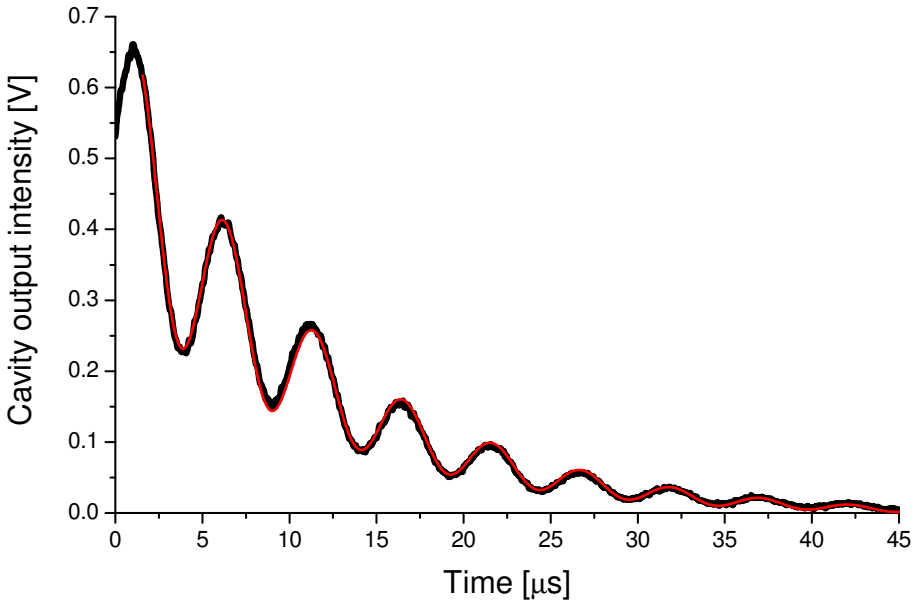

Figure 3.5: Birefringence of high-reflectivity mirrors measured using the CRD setup. The two polarization modes interfere while leaking out of the cavity. The oscillation frequency is equal to the mode splitting. The thin line is a fit, corresponding to equation (3.16), with fit parameters listed in Table 3.1. The graph represents a single trace result.

Measuring the birefringence

The most general way to measure the cavity birefringence is to directly measure the peak splitting ν_{split} by scanning the length of the cavity and recording its double-peak transmission. This method is simple if ν_{split} is larger than the cavity linewidth, ν_{FWHM}, and the laser linewidth, $\Delta\nu_{\text{laser}}$. But, if the splitting is small and the peaks are not well resolved, the accuracy of this measurement might not be satisfactory. Several different ways to measure the small birefringence of high-finesse cavities have been extensively studied in the group of J. Kimble, see e.g. [86]. A general technique is based on scanning the cavity length over the entire cavity resonance profile, injecting light with a well-defined polarization, and detecting the polarization of the transmitted light on a rotatable linear polarizer.

We use an alternative method to measure the birefringence by employing our current CRD setup. Here, if both polarization modes of the cavity are filled with light, they start to leak out of the cavity simultaneously after switching off an incident laser source. If then these, initially orthogonal, polarization modes with different optical frequencies are mixed on some optical elements (e.g., on a mirror, a beam splitter, or a detector active surface), they start to interfere. The resulting beat signal can be detected on top of the overall CRD decay. Moreover, if both modes have the same decay rate, we get the exponential decay modulated at their beat frequency with a constant contrast. A typical signal of such interference is shown in Fig. 3.5.

The fit function to the oscillating decay has the following form:

$$T(t) = A \exp(-t/\tau)\left(1 + C \sin(2\pi\nu t + \phi)\right), \tag{3.16}$$

where C is the contrast of the oscillations, ν and ϕ are the frequency and the phase of the oscillations, respectively. The resulting fit parameters are listed in Table 3.1. The measured oscillation frequency gives the frequency difference between two polarization modes of the cavity.

amplitude	A	0.535 ± 0.001	V
decay time	τ	11.02 ± 0.01	μs
contrast	C	37.5 ± 0.1	%
oscillation frequency	ν	195.1 ± 0.1	kHz
phase	ϕ	70 ± 3	mrad

Table 3.1: Fit results for the oscillating cavity ring-down signal of Fig. 3.5, according to equation (3.16).

Analysis and experimental observations

If two mirrors composing a cavity have almost the same birefringent phase shift, the overall phase shift can vanish for a specific relative orientation of the mirrors, thus reducing the oscillation frequency to zero. On the other hand, if the mirrors show a very different degree of birefringence, the overall phase shift cannot vanish and oscillations are present for any mirror orientation. This effect of an orientation-dependent beat frequency was observed for different pairs of mirrors by rotating one of them with respect to the other one.

The contrast of the oscillations depends both on the relative population of the modes and on the degree of mixing of both polarizations after the cavity. The oscillation can vanish, if the input laser polarization exactly matches one of the cavity polarization modes. The input polarization can be set by rotating a $\lambda/2$-plate placed before the cavity holder.

We have observed that the contrast of the oscillations for each measurement stays constant during the decay, as in Fig. 3.5. This means, that the cavity decay rate is the same for both polarization modes and, consequently, the mirrors do not show noticeable polarization-dependent losses, such as absorption, scattering, or transmission.

The measured birefringence varies strongly within a charge of manufactured high-reflectivity mirrors. The maximal observed mode splitting was about 200 kHz, corresponding to a phase shift of $\delta = 0.8 \times 10^{-4}$ rad. At the same time some pairs showed no detectable splitting. Thus, the best candidates to constitute a high-finesse cavity for the planned experiments are mirrors, which have the largest reflectivity (the longest photon lifetime), while possessing negligible birefringence.

Limits of the method

If the birefringence is large, i.e. if the mode splitting is larger than both the cavity and laser linewidth, the laser may be switched off after triggering on the transmission of the first

cavity mode before the second mode becomes considerably populated. Of course, in this case, no interference is possible and the CRD method fails to measure the birefringence.

The smallest measurable birefringence corresponds to the slowest beat signal between the polarization modes which can be detected with the current method. We have found, that the slowest oscillations, which still can be identified on top of the cavity decay signal, have a period of $T_{\mathrm{osc}} \approx 3.6\,\tau$. Since $\nu_{\mathrm{split}} = 1/T_{\mathrm{osc}}$ and $\nu_{\mathrm{FWHM}} = 1/(2\pi\tau)$, the lowest limit on measuring a mode splitting is thus $\nu_{\mathrm{split}} \approx 1.8\,\nu_{\mathrm{FWHM}}$.

If the mode splitting is even smaller, the induced oscillations cannot be observed on top of the relative fast cavity decay. Although oscillations are not detectible in this case, they still can lead to a small deviation of the decay curve from the ideal exponential one. This then unavoidably results in a decay time, obtained from an exponential fit, significantly smaller (up to 20 %) than the real cavity decay time τ.

The conventional limit for the spectral resolution of two close lines from a spectrum is $\nu_{\mathrm{split}} \approx \nu_{\mathrm{FWHM}}$, thus being lower than that of the presented method based on CRD effect. However, the main advantages of our approach compared to the direct mode splitting measurement are that it does not require a cavity scan to be linear, does not need its frequency calibration, and does not require a laser linewidth to be smaller than that of the cavity.

Birefringence in cavity QED experiments

In case of strong birefringence ($\nu_{\mathrm{split}} > \nu_{\mathrm{FWHM}}$) only linear polarized light can be injected into the cavity. Thus, the birefringence makes it difficult for the cavity field to drive only σ^+ or σ^- transitions in an atom coupled to it. On the other hand, if the mode splitting is comparable to the cavity linewidth, an atom can be simultaneously coupled to both cavity modes, which then can be treated as two different cavities. This significantly complicates the treatment of the atom-cavity system and should be avoided.

The investigation of the birefringence in our set of high-finesse mirrors allowed us to select several mirrors showing the best performance (that is the smallest birefringence if tested together with other mirrors), and thus being the most applicable for cavity construction. Later on, the birefringence of the assembled cavity after gluing and backing the mirrors is studied by scanning through the cavity resonance and directly measuring mode splitting, as will be presented and discussed in Sec. 3.3.4.

3.2.5 Cavity ringing

An alternative method to measure cavity finesse in based on the so-called “cavity ringing” phenomenon, see Ref. [87] and references therein. The transmission of a scanning Fabry-Perot interferometer is given by the well-known Airy function, and for a finesse of $\mathcal{F} \gtrsim 10$ the transmission peak approximately has a Lorentzian profile. However, if the cavity is swept over the laser frequency faster than the cavity decay time, the decaying cavity output field shows an amplitude modulation with increasing frequency, known as cavity

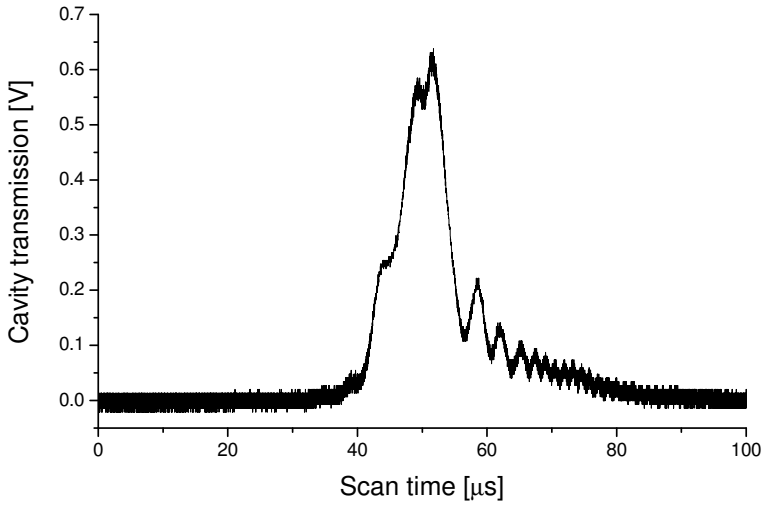

Figure 3.6: Cavity ringing. If the cavity scan over the laser frequency is faster than the cavity decay time, the recorded transmission signal strongly deviates from that given by the Airy function and shows speeding up oscillations on the tail of the transmission peak.

ringing, see Fig. 3.6. The physical insight into this behavior can be obtained by considering the interference between the probe laser and the intracavity field, the frequency difference of which continuously increases, since the probe laser frequency is constant, while the frequency of the intracavity field is continuously shifted due to the cavity scan.

From a classical point of view, the cavity in this problem may be seen as a damped harmonic oscillator with a time-dependent resonance frequency driven by an external periodic force (i.e. by a laser field). The differential equation describing the oscillator's dynamics is solved in Appendix B. Figure 3.7 shows the time dependence of the cavity output intensity for realistic scan parameters. This dependence reproduces well the experimentally measured cavity ringing, shown in Fig. 3.6.

A more complicated decay signal can be observed if both the cavity ringing and the beat of the polarization modes (see Sec. 3.2.4) come into play, as can be seen in Fig. 3.8. From this time dependence one can in principle simultaneously get information about both these effects. However, the analytical analysis of the curve form becomes even more complex.

Cavity ringing and finesse measurement

Since the form of the ringing strongly depends on the relation between the sweep time and the cavity decay time, by analyzing the cavity ringing one can determine the cavity finesse [87]. The advantage of such a measurement is that it does not require switching an incident laser field on and off. However, a linear and continuous cavity scan is essential. If it is not the case, the analytical signal form of equation (B.7) is not valid anymore. Unfortunately, our bulky cavity holder with clamped PZT, initially designed for CRD measurements, does not support a linear cavity scan. As seen in Fig. 3.6, there are several

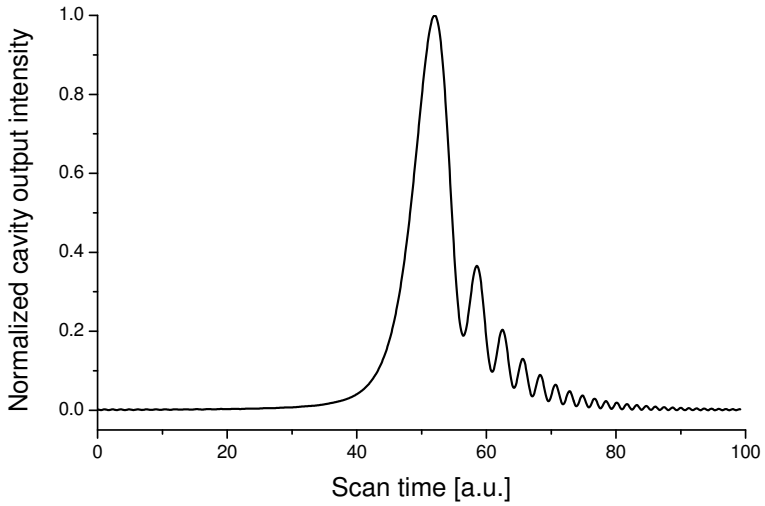

Figure 3.7: Theoretical cavity ringing signal as given by equation (B.7) for realistic experimental parameters (see Appendix B for details).

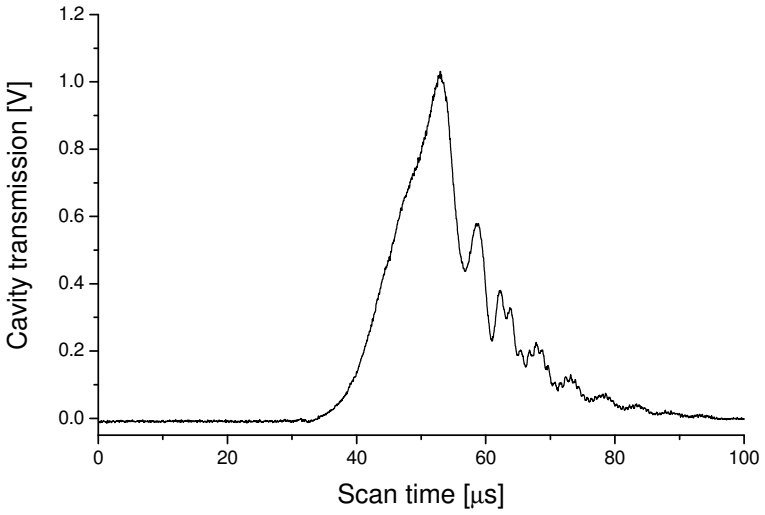

Figure 3.8: Cavity ringing and birefringence as seen from a single shot scan over the cavity resonance. The slow constant oscillation is the beat of the two cavity polarization modes, see Sec. 3.2.4, while the faster oscillations with increasing frequency represent the cavity ringing.

bends on the signal tail. Besides, the presence of several close resonance lines, e.g., of two polarization modes in our case (see Sec. 3.2.4), badly distorts the ringing signal and also prevents a robust finesse measurement compared to the CRD approach.

By very rapidly scanning the cavity, i.e. if the scan over the cavity resonance is much faster than the cavity decay, the cavity output does not show significant ringing, instead it changes into an exponentially decaying signal [88]. This effect can be used to realize

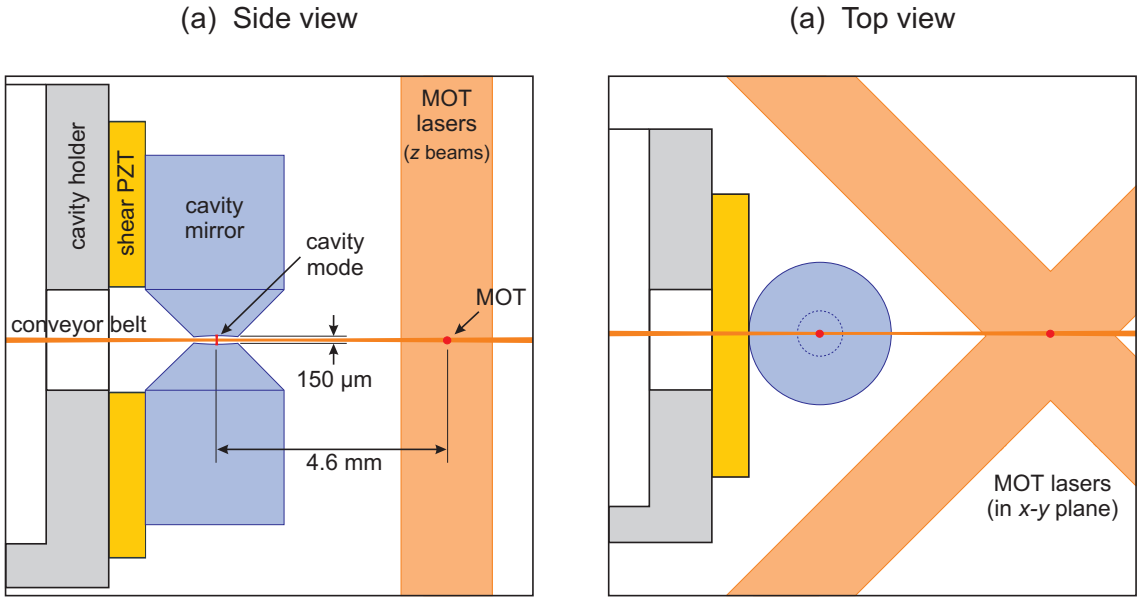

Figure 3.9: Schematic view of the high-finesse cavity integrated into our atom-trapping experiment. All elements and laser beams are approximately drawn to scale. Not shown dimensions are the waist of the MOT beams (1 mm), the MOT diameter (10 μm), the waist of the dipole trap beams (35 μm), and the cavity mode waist (23 μm).

a cavity ring-down experiment that does not require turning a probe laser on and off. Besides, it does not suffer from a scan non-linearity as in the case of the measuring finesse from a ringing decay. However, because of the fast scan, the probe laser will not have enough time to significantly excite the cavity mode resulting in a reduced signal amplitude of such a measurement.

The cavity ringing is a promising method of measuring the finesse of low-loss resonators. However, since our optical setup is better suitable for CRD-based measurements, we use the ring-down approach for determining reflectivity of our mirrors.

3.3 High-finesse cavity

Our cavity consists of two spherical mirrors with a radius of curvature of 5 cm on super-polished substrates with diameter of 3 mm coned to 1 mm at their tips. The cavity length is 156 μm, the high-reflectivity dielectric coating results in a finesse of about 10^6 at 852 nm. The cavity is assembled on a specially designed cavity holder, which allows us to integrate the cavity into our main atom-trapping experimental setup in a most efficient way and to align it onto the dipole trap, see Sec. 3.3.1. The cavity length is stabilized by means of a "lock chain", which is developed for transferring the stability of one of the cesium transitions to the high-finesse cavity, see Sec. 3.3.2. Finally, the cavity is fully characterized in a series of measurements, see Secs. 3.3.4–3.3.5.

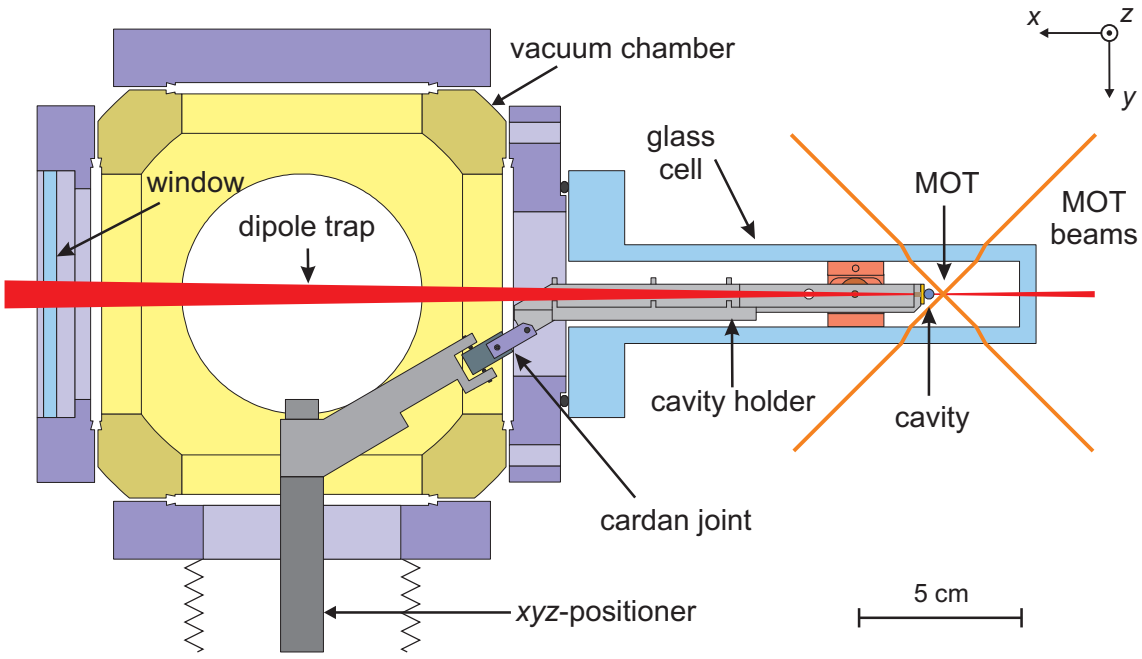

Figure 3.10: Cavity holder in the vacuum setup (top view).

3.3.1 Assembly

Integration into the atom-trapping experiment

We aim to use our dipole trap to transport one or few single atoms, initially cooled, trapped, and prepared at the position of the magneto-optical trap (MOT), into the mode of the high-finesse cavity. A schematic view of the integration of the high-finesse cavity into the atom-trapping experiment is shown in Fig. 3.9. To provide lossless atom transport, the cavity should be placed close to the MOT. At the same time, the relatively large mirror substrates should not block or disturb the laser beams composing the MOT. The distance of about 5 mm between the MOT and the cavity mode allows us both to efficiently transport atoms and not to interfere with the laser beams. Besides, the conical substrate shape leaves more space for the MOT laser beams in the x-y plane.

The cavity clearance should allow the high-power laser beams of the dipole trap to pass between the two mirrors without being scattered, absorbed, or significantly diffracted on their edges. For the waist of the dipole trap beams of $w_0 \approx 35 - 40\,\mu$m the chosen cavity length of $150\,\mu$m should be sufficient for this purpose.

Cavity holder

The main function of our cavity holder is to hold and locate the cavity mirrors inside our narrow glass cell about 5 mm away from the MOT, which is operating rather deep inside the cell, see Figs. 3.10 and 3.11. Two mirrors selected for maximum reflectivity and minimum birefringence are glued onto shear piezoelectric transducer (PZTs) attached to

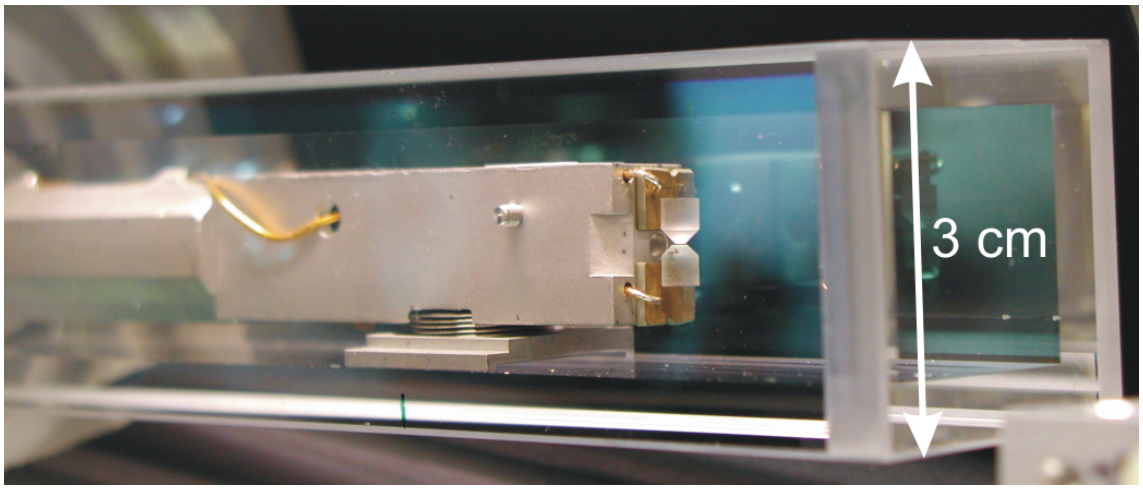

Figure 3.11: Assembled cavity integrated into the vacuum glass cell.

the aluminium holder. Details of the gluing procedure, including details on aligning the mirrors and controlling their separation, are described in Ref. [81].

After installing the cavity inside the glass cell and pumping out the vacuum chamber we have found that only one PZT has an electric connection to the outside of the chamber and thus can be used. Still, by driving one of the PZTs, the cavity length can be scanned over about one and a half of its free spectral range.

The long and rigid holder leaves enough space for the dipole trap beams and guides the electric wires from the PZTs. The position of the dipole trap is fixed by the MOT position and by a set of apertures for the DT beams placed outside the vacuum chamber. Thus, the cavity holder is made adjustable to permit the alignment of the cavity mode onto the dipole trap by moving the cavity in two dimensions perpendicular to the trap axis. For this purpose, the holder rests inside the glass cell on a short piece of bellows, acting both as a pivot and as a spring for crude vibration isolation of the cavity holder, and is connected via a cardan joint to a linear XYZ-positioner, consisting of a XY-manipulator and Z-feedthrough, as shown in Fig. 3.10. This combination allows us to adjust the cavity position with micrometer precision relative to the trap axis. Moving the cavity along the dipole trap, which is achieved by sliding the bellow on its support base, sets the desired distance to the MOT.

3.3.2 Frequency stabilization

Cavity QED experiments require a precise control of the resonance frequency of the cavity relative to the atomic transition frequency. The corresponding precision should be much better than the cavity linewidth. However, any instability of the cavity length, caused by, e.g., thermal drifts and mechanical (acoustical) vibrations, inevitable impairs the cavity frequency stability, since $\delta\omega/\omega = -\delta L/L$. Thus, if we would like to keep the cavity

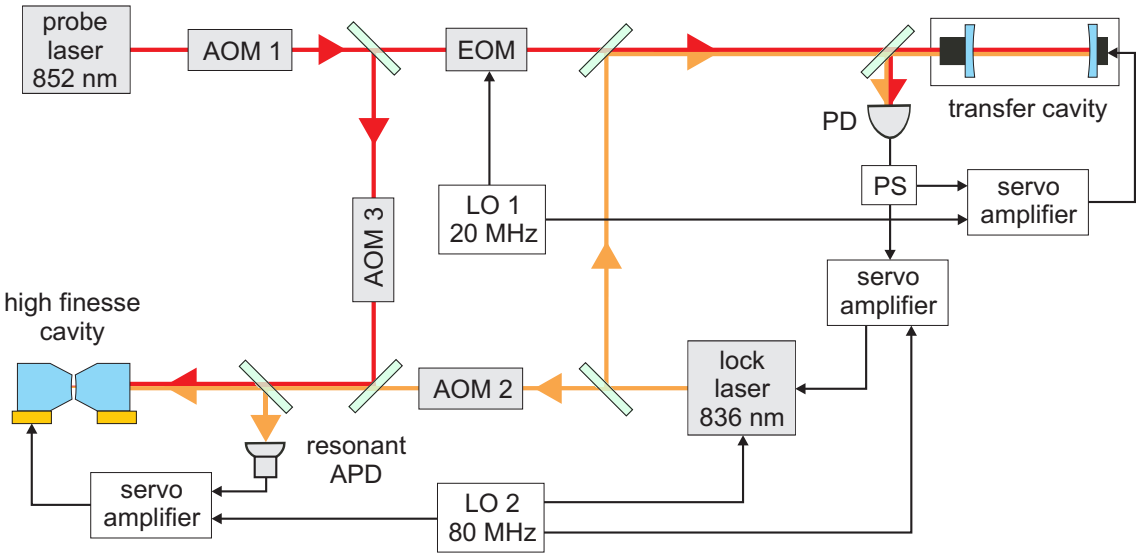

Figure 3.12: Frequency stabilization of the high-finesse cavity. AOM: acousto-optic modulator, EOM: electro-optic modulator, PD: photodiode, APD: avalanche photodiode, LO: local oscillator, PS: RF power splitter. The probe laser is stabilized to cesium polarization spectroscopy. The three servo amplifiers are based on the PDH method. All AOMs are set up in the double-pass configuration.

resonance stabile to within a fraction A of its linewidth, the stability of the cavity length should be better than

$$\delta L = \frac{A\lambda}{2\mathcal{F}}. \tag{3.17}$$

For a high-finesse cavity with $\mathcal{F} = 10^6$ and a required relative stability of, e.g., $A = 0.1$ we need a stability of $\delta L = 43$ fm.

The cavity's resonance frequency is locked to a reference "lock" laser using the Pound-Drever-Hall (PDH) method [89]. This method utilizes a phase-modulated lock laser and derives an error signal for an electronic servo loop by demodulating the laser power reflected off the cavity and detected by a fast photodetector. Our locking scheme for the stabilization of the high-finesse cavity is similar to the one used in the group of J. Kimble [90]. The components and performance of our setup are described in detail in Ref. [80, 81] and summarized in Ref. [51]. Here, I present a short overview of the main lock elements, schematically depicted in Fig. 3.12.

The lock laser is a diode laser in Littrow configuration emitting at 836 nm. The chosen laser frequency is far blue-detuned with respect to the D_2 transition line of cesium, which insures a small scattering rate of an atom in the cavity, as it is required for cavity QED experiments (for more details on the influence of the lock laser on trapped atoms see Sec. 4.5.1). Yet, this frequency still lies within the window of high reflectivity of the mirror coating, providing the high finesse necessary for cavity stabilization. Because of the absence of easily accessible atomic frequency standards at this wavelength, the lock laser is locked to an auxiliary cavity, which transfers the frequency stability from the stable

probe laser to the lock laser. Both servo loops for locking the transfer cavity and the lock laser are based on PDH method.

The probe laser is derived from the cooling laser used to drive our magneto-optical trap, see Sec. 1.2. Its frequency is locked to the crossover signal of the $F = 4 \rightarrow F' = 3$ and the $F = 4 \rightarrow F' = 5$ transitions using a Doppler-free polarization spectroscopy [91, 92], such that its frequency lies about 225 MHz below the $F = 4 \rightarrow F' = 5$ transition. This laser is used both as a reference laser for locking the transfer cavity and as a probe laser for the cavity QED experiments. The part of the beam which is used for locking is phase-modulated by an EOM resonantly driven at 20 MHz. The reflection off the transfer cavity is detected with a fast photodiode. A servo amplifier extracts and amplifies an error signal, which is then sent to a piezoelectric actuator attached to the transfer cavity, compensating for cavity frequency drifts.

The frequency modulation of the lock laser is realized by direct modulation of the diode current at 80 MHz. The reflection of the lock laser beam off the transfer cavity is detected with the same photodiode used for detecting the probe laser. After being demodulated and amplified, the PDH error signal is fed back to the grating and to the current of the lock laser.

Since in a high-finesse cavity the incident power of a resonant laser is drastically enhanced by a factor on the order of $\mathcal{F}/\pi$, we have to use the smallest possible lock laser power for locking our QED cavity in order not to affect a trapped atom. For instance, 170 nW of lock laser power coupled into the high-finesse cavity results in a scattering rate of 10 photons per second, see Sec. 4.5.1. For detecting a weak reflected lock beam we utilize a home-built avalanche photodiode followed by a resonant amplifier. After demodulation, the PDH error signal is processed by a proportional-integral servo amplifier, amplified by a fast low-noise high-voltage amplifier [51], and finally sent to the shear PZT supporting the cavity mirrors.

The acousto-optic modulator AOM 1 (see Fig. 3.12) is used to preset the frequency of the probe laser. AOM 2 is used to scan the locked high-finesse cavity with respect to the probe laser. The probe laser frequency can be tuned over the cavity resonance by means of AOM 3. In this way, both frequencies can be varied around the atomic resonance: the lock laser over about ± 100 MHz and the probe laser over about ± 200 MHz (see also Sec. 4.5.1).

Summarizing, the described stabilization scheme is sufficient to stabilize the resonance frequency of the high-finesse cavity to an atomic resonance with about 100 nW of coupled lock laser power. The residual frequency fluctuations are about $0.2\,\nu_{\mathrm{FWHM}}$ rms. The cavity remains locked during execution of different experimental sequences (see Chapter 4), even if they use optical shutters mounted to the optical table and producing mechanical disturbance to the cavity length. More importantly, the cavity lock can follow rapid thermal expansion and contraction of the mirror substrates caused by switching the strong dipole laser beams on and off within 100 ms.

3.3.3 Detection of the cavity transmission

The main information obtained in experiments, where a coupled atom-cavity system is probed by an external laser, is contained in the transmission of this laser through the cavity, see Sec. 4.2. Since the probe laser field must be very weak, we must be able to detect the transmitted probe power at the level of single photons. Below I present our optical setup allowing us to fulfil this task.

Coupling light into and out of the cavity

The optical setup around the cavity consists basically of two parts: one for stabilizing the cavity length and the other for detecting the transmission of the probe laser through the cavity. In the laboratory the whole setup is distributed over two optical tables connected by optical fibers. The first table contains the lock chain, except for the resonant APD and the high-finesse cavity, as well as the elements of the frequency and power control of the lock and probe lasers, see Fig. 3.12. The optical system for detecting the cavity reflection and transmission is located on the second table containing the vacuum chamber with the high-finesse cavity and the optical traps. Its main components are schematically shown in Fig. 3.13. They include the optics for coupling the probe and lock lasers into the cavity mode, detecting the reflection of the lock laser for locking the cavity, and separation and independent detection of the transmitted lasers.

Both lock and probe lasers are guided from the first table to the second one by means of one optical fiber. It provides perfect geometrical overlap of the beams, their high spatial stability, and nearly Gaussian spatial mode profile before the cavity. The combination of the two zero-order wave plates, $\lambda/4$ and $\lambda/2$, allows us to arbitrary set the polarization of the incoming lasers, for instance, for populating only one polarization mode of the cavity, see Sec. 3.3.4. Since the probe and the lock laser are coupled into the fiber in orthogonal linear polarizations, they also stay orthogonal before the cavity. The lasers are coupled into the cavity mode by using a mode matching lens system and a pair of mirrors. The reflection off the cavity is deflected by a non-polarizing 50/50 beam splitter (BS) onto the resonant APD, which is used for locking the cavity onto the lock laser, see Sec. 3.3.2. Being designed to detect and amplify only a signal modulated at 80 MHz, the resonant APD is not sensitive to the probe laser light.

After passing through the cavity and being again collimated, a part of the transmitted light is reflected by a removable BS onto a camera CCD 1. It provides information on the transversal mode structure of the two beams. In addition this camera allows us to observe the scattering of the DT laser beams off the cavity mirrors, which is very useful during the DT alignment, see Sec. 3.4. After the DT is aligned and the desired transversal mode of the probe laser is chosen, the BS is removed to avoid additional losses of the transmitted light.

Separating the two lasers

The lock and probe lasers with a wavelength difference of about 16 nm are spatially separated on a diffraction grating (Thorlabs Inc., model GR25-1210) ruled with 1200 lines/mm

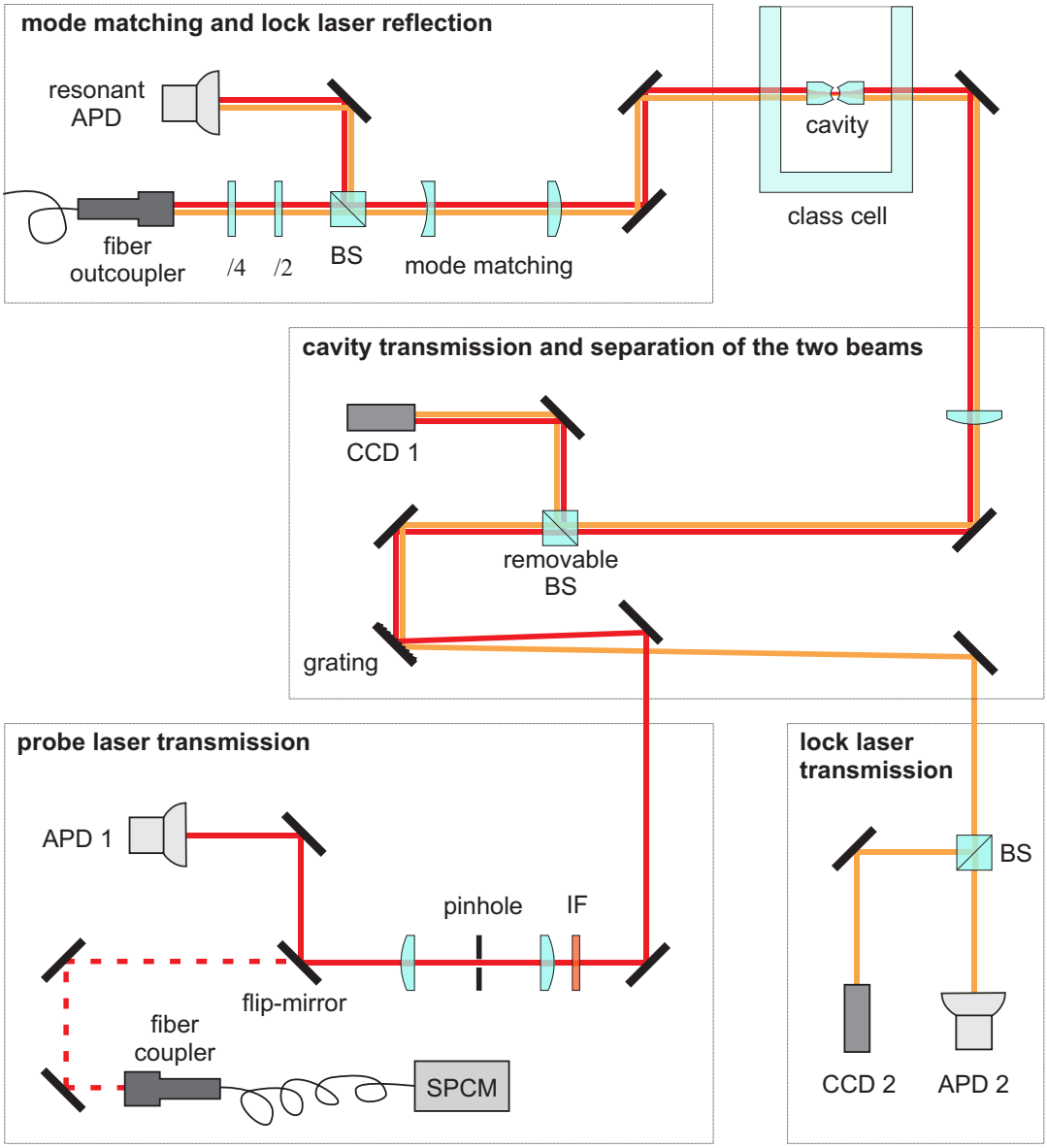

Figure 3.13: Schematic optical setup for coupling the lock and probe lasers into the cavity and detecting their transmission. BS: non-polarizing beam splitter, $\lambda/4$ and $\lambda/2$: quater- and a half-wave plate, respectively, CCD: infrared CCD camera, IF: interference filter, APD: avalanche photo-diode, SPCM: single photon counting module.

and a blaze wavelength of 1000 nm. The grating is set up in Littrow configuration, i.e. the incident angle is close to the blaze angle of 37^0. With the designed dispersion of 0.67 nm/mrad the beams are separated by about 10 mm after a distance of 40 cm from the grating. Having a waist of 1 mm they are then easily separated by mirrors. To increase the reflectivity of the grating surface, it is coated with gold. The measured diffraction

efficiency, η_{grating}, i.e. the relative light power in the first diffraction order, is 76(±2) % at 836 nm and 71(±2) % at 852 nm. The efficiency is polarization independent within the measurement uncertainty.

Additionally, the transmission of the probe laser is filtered by an interference filter (company "Dr. Hugo Anders"). It has a transmission of $\eta_{\text{filter}} = 0.77$ at 852 nm and about 10^{-4} for the 836 nm lock laser light.

Spacial filtering

The probe beam is spatially filtered with a 70 μm pinhole, installed at the focus between two convex lenses with 50 mm focal length. It helps to block stray light not originating from the cavity mode as well as parasitic scattering and diffraction off the ruled grating due to its spacing errors ("ghost" stray light).

If the cavity transmission is detected by the single photon counting module (SPCM, see below), additional mode cleaning is performed by coupling the transmitted light into a single-mode optical fiber directly attached to the detector via FC connector. The fiber is shielded from ambient room light by a furcation tubing. The typically achieved collection efficiency, η_{fiber}, of the fiber is about 60 % (fiber collimator from Schäfter+Kirchhoff, model 60FC-4-A18-02 with FC plug connection).

Detection of the transmission

In order to eliminate measurements when the cavity is not properly locked, we detect the transmission of the lock laser by an analog APD during all measurements. In the case of an unlocked cavity, the probe transmission drops to zero. Besides, the transmission is permanently monitored by the camera CCD 2 for visual inspection of the cavity stability.

The transmitted probe laser light is detected either by an analog APD or by an SPCM, see below. The choice of the detector is realized by a flip-mirror.

Analog APD

The first detector measuring the probe transmission is an avalanche photodiode (PerkinElmer, Si-APD, model C30902S) with a home-built transimpedance amplifier. The minimal measurable light power is about 1 pW, resulting in 4.9 mV of the APD output voltage with about 20 % uncertainty. The output of the APD saturates at about 4 V, while the APD's dark current causes a constant background of about 2 V. The high transimpedance of 100 MΩ limits the detector's bandwidth to 9 kHz.

The analog APD detector can be used with higher laser power than common photon-counting modules. This makes it an ideal detector for aligning purposes and in the measurements testing the overall performance of the experimental setup where an overexposure of the detector is not improbable. Besides, it is used to measure the transmission spectrum of the probe laser, its transversal mode spectrum, and the cavity polarization modes. All measurements in this chapter on cavity characterization as well as the first test experiments of Sec. 4.4 with transporting many atoms into the cavity have been performed with this detector.

Single photon counting module

To detect low laser intensities we use a single photon counting module (PerkinElmer, model SPCM-AQR-12-FC). Its maximum count rate is 10 Mc/s and the dark count rate is less than 500 c/s. The SPCM has an FC connector for attaching an optical fiber close to its active area. The measured photon detection efficiency, η_{SPCM}, of the SPCM is 0.30 at 852 nm and consists of the detector's quantum efficiency and of the coupling efficiency of the fiber light into the detector's active area. The total detection efficiency of the photons transmitted through the cavity is then

$$\eta_{\mathrm{total}} = \eta_{\mathrm{optic}} \cdot \eta_{\mathrm{grating}} \cdot \eta_{\mathrm{filter}} \cdot \eta_{\mathrm{fiber}} \cdot \eta_{\mathrm{SPCM}} \approx 0.089 \ , \tag{3.18}$$

where $\eta_{\mathrm{optic}} = 0.9$ denotes transmission of the light through all other optical elements on the beam path from the cavity to the detector (if the removable beam splitter is removed, see Fig. 3.13). The SPCM detector was used in experiments presented in Sec. 4.5 typically detecting 10–50$\times 10^3$ counts/s.

Cavity control software

During cavity QED measurements, the detectors' signals resulting from the detection of the cavity transmission for both lock and probe lasers are read out and stored on a computer for later data processing. For this purpose, the output voltages of the analog APDs are sent to two analog inputs of a high-speed data acquisition card (National Instruments, model PCI-6251). The output of the SPCM, which is put out as TTL pulses, are counted by a counter/timer card (National Instruments, model PCI-6601). Both cards are installed into a standard personal computer. During a high TTL gate input, which is sent by an experiment control software running the whole experiment [50], either the analog card digitalizes the APD signal of the probe transmission with a preset sampling rate or the counter card bins the photon counts detected by the SPCM with a preset bin time, depending on the detector in use. At the same time the analog card processes the signal from the lock laser APD. Both the sampling rate and the bin time are preset by the cavity control software and are typically 0.1–1 ms. In addition, the same software reads out the corresponding cards, plots traces of cavity transmission for both lasers, and saves them for their later analysis. Moreover, this software is used to detect the thermal drifts of the locked cavity relative to the probe laser and to compensate for them by controlling the frequency of the lock laser, for details see Sec. 3.5.

3.3.4 Characterization of the cavity

Length measurement

One of the most important cavity parameters is its length. It defines the free spectral range, the waist of the cavity mode, its volume, and consequently the atom-photon coupling strength. Before gluing the mirror substrates we tried to manually set their separation to about 150 μm while observing the mirror spacing under a microscope. However, the

gluing and baking processes can change the set separation. Therefore, the cavity length should be precisely measured again after the cavity is assembled.

A widely used method to determine the cavity length is based on a measurement of the transverse mode spacing, $\Delta\nu_{\text{transv}}$. For a symmetric resonator

$$\Delta\nu_{\text{transv}} = \frac{\arccos(1 - L/R)}{\pi}\frac{c}{2L}\,, \tag{3.19}$$

where R is the mirror's radius of curvature (see e.g. [79]). In approximation of a short cavity, that is for $L \ll R$, equation (3.19) can be rewritten as

$$L = \frac{2c^2}{(2\pi\Delta\nu_{\text{transv}})^2 R}\,. \tag{3.20}$$

Despite of its conceptual simplicity, a precise measurement of $\Delta\nu_{\text{transv}}$ for finding L usually requires a highly linear cavity scan, see e.g. [80, 86], which is difficult to realize. Indeed, the measured length of our cavity of 135 μm has a relatively large error of $\pm 20\,\mu$m, which results from the scan nonlinearity and uncertainty of the scan calibration.

To avoid scanning the cavity for measuring its length, we tune the laser through a full free spectral range of the cavity. The two corresponding wavelengths λ_1 and λ_2 satisfy the relation $L = n\lambda_1/2 = (n-1)\lambda_2/2$. Thus, the cavity length is given by

$$L = \frac{\lambda_1\lambda_2}{2(\lambda_2 - \lambda_1)}. \tag{3.21}$$

In this way, we have measured the cavity length of $L = 156.52(\pm 0.04)\,\mu$m. The free spectral range is $\nu_{\text{FSR}} = \nu_1 - \nu_2 = 957.7(\pm 0.3)$ GHz, corresponding to 2.3 nm at a 852 nm wavelength. The mode waist of the probe laser field, given by equation (3.5), is $w_0 = 23.15\,\mu$m, and the mode volume, given by equation (3.6), is $V = 65897\,\mu\text{m}^3$.

Note that the measured L is an effective cavity length, L_{eff}. It consists of the physical distance between the mirror surfaces, L_{phys}, which is an integer number of $\lambda/2$, and the penetration of the cavity electro-magnetic field into the multi-layer dielectric coating [86]. Thus, in general, n is not an integer and in our case $n_{852} \approx 367.4$ and $n_{836} \approx 374.4$.

Since the penetration depth depends on the wavelength, L_{eff} for the probe and lock lasers may differ. This issue becomes important for very short cavities, e.g., of $L \approx 10\,\mu$m used in Ref. [82]. In our case, the discrepancy between different L_{eff} is small and does not significantly influence the calculation of the cavity parameters important for us, e.g., such as a mode waist and an atom-photon coupling. However, in Sec. 3.5 we will see that the probe laser and the lock laser fields indeed have different penetration depths into the coating stack and, thus, see slightly different cavity lengths.

Finesse measurement

Generally speaking, the finesse of the assembled cavity differs from that measured with non-glued mirrors in the CRD setup in Sec. 3.2.3. If one is not careful enough, the mirror coating may be damaged and/or mirror surfaces may be polluted during the cavity

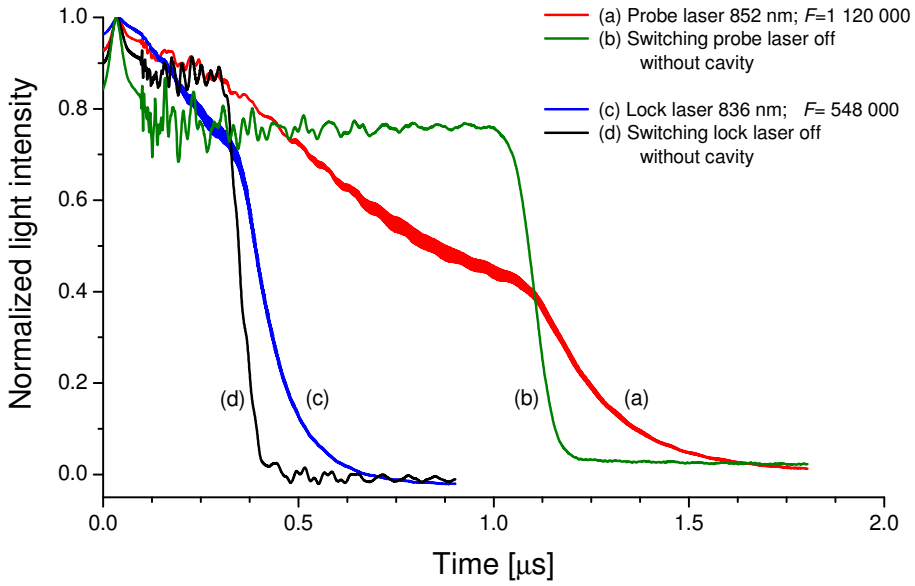

Figure 3.14: Cavity ring-down of the high-finesse cavity. The cavity decay time is measured for both the probe (a) and lock laser (c) wavelengths (852 nm and 836 nm, respectively). The influence of the detector bandwidth is investigated by recording the light intensity while switching off the both lasers without the cavity, see curves (b) and (d). Each trace shown is an average over about 20 single shots. All traces are normalized to 1 for better visibility.

construction, thus deteriorating their quality. In addition, the mode of an assembled cavity probes points at the mirror surface which are in general different from those tested with not glued mirrors.

The finesse of the assembled cavity is measured *in situ*, that is in the vacuum system, after the holder with the cavity is placed inside the glass cell. The method used is the cavity ring-down, introduced in Sec. 3.2.2. The measured cavity decay at both the probe and lock laser wavelengths, i.e. at 852 nm and 836 nm, respectively, is shown in Fig. 3.14. The difference in switching-off times for the two lasers comes from the difference in switching electronics and optics (including different AOMs) used for the probe and lock lasers. Each presented trace is an average over about 20 single measurements, normalized to 1 for easier comparison of different curves. From the measured decay times we get the cavity finesse at both wavelengths: $\mathcal{F}_{852\,\mathrm{nm}} = 1.12 \times 10^6$ and $\mathcal{F}_{835\,\mathrm{nm}} = 0.55 \times 10^6$ as well as the cavity linewidth at 852 nm of $\omega_{\mathrm{FWHM}} = 2\pi \times 0.85$ MHz.

Compared to the CRD measurements with a cavity of 1 cm length, presented in Sec. 3.2.2, the lifetime of photons inside the assembled 156 μm-long cavity is much shorter. This sets more stringent requirements on the bandwidth of the employed photodetector. For the current measurement we have used an avalanche photodiode with 9 MHz bandwidth. To investigate its influence on the form of the recorded CRD signal, we record the signal when the probe or lock laser are switch off without passing through the cavity. The observed drop-off times of the detected signal, see traces (b) and (d) in Fig. 3.14,

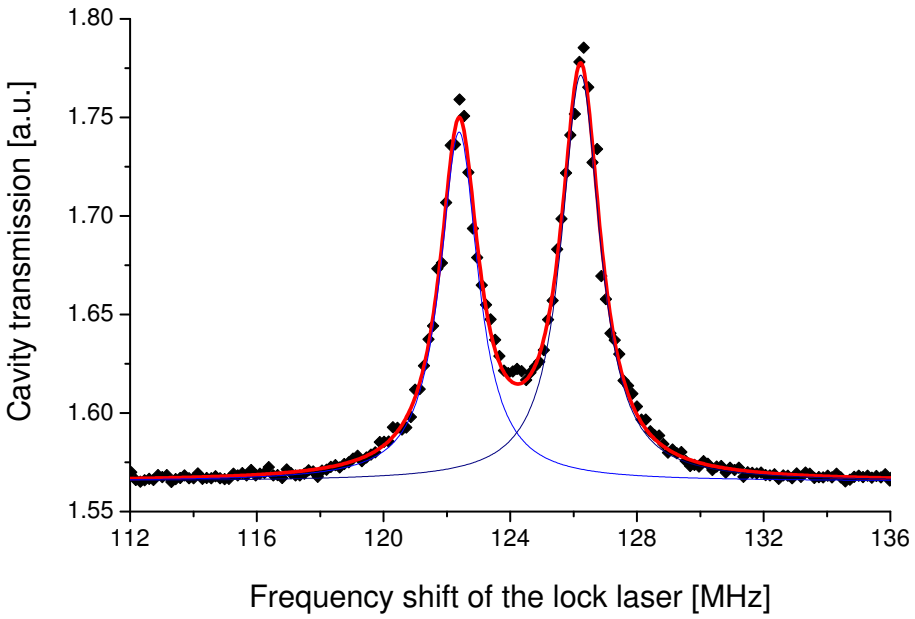

Figure 3.15: Birefringent modes of the cavity. The length of the locked cavity is scanned by sweeping the frequency of the lock laser. Two transmitted peaks correspond to two polarization modes of the cavity. The thick line is a fit to the data with a sum of two Lorentzian lines, resulting in a mode splitting of 3.86(±0.01) MHz. The peaks have a full width at half maximum of about 1.4 MHz.

are significantly shorter than the cavity decay time, thus justifying the utilization of the detector.

Birefringence measurement

Due to the gluing and backing processes, the stress-induced birefringence of an assembled cavity can be much larger than the inherent birefringence of the mirror coating, investigated in Sec. 3.2.4, and thus must be studied separately. In contrast to non-glued mirrors, we measure the birefringence of the assembled cavity from the splitting of the transmission peak by scanning the cavity. In order to eliminate drifts and fluctuation of the cavity length during the measurement, we lock the cavity to the lock laser. By slowly scanning the lock laser frequency using an acousto-optic modulator (in Fig. 3.12 denoted as AOM 2), the cavity length can be tuned while keeping the cavity locked. The cavity transmission recorded in a single shot is presented in Fig. 3.15. Here, we have scanned the AOM frequency over 14 MHz within 200 ms. For the better signal-to-noise, the input linear polarization of the probe light is set such that both polarization modes are approximately equally excited. This corresponds to input polarization rotated by about 45° degree relative to the birefringence axis of the cavity. The transmission spectrum is then fitted by a sum of two Lorentzian functions, resulting in a mode splitting of 3.86(±0.01) MHz. The measured linewidth at half maximum of 1.4 MHz is larger than $\omega_{\mathrm{FWHM}}/2\pi = 0.85$ MHz expected from the CRD measurement because of the finite linewidth of the lock laser.

The measured mode splitting is larger than that typically measured with unglued cavities in Sec. 3.2.4. According to equation (3.14), this difference is caused first of all by using here the shorter cavity length. From relation (3.15) we find the round-trip phase shift between the polarization modes of $\delta \approx 1.5 \times 10^{-5}$. Since we have not observed the birefringence with the unglued mirrors, which now compose our cavity, the intrinsic phase shift between polarization modes, if any, was smaller than 10^{-5}. The acquired birefringence results from the mechanical stress induced in the mirror substrates after gluing them and transmitted to the coated surface.

In general, the polarization direction of the birefringent modes depends on the symmetry of the induced mechanical strain. Since the glued surfaces of the mirror substrates are perpendicular to the cavity holder, the resulted strain, and thus the mode polarizations, should be symmetrical with respect to plane containing the axes of both the cavity and the holder. As expected, the measured polarizations of the two modes (see Fig. 3.15) are parallel and perpendicular to the holder axis, respectively. By setting the polarization of the incident light, we choose which cavity mode to excite. All experiments presented in Chapter 4 were performed with the probe laser polarized parallel to the cavity holder axis and, thus, to the dipole trap axis.

3.3.5 Mirror losses

Since high-finesse cavities strongly enhance the intra-cavity light, one should use very low light intensities for most cavity QED experiments in combination with ultra sensitive light detectors such as single photon counting modules. In this case any cavity losses other than mirror transmission reduce the valuable transmitted light power and thus significantly decrease the detection sensitivity. Below, I identify and measure the main losses of light in our high-finesse cavity.

A mirror can be characterized by three parameters, R, T, and A, the intensity reflection, transmission, and loss coefficients, respectively. Here, A includes both absorption and scattering losses. The coefficients are related through energy conservation by $R+T+A = 1$ and can be calculated by analyzing the cavity transmission and reflection of resonant laser light [82, 83]. Since the method presented below does not allow us to distinguish between the mirrors, in the following we suppose they are equivalent and thus have equal losses.

For a monochromatic light of a power P_{in} and a frequency ω incident on a Fabry-Perot resonator, the reflected power, P_{r}, and the transmitted power, P_{t}, are given by

$$\frac{P_{\text{r}}}{P_{\text{in}}} = \frac{R(1-R-T)^2 + 4R(T+R)\sin^2\frac{\phi}{2}}{(1-R)^2 + 4R\sin^2\frac{\phi}{2}}\,, \tag{3.22a}$$

$$\frac{P_{\text{t}}}{P_{\text{in}}} = \frac{T^2}{(1-R)^2 + 4R\sin^2\frac{\phi}{2}}\,. \tag{3.22b}$$

where $\phi = 2\pi\omega/\omega_{\text{FSR}}$ is the round-trip phase of the light field in the resonator and ω_{FSR} is its free spectral range. In case of resonance, $\phi = 0$ and equations (3.22b) and (3.22a)

are simplified to

$$\frac{P_\mathrm{r}}{P_\mathrm{in}} = \frac{(1-T-A)A^2}{(T+A)^2} \approx \frac{A^2}{(T+A)^2} \qquad (\text{for } R \approx 1)\ , \tag{3.23a}$$

$$\frac{P_\mathrm{t}}{P_\mathrm{in}} = \frac{T^2}{(T+A)^2}\ . \tag{3.23b}$$

For a resonator without absorption losses ($A = 0$), as usually considered in general textbooks on optics, these equations result in a total transmission of resonant light. However, if A cannot be neglected, we can calculate the mirror losses, T and A, by measuring powers P_in, P_r, and P_t. For this purpose, we make use of an additional equation connecting the cavity losses, which is based on a cavity finesse and reads

$$\mathcal{F} = \frac{\pi\sqrt{R}}{1-R} \approx \frac{\pi}{T+A} \qquad (\text{for } R \approx 1). \tag{3.24}$$

Unfortunately, in real experiments not all of the incident power P_in is coupled into a cavity TEM_{00} mode. If taking into account a mode matching factor, ε, the useful, coupled input power is reduced to $\varepsilon P_\mathrm{in}$, whereas a power $(1-\varepsilon)P_\mathrm{in}$ is directly reflected off the first cavity mirror without carrying any information on cavity properties. Consequently, the extended equations (3.23a) and (3.23b) should now read

$$\frac{P_\mathrm{r} - (1-\varepsilon)P_\mathrm{in}}{\varepsilon P_\mathrm{in}} = \frac{A^2}{(T+A)^2}\ , \tag{3.25a}$$

$$\frac{P_\mathrm{t}}{\varepsilon P_\mathrm{in}} = \frac{T^2}{(T+A)^2}\ . \tag{3.25b}$$

Finally, after making rearrangements in equations (3.23a)–(3.24), we get

$$T = \frac{2\alpha}{1+\alpha}\frac{\pi}{\mathcal{F}}\ , \tag{3.26a}$$

$$A = \frac{1-\alpha}{1+\alpha}\frac{\pi}{\mathcal{F}}\ , \tag{3.26b}$$

$$\varepsilon = \frac{P_\mathrm{t}}{P_\mathrm{in}}\frac{(T+A)^2}{T^2}\ , \tag{3.26c}$$

with a subsidiary parameter $\alpha = P_\mathrm{t}/(P_\mathrm{in} - P_\mathrm{r})$.

In our cavity setup, we measure the incident laser power P_in using a powermeter, and the powers P_r and P_t using calibrated APDs. For this purpose we scan the cavity length and determine the minimum cavity reflection and the maximum cavity transmission, respectively. Additional power losses on intermediate optical elements, e.g., on the glass cell, are approximately taken into account. The results of this measurement are summarized in Table 3.2. The estimated uncertainty of measured losses is about 10 %. A higher mirror absorption measured for the lock laser results from its deeper penetration into the dielectric coating compared to the probe laser.

Parameter		852 nm	836 nm
photon lifetime	τ	187 ns	91 ns
cavity finesse	$\mathcal{F}$	1 120 000	548 000
mirror transmission	T	1.3 ppm	3.6 ppm
mirror absorption	A	1.8 ppm	2.7 ppm
mode coupling	ε	36 %	41 %

Table 3.2: Measured mirror losses and mode coupling efficiency for the wavelengths of the probe and lock laser. Photon lifetimes and finesse are those measured with the CRD method in Sec. 3.3.4.

Because of the difference in Gaussian beam geometry for the probe and lock laser wavelengths, the cavity mode coupling for these beams slightly differs. Note that in experiments in Chapter 4 the mode coupling efficiency was about 55 %. Alternatively, the efficiency of the mode coupling has been determined by comparing the height of the fundamental TEM_{00} mode measured from the transmission spectrum of the cavity to the sum of the heights of all transversal modes which can be observed. This method has resulted in a coupling efficiency of about 80 % for the probe laser. The origin of the discrepancy between this value and that in Table 3.2 is unclear for us.

Intra-cavity intensity

Besides their importance for general mirror characterization, the mirror losses are necessary for calculating the intra-cavity light intensity affecting an atom coupled to the cavity mode. In analogy to equations (3.25a) and (3.25b), the intra-cavity power circulating inside a resonant Fabry-Perot resonator is given by

$$\frac{P_{\mathrm{intra}}}{\varepsilon P_{\mathrm{in}}} = \frac{T}{(T+A)^2} \ . \tag{3.27}$$

With (3.25b) this allows us to determine P_{intra} by measuring the transmitted laser power using the obvious relation

$$P_{\mathrm{intra}} = \frac{1}{T} P_{\mathrm{t}} \ . \tag{3.28}$$

Finally, from P_{intra}, we calculate the intra-cavity light intensity at an antinode of the standing wave of the cavity field as

$$I_{\mathrm{max}} = \frac{8 P_{\mathrm{intra}}}{\pi w_0^2} \ . \tag{3.29}$$

3.3.6 Conclusion

In the previous sections I have presented the construction and characterization of the high-finesse optical cavity applicable for the planned cavity QED experiments with trapped cesium atoms. The successful cooperation with a mirror fabricator during manufacturing the high-reflectivity mirrors allowed us to achieve a cavity finesse of about 10^6. After the additional investigation of their properties, we have selected the best mirrors for the cavity.

The specially designed cavity holder provides the efficient integration of the cavity into our atom-trapping experimental setup. Here, the cavity mode can be placed at 5 mm distance from our magneto-optical trap and, using the adjustable holder, can be precisely aligned onto the dipole trap. Our stabilization scheme is able to stabilize the resonance frequency of the high-finesse cavity to an atomic resonance with about 100 nW of coupled lock laser power. The residual frequency fluctuations are about $0.2\,\nu_{\mathrm{FWHM}}$ rms.

Finally, the assembled high-finesse cavity was characterized in a series of measurements. The basic properties of the cavity are summarized in Table 3.3.

Parameter		**Value**	**Comments**
Geometry			
cavity length	L	156.52 µm	effective, measured at 839 nm
radius of curvature	R	5 cm	specified by manufacturer
mirror diameter	D	1 mm	specified by manufacturer
cavity clearance	L_{c}	$\approx$ 150 µm	
TEM_{00} mode waist	w_0	23.15 µm	for light at 852 nm
mode size at the surface	w	23.17 µm	
mode volume	V	65 900 $\mu\mathrm{m}^3$	
Spectroscopic properties			
free spectral range	ν_{FSR}	957.7 THz	
finesse	$\mathcal{F}$	1 120 000	from CRD at 852 nm
	$\mathcal{F}_{836\,\mathrm{nm}}$	550 000	from CRD at 836 nm
linewidth	ν_{FWHM}	0.85 MHz	from CRD at 852 nm
polarization mode splitting	$\Delta\nu_{\mathrm{split}}$	3.86 MHz	birefr. axis along the holder
Cavity QED parameters			
atom-photon coupling rate	$g/2\pi$	18.0 MHz	for $F=4 \rightarrow F'=5$ with σ^+-polarized cavity mode
cavity field decay rate	$\kappa/2\pi$	0.43 MHz	from CRD at 852 nm
atomic dipole decay rate	$\gamma/2\pi$	2.61 MHz	decay rate for cesium atom
cooperativity parameter	C_1	146.7	

Table 3.3: Properties of the high-finesse optical cavity. For mirror losses see Table 3.2.

3.4 Interplay of the atom trap setup and the cavity

Being a massive object in the glass cell, the cavity with its holder can in principle influence our atom trap setup, even though it is placed far from the MOT center and the mirror spacing is larger than the size of the DT beams. Of course the atom traps can also affect the cavity performance. In the following I investigate the possible cross-influence of the atom trap setup and the cavity.

The MOT

The presence of the cavity does not noticeably prevent the normal operation of our single atom MOT: The cavity mirrors are located far enough from the MOT beams and thus do not noticeably block them, and the non-magnetic cavity holder does not influence the magnetic field of the MOT. However, the small scattering of the MOT lasers off the cavity mirrors increases the stray light seen by the APD detecting the MOT fluorescence rate (Sec. 1.2). In the absence of the cavity, the typical stray light-induced background count rate of the MOT APD is 2×10^4 counts/s. The presence of the cavity increases this number to about 7×10^4 counts/s. Of course, the fluorescence rate of a single atom stays the same, namely 3×10^4 counts/s. The increased background level results in an increased statistical noise of the detected fluorescence of the running MOT, thus decreasing the maximal faultlessly countable number of trapped atoms from 19 (see Ref. [56]) to about 10. However, since in the planned cavity QED experiments we aim on using few or even single atoms, the scattering of the MOT beams off the cavity mirrors does not constrain us.

Due to the spatial filtering of the probe laser beam transmitted through the cavity, this scattering is not visible on the APD detecting the cavity transmission and thus also does not influence our cavity transmission measurements.

Modification of the dipole trap geometry

The main demand on the geometry of the DT beams is a reasonably small beam size at the MOT position (to provide a deep trapping potential for efficient loading of the DT) and inside the cavity mode (to not clip the DT beams on the mirror edges). These two points are separated by 4.6 mm. The DT beams with a waist of $w_{\mathrm{old}} = 25.6\,\mu$m, which were used in the experiments described in Chapter 2, had a Rayleigh range of 2.0 mm. This small range would have resulted in a beam diameter of $128\,\mu$m inside the cavity, comparable to the clearance of $156\,\mu$m. Therefore, for the cavity experiments we have increased the beam waist to about $w_{\mathrm{new}} = 36\,\mu$m, extending the Rayleigh range to 4.0 mm, and have shifted the waist position midway between the MOT and the cavity mode. As a result, from now on the beam radius at these two positions is about $42\,\mu$m.

Due to the increased size of the DT beams at the MOT position the depth of the dipole potential for the same YAG laser power is smaller by a factor of $w_{\mathrm{new}}^2/w_{\mathrm{old}}^2 \approx 2.7$ than was, e.g., in Chapter 2. For atoms trapped in a shallower DT, the optical molasses illumination is more critical. For instance, a small imbalance in the intensities of the counter propagating illumination beams can push atoms out of a shallow trap, while in a deep trap such imbalance in light pressure is outweighted by a large dipole force holding

the atoms. Reducing the intensity of the optical molasses beams helps to keep the atoms trapped. However, it also reduces their fluorescence and thus the signal of the atoms seen on a CCD image. To overcome this difficulty we have performed an accurate balancing of the intensities of the MOT laser beams used for illuminating trapped atoms and increased the power of the trapping beams.

Note that for technical reasons described in Sec. 1.3 we have replaced the Nd:YAG laser (1064 nm) used in experiments of Chapter 2 by an Yb:YAG laser (1030 nm) providing up to 20 W output power in a single mode. Normally, in experiments in Chapter 4 involving imaging of atoms, we use about 3 W of the DT laser power per beam (in contrast to 1 W used in Chapter 2). According to equation (1.7), the resulting DT depth is about 1.4 mK.

The new beam waist of 36 μm was measured without glass cell by deflecting the beam under investigation sidewards. Its measured M^2-parameter is close to 1.0 indicating that the beam is close to a perfect Gaussian one [79]. After passing through the class cell and refocusing the DT beam by similar optics we measure a waist of 41 μm and M^2-parameter of about 1.2, although the divergence of the beam is the same as measured before the cell. Therefore we conclude that the vacuum system introduces additional aberrations to the beam. This can result in decreased DT laser power and increased beam width inside the cavity leading to a dipole trap depth smaller than the 1.4 mK calculated above.

Heating the cavity mirrors with the DT beams

We have observed, that some small fraction of the DT beams is clipped and absorbed by the cavity mirrors heating them even when the DT passes through the center of the cavity. Besides, due to the small cavity clearance of only 150 μm, it is difficult to avoid hitting the cavity and its holder with the powerful YAG beams while aligning the DT onto the MOT and then the cavity onto the DT. To estimate the possible damages to our cavity caused in this situation, we have investigated the thermal influence of the YAG beam on different cavity elements.

Several minutes of exposing a mirror substrate in air to the YAG beams with a power of 2 W, shined in on the substrate from a side, result in heating the mirror up to about 40–50 centigrade which is not harmful. However, because of the lower heat conductance of mirrors placed in vacuum, the mirror temperature in the glass cell can be higher and is difficult to estimate. Therefore, we try to avoid long direct exposure of the mirror substrates to the YAG beams.

We have tested that the same YAG laser power focused in air down to about 30 μm directly on a mirror surface (what is very unlikely to happen in the experiment) does not noticeably damage the mirror coating. Moreover, the damage threshold of the coating, as specified by the manufacturer, lies about 10 times higher. Furthermore, no damage is detected if focusing the laser onto the glue between mirrors and PZTs.

The most vulnerable element of the cavity assembly is found to be the gold-coated surface of the shear PZTs. If during beam walking the DT beam slides across the PZTs' surface, the laser immediately burns holes and traces on it. Of course, this should be strictly avoided by carefully performing the DT prealignment with low power.

Although we have seen that the DT beams going through the cavity spacing do not

damage the cavity, heating of the locked cavity can significantly shift its resonance frequency relative to the probe laser frequency and thus hinders our experiments. This problem and its solution are discussed in the next Sec. 3.5.

Aligning the cavity onto the DT

Due to the small size of our atom traps and their high sensitivity on all instabilities and thermal drifts of optical elements forming them, both the MOT and the DT beams should be accurately aligned at least once a day before performing any experiment with atoms. The presence of the cavity inside the glass cell complicates the alignment procedure of the DT beams. To avoid strong heating of the cavity and damaging the PZTs with the YAG laser beams while aligning them onto the MOT, their transmission through the cavity spacing is permanently observed. If we detect clipping of the beams, the cavity holder is displaced appropriately to let them pass between the cavity mirrors and the DT alignment is continued. Besides, an infrared CCD camera watching the cavity from the side monitors the YAG scattering off the cavity mirrors, thus giving us good qualitative information about the position of the cavity with respect to the DT beams.

After the DT is aligned onto the MOT and its position is fixed, we start to align the cavity relative to the DT. First, we set the right vertical position of the cavity by measuring the transmission of one of the DT beams through the cell while moving the cavity up and down. For large cavity displacements in both directions the transmission starts to decrease due to clipping of the beams. The optimal position is in the middle between these two regions. The estimated precision of this method is about $20\,\mu$m.

The alignment of the cavity in the horizontal plane transversely to the DT beams is more demanding, since the DT axis and the cavity mode should overlap precisely. This alignement is performed by using transported atoms as a probe for measuring the position of the cavity mode with micrometer precision. Several alternative experimental procedures for locating the mode are presented and discussed in Sec. 4.3.

Local vacuum between the mirrors

In general, the local vacuum between the two closely spaced cavity mirrors can be worse than the vacuum in the rest of the glass cell [93] due to outgassing of the mirror substrates. In order to make sure that the local vacuum here does not affect the trapped atoms, we measure the lifetime of atoms in the DT transported between the cavity mirrors. For this purpose, we move several (on average 5) atoms into the cavity with the probe and lock lasers switched off. After a variable waiting time we transport the remaining atoms back and count them by transferring the atoms back into the MOT. The experimental sequence is repeated 30 times. As a reference, we perform the same lifetime measurement without transporting atoms. The result is shown in Fig. 3.16. In both measurements the measured lifetime is about 10 s, mainly limited by phase noise of the AOMs used for shifting the standing-wave trap, see also Sec. 1.3. Consequently, the local vacuum between the cavity mirrors should not constrain our experiments.

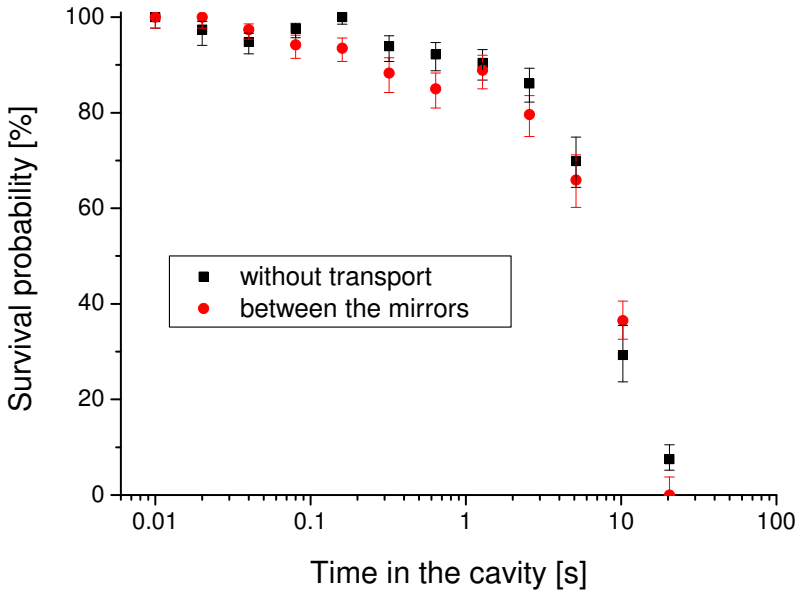

Figure 3.16: Lifetime of trapped atoms placed between the cavity mirrors (circles). For comparison the atom survival is also measured without transporting atoms into the cavity (squares).

3.5 Compensation of thermal drifts of the locked cavity

The laser beams of the dipole trap, while passing between the mirrors, are partially clipped and absorbed by the mirror edges. Since the index of refraction of the mirror coating is in general temperature dependent, the resulting heating of the coating changes the phase shift of the cavity mode light penetrating into it. If the cavity is locked, this phase shift is compensated by changing the cavity length, thus keeping the cavity always resonant with the lock laser.

Due to the difference in wavelength, the probe and lock lasers have different penetration depths into the mirror dielectric coating (the lock laser penetrates deeper) and thus their "thermal" phase shifts are different. As long as the mirror temperature stays constant, the constant differential phase shift can be corrected by slightly changing the frequency of the lock laser in order to bring the cavity in resonance with the probe laser.

However, during any experimental run consisting of many repetitions of some experimental sequence we repeatedly switch the DT beams on and off (e.g., for loading and counting atoms in the MOT). The rapidly alternating heating and cooling of the mirrors determine a new thermal equilibrium for the cavity which is approached after the experiment has been started. This equilibrium depends on the average DT laser power affecting the cavity during one repetition of the experiment and is thus different from that before the experiment was started. As a result, the cavity, while remaining stabilized to the lock laser, drifts away from the probe frequency. Hence, the probe laser transmission through the cavity drops during the successive execution of several experimental shots, as can be clearly seen in Fig. 3.17. In this measurement the duration of one shot is about 1 s with

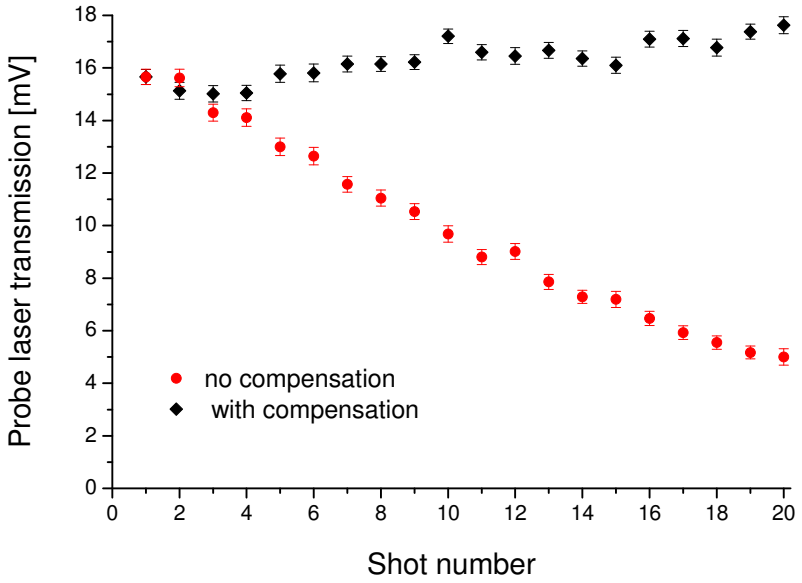

Figure 3.17: Probe transmission with (diamonds) and without (circles) compensation of the cavity thermal drifts. The transmission is measured for 20 successive experimental shots within one experimental run. The compensation method used is the center-of-mass method. A slight increase of the cavity transmission in (b) originates from a drift of the incident power of the probe laser.

the DT switched on about 60 % of the time. Before the experiment has been started, the DT laser beams were on continuously and the cavity was set in resonance to the probe laser. One sees that already after a few experimental shots the transmission is significantly decreased, making further execution of the experiment useless.

The differential thermal phase shift between the lock and the probe laser can be decreased by reducing the amount of the absorbed DT laser power. However, in our experiments this cannot be achieved by simple means. For instance, decreasing the DT laser power, what is the first natural candidate in reducing the cavity heating, will not allow us to take images of the trapped atoms without loosing them, see Sec. 3.4. Next, increasing the spacing between cavity mirrors will result in an undesirable decrease of the atom-photon coupling, see Sec. 3.1. Finally, decreasing the diameter of the DT beams will inevitably reduce their Rayleigh range, complicating the transport of atoms over several millimeter distances. Therefore, having no means to reduce the cavity heating, we can take it into account and try to actively compensate it.

Active compensation of the differential thermal phase shift

To actively compensate for the described thermal drifts of the locked cavity, we adjust the frequency of the lock laser during the experimental run in such a way that the cavity, being stabilized to the lock laser, stays resonant with the probe laser. The lock laser frequency is tuned by means of the AOM 2 shown in Fig. 3.12. The frequency of the AOM driver is

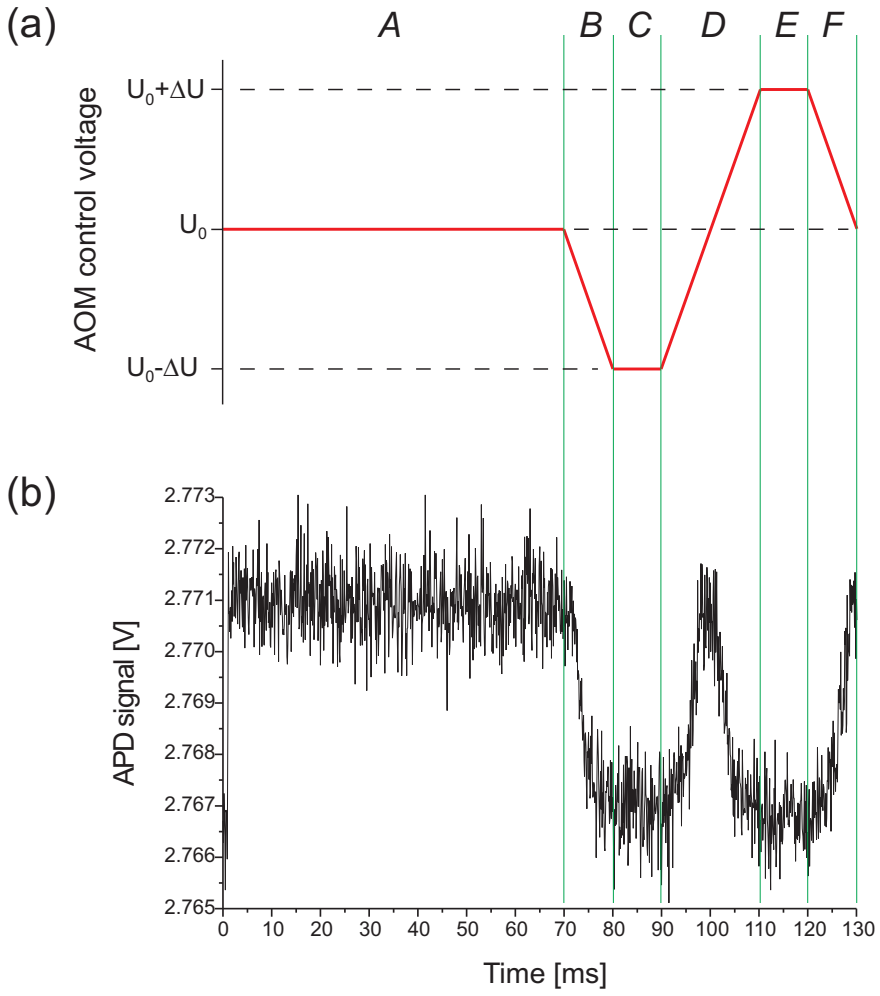

Figure 3.18: Compensating for the cavity thermal drifts resulting from switching the DT beams on and off. The time interval A is reserved for performing cavity QED experiments and can have an arbitrary length depending on the planned experiments. The intervals B to F are reserved for determining the optimal control voltage of the lock laser AOM which provides the maximum transmission of the probe laser. (a) Time dependence of the control voltage sent to the lock laser AOM. The initial optimal voltage U_0 is found from the previous experimental shot. (b) The corresponding cavity transmission of the probe laser as detected by the APD.

controlled via its VCO input by the PC analog output card.

The compensation procedure works as follows. After the cavity QED measurement has been performed and the atoms are moved out of the cavity mode we scan the cavity resonance over the probe laser frequency in a way depending on the specific compensation method, see below, and measure the cavity transmission of the probe laser. Then, we determine the AOM control voltage $U_{\max}$, which corresponds to the maximum transmission of the probe laser, and use its value in the next experimental shot.

Center-of-mass method

There are several algorithms to determine $U_{\max}$. The easiest one is to linearly scan over the whole transmission spectrum of the probe laser and to find the center of mass of the transmission peak. The realization of this method is illustrated in Fig. 3.18. Part (a) shows a time sweep of the AOM control voltage prepared for scanning the cavity and determining $U_{\max}$. Part (b) presents a typical cavity transmission signal corresponding to the cavity scan of (a). In this example the transmission is detected by an analog APD. However, the compensation methods described in this chapter work as well with a single photon counting detector.

The time interval A is reserved for the cavity QED part of the experiment and its length can be set arbitrary. The AOM voltage U_0, which is supposed to correspond to the maximum transmission $T_{\max}$ of the probe laser, equals $U_{\max}$, which was calculated in the previous shot. During the intervals B to F we determine a new optimal voltage $U_{\max}$ which will be automatically used for the next experimental shot. The probe laser transmission line is recorded in the time interval D. During the time intervals C and E we measure the background level.

After the whole voltage sweep A–F is executed and the corresponding cavity transmission is recorded, the cavity control software calculates the position t_c of the center of mass of the background-free cavity transmission and the corresponding AOM voltage $U_{\max}$. Then, it reprograms the PC analog output card with a new AOM voltage sweep similar to Fig. 3.18(a) with U_0 given by the newly found $U_{\max}$.

Two-point method

Our second method of finding the center position of the transmission peak, which has a Lorentzian form, is based on precisely measuring the transmission level at two points located on the opposite slopes of the transmission peak. Using these two values together with the maximum transmission and the background level, which are in general constant and thus are measured independently before the main experiment, we then determine the position of the peak maximum. To realize this method, we apply an AOM voltage scan similar to that of Fig. 3.18(a). The two transmission values are measured during the time intervals C and E, respectively. For this purpose, we use a small voltage span ΔV, corresponding to a half width of the transmission peak.

Results

The efficiency of the center-of-mass method (CMM) for compensating cavity thermal drifts is demonstrated in Fig. 3.17. We are able to keep the cavity transmission high in each experimental shot, making our experiments insensitive to the thermal drifts of the cavity. The cavity transmission compensated with the two-point method (TPM) looks very similar (within statistical errors) to that of CMM and thus is not shown here.

Although in this demonstration the results of the two compensation methods look similar, the methods differ significantly by their capture range ΔU. It defines the maximal thermal drift between two successive experimental shots, which can be compensated. In

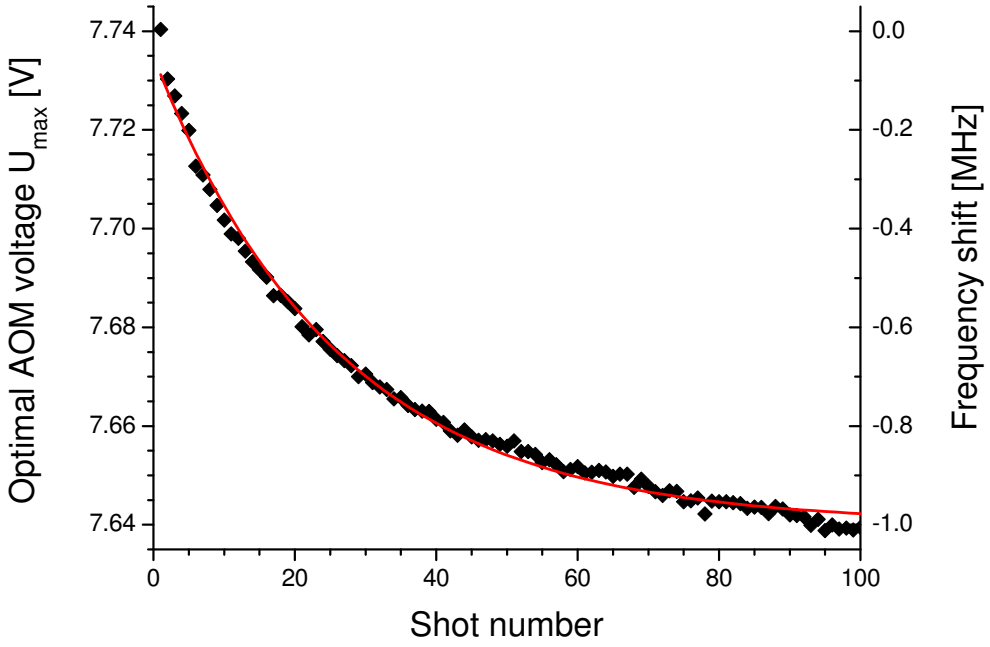

Figure 3.19: Re-thermalization of the locked cavity during an experimental run. One shot lasts 1.06 s. The straight line is an exponential fit with a decay time of 27.6(±0.6) s.

contrast to TPM having a small ΔU, the capture range of CMM can be set arbitrary large, depending on the experimental needs. However, being more sensitive to small transmission shifts, TPM gives a more precise peak position compared to CMM for the small thermal drifts, since it measures the signal at the most sensitive points (the slopes) of the transmission peak.

All experiments described in Sec. 4.5 have been performed with the robust center-of-mass method, although in the future, after improving the stability of the experimental setup and passively reducing the thermal drifts, see Outlook, we plan to use the more precise two-point method.

Re-thermalization of the cavity

The cavity re-thermalization during successive executions of many experimental shots can be explored by recording values of $U_{\max}$ determined in individual shots. Since the cavity is actively kept resonant with the probe laser, the change of $U_{\max}$ corresponds to the differential thermal phase shift in the cavity between the lock and probe laser. Figure 3.19 presents the re-thermalization in an experiment consisting of 100 shots. The graph shows the optimal AOM voltage $U_{\max}$ found in each experimental shot. The right vertical axis shows the corresponding frequency shift applied to the lock laser for compensating the thermal changes in the mirror coating. The duration of one experimental sequence together with the time interval between two successive shots is 1.060 s. The overall run duration is thus 106 s. The DT beams are switched on during 59 % of this time. The continuous

line is an exponential fit with a decay time of 27.6(±0.6) s. One sees that already after 20 shots the thermal drift of the locked cavity relative to the probe laser frequency is about 0.5 MHz, which is about a half-width of the cavity resonance line. This result is consistent with the decrease of the cavity transmission observed in Fig. 3.17 with no compensation applied.

Knowing the frequency shift, ν_{shift}, the differential phase shift can be found from the same formula as used for calculating the frequency splitting of birefringent modes depending on a round trip phase shift, see equation (3.14). This results in the following relation

$$\delta_{\text{therm}} = 2\pi\nu_{\text{shift}}\frac{2L}{c}\,. \tag{3.30}$$

Thus, the frequency shift of, e.g., $\nu_{\text{shift}} = 1$ MHz results from the phase shift between the probe and lock laser wavelengths in the cavity of $\delta_{\text{therm}} = 0.65 \times 10^{-5}$ rad.

Conclusion and discussion

All experiments described in Sec. 4.5 have been performed with the center-of-mass stabilization method. In this way the probe laser transmission was kept maximal even in experiments with almost 10 seconds long shots, see e.g. measurements of Fig. 4.19. Moreover, both methods have been successfully applied in experiments with very low probe laser power having a signal-to-noise (S/N) ratio of about 1.5. For comparison, S/N in Fig. 3.18(b) is about 6.5. If experiments require an even smaller probe laser power, the durations of the intervals *C*, *D*, and *E* can be increased in order to overcome the lower S/N. Alternatively, we can increase the probe laser power only during the compensation phase *B*–*F*, when the atoms are not affected by the cavity field anymore.

Although both stabilization schemes serve reliably, we still try to keep thermal drifts of the cavity as small as possible by leaving the DT beams switched on all the time, except for loading the MOT with atoms and collecting the MOT fluorescence. Furthermore, the beams are kept on even between execution of different experimental runs and between different experimental shots within individual runs. This helps to reduce temperature changes of the cavity mirrors.

In some experiments we might require the cavity not to be resonant with the probe laser, but instead to have a well-defined detuning relative to it. Still, we can use the described stabilization methods in order to find the exact position of the maximum of the laser transmission and only then shift the cavity by the required frequency relative to the probe laser by means of the lock laser AOM.

Summarizing, the developed stabilization schemes allow us to precisely control the cavity resonance frequency relative to the frequency of the probe laser in the presence of thermal heating and cooling of the cavity mirrors due to switching the DT laser beams on and off. This thermal changes result in different thermal expansion of the cavity seen by the lock laser and the probe laser. In this case, the cavity resonance, stabilized by the lock laser, moves away from the probe laser frequency due to thermal expansion or contraction.

Chapter 4

Deterministic atom-cavity coupling

4.1 Introduction

For several years all experimental progress in our research group has been achieved with the objective of realizing deterministic atom-cavity coupling. The developed optical conveyor belt allows us to transport a single atom or any small number of atoms over macroscopic distances [23, 24]. Besides, this transport has been demonstrated to preserve the coherence of the prepared atomic quantum state [19]. The realization of a quantum register on a string of trapped atoms [18] gives us the possibility to prepare and manipulate quantum states of individual atoms. Thus, in combination with the coherent transport, this should allow us to let atoms coherently interact at a location different from the state preparation and read-out, e.g., inside a remote high-finesse cavity.

The first version of the required cavity setup was developed in our group about 5 years ago [80]. During my thesis the assembly and test of the improved high-finesse optical resonator have been performed. Besides, several special techniques, such as the number-locked loading of the dipole trap [56] and the precise position control of single atoms [25], necessary for the deterministic manipulation of single atoms, have been developed. So now, after coming a long way, we are ready to tackle the long-expected goal of our group – the deterministic atom-cavity coupling.

This chapter starts with the basic theoretical backgrounds necessary for understanding the main properties of a coupled atom-cavity system (Sec. 4.2). Next, I describe several methods for precisely locating the cavity mode, which is necessary for placing atoms at the field maximum and thus for achieving the highest possible atom-cavity coupling (Sec. 4.3). In Sec. 4.4 I present the transportation of bunches of several atoms into the cavity and their coupling to the cavity mode. These experiments with many atoms helped us to better understand our new system as well as to test the compatibility of different components and techniques. Finally, the main result of my thesis – the deterministic transport and coupling of single atoms to the mode of a high-finesse optical resonator – is presented in Sec. 4.5.

4.2 Basics of cavity quantum electrodynamics

In this section I recall a basic theoretical approach how to treat a coupled atom-cavity system. It is based on the so-called Jaynes-Cummings model of the spin-spring interaction – coupling of a two-level system (atom) with a quantum harmonic oscillator (cavity mode) [2]. The Jaynes-Cummings Hamiltonian gives us the eigenstates and eigenvalues of the coupled system depending on the coupling strength and the respective frequencies of the system components. The contribution of dissipation present in any open physically realizable system is treated by using the density matrix formalism and solving the master equation [94]. This approach allows us to find the expectation values of the relevant operators describing the system as well as to calculate the modified spectrum in the presence of the coupling. A more detailed introduction into the cavity quantum electrodynamics system can be found, e.g., in Refs. [78, 95]. Concerning atom-photon interaction I refer to [96].

4.2.1 Atom-cavity coupling rate

The interaction between atom and cavity is based on the electric dipole interaction of the atomic dipole moment, $\mathbf{d}$, with the electric field of the cavity mode, $\mathbf{E}(\vec{r})$. The corresponding coherent coupling rate g can be introduced as

$$g(\vec{r}) = \frac{\mathbf{d} \cdot \mathbf{E}(\vec{r})}{\hbar} \,. \tag{4.1}$$

Due to the spatial structure of the cavity mode field, $\psi(\vec{r})$, the atom-cavity coupling rate is position dependent and can be expressed as

$$g(\vec{r}) = g_0 \, \psi(\vec{r}), \tag{4.2}$$

where g_0 is the coupling rate at the maximum of the mode. Considering the fundamental TEM_{00} mode of the cavity and neglecting the divergence of the Gaussian mode for the short cavity, we get

$$\psi(\vec{r}) = \exp\left[-\frac{x^2+y^2}{w_0^2}\right] \sin\left(\frac{2\pi z}{\lambda}\right). \tag{4.3}$$

Here, the oscillatory term indicates the standing-wave structure of the cavity mode with a wavelength λ along its axis (z direction) and the Gaussian term is the transversal mode profile of the cavity fundamental mode with a waist ω_0 (x and y directions).

The r.m.s. electric field amplitude of the vacuum in the cavity mode of a volume V and of an angular frequency ω_c is given by [97]

$$E = \sqrt{\frac{\hbar\omega_\mathrm{c}}{2\epsilon_0 V}} \tag{4.4}$$

with ϵ_0 denoting the permittivity of free space. Thus, using (4.1), the maximum coupling rate reads

$$g_0 = d\sqrt{\frac{\omega_\mathrm{c}}{2\hbar\,\epsilon_0 V}} \,. \tag{4.5}$$

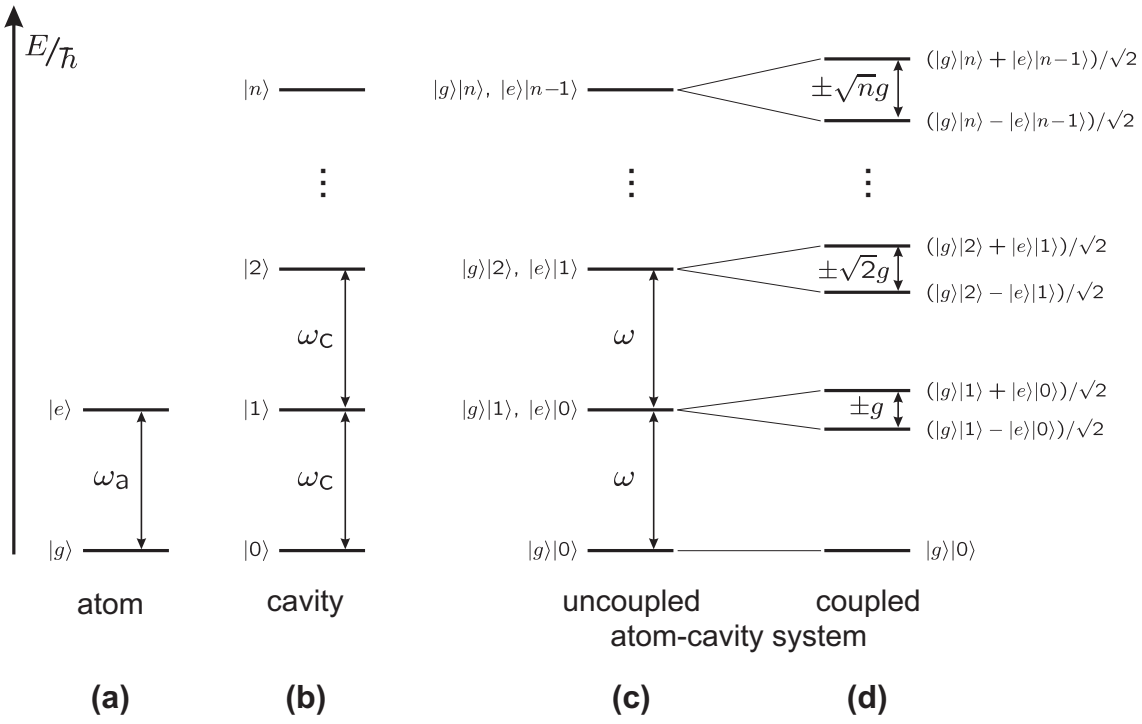

Figure 4.1: Eigenstates of the resonant atom-cavity system. For the resonant system, the frequency spacing ω coincides with ω_a and ω_c.

4.2.2 Jaynes-Cummings model

The Hamiltonian of a coupled atom-cavity system is generally expressed as a sum of three terms – atomic, cavity, and interaction:

$$H = H_\mathrm{atom} + H_\mathrm{cavity} + H_\mathrm{int}\,. \tag{4.6}$$

Let us consider a two-level atom with the ground and excited levels $|g\rangle$ and $|e\rangle$, respectively. The levels are separated by the energy difference $\hbar\omega_\mathrm{a}$ with ω_a the angular resonance frequency of the atomic transition as shown in Fig. 4.1(a). The Hamiltonian for the atom then reads

$$H_\mathrm{atom} = \sum_i E_i |i\rangle\langle i| \tag{4.7}$$

with E_i the energy of the atomic state $|i\rangle$. For convenience, we set the energy E_g of the ground state to zero.

In the following we introduce the atomic raising and lowering operators, $\sigma^\dagger$ and σ, defined as $\sigma^\dagger = |e\rangle\langle g|$ and $\sigma = |g\rangle\langle e|$. They describe the excitation and deexcitation of the atom, respectively, and their product $\sigma^\dagger\sigma = |e\rangle\langle e|$ gives the projection operator onto the atomic excited state. The atomic Hamiltonian can now be expressed as

$$H_\mathrm{atom} = \hbar\omega_\mathrm{a}\sigma^\dagger\sigma\,. \tag{4.8}$$

The Hamiltonian for the cavity mode with a frequency ω_c is given by

$$H_{\text{cavity}} = \hbar\omega_c\Big(a^\dagger a + \frac{1}{2}\Big), \tag{4.9}$$

where $a^\dagger$ and a are the field creation and annihilation operators, respectively. Their product corresponds to the photon number operator, $\widehat{N}$, defining the number of the excitations in the cavity. The energy spectrum of the cavity consists of equidistant photon number states $|i\rangle$ separated by the cavity resonance frequency ω_c, see Fig. 4.1(b). The ground state $|0\rangle$ is referred to as the vacuum state.

The interaction Hamiltonian based on the electric dipole coupling between the atom and the cavity reads

$$\begin{aligned} H_{\text{int}} &= \widehat{d}\cdot\widehat{E} && (4.10)\\ &= d(\sigma^\dagger e^{i\omega_a t} + \sigma\, e^{-i\omega_a t})\cdot E(a^\dagger e^{i\omega_c t} + a\, e^{-i\omega_c t}). && (4.11)\end{aligned}$$

Here, the dipole moment operator, $\widehat{d}$, and the electric field operator, $\widehat{E}$, are expressed via the atomic and cavity operators in the Heisenberg interaction picture. In the approximation $|\omega_a - \omega_c| \ll (\omega_a + \omega_c)$ the Hamiltonian (4.11) reduces to

$$H_{\text{int}} = \hbar g(\sigma^\dagger a + \sigma a^\dagger) \tag{4.12}$$

with g the coherent atom-field coupling rate, introduced above.

The total Hamiltonian of the atom-cavity system now reads

$$H = \hbar\omega_a\sigma^\dagger\sigma + \hbar\omega_c\Big(a^\dagger a + \frac{1}{2}\Big) + \hbar g(\sigma^\dagger a + \sigma a^\dagger) \tag{4.13}$$

and corresponds to the Jaynes-Cummings model [2] for a single two-level atom in an electromagnetic field in the absence of dissipation.

Without interaction, e.g., for $g = 0$, the levels $|g\rangle|n\rangle$ and $|e\rangle|n-1\rangle$ of the resonant uncoupled atom-cavity system are degenerate, having energy $n\hbar\omega$ with $\omega = \omega_a = \omega_c$, see Fig. 4.1(c). The coupling lifts this degeneracy and the new eigenstates of the coupled system are found by diagonalizing the Hamiltonian (4.13), yielding

$$|\pm_n\rangle = (|g\rangle|n\rangle \pm |e\rangle|n-1\rangle)/\sqrt{2}\,, \tag{4.14}$$

where n is the number of excitations in the system. The corresponding energy eigenvalues read

$$E_{\pm_n} = n\hbar\omega \pm \sqrt{n}\,\hbar g \tag{4.15}$$

and their spectrum is schematically shown in Fig. 4.1(d). The eigenstates with non-zero energy are symmetrically split by $2\sqrt{n}\,\hbar g$. The frequency splitting of the first excited state of $2g$ is called vacuum Rabi splitting. This frequency is also known as the single-photon Rabi frequency since it determines the energy exchange rate between the atomic dipole and the cavity electric field containing one photon. It is worthwhile mentioning that if N identical atoms are simultaneously coupled to the cavity mode, the vacuum Rabi splitting is increased by a factor of $\sqrt{N}$ and reads [78]

$$\Omega_{\text{Rabi}} = 2\sqrt{N}\,g\,. \tag{4.16}$$

4.2.3 Density matrix and master equation

The Jaynes-Cummings Hamiltonian describes a system in the absence of dissipation and driving, i.e. a closed system isolated from the environment. However, our system is subject to dissipation: The atom spontaneously decays into modes other than the cavity one with a dipole decay rate γ and the cavity photon leaks out of the cavity mode with a leakage rate κ due to finite transmission, absorption, and/or scattering on cavity mirrors. In addition, the coupled system can be probed by an external classical driving (laser) field. Thus, our experimental atom-cavity coupling can not be completely described by the Jaynes-Cummings Hamiltonian (4.13) alone.

In the presence of dissipation the atom-cavity system cannot be treated independently from the environment. The joint evolution of the atom-cavity-environment system can be treated using the Schrödinger equation with the joint Hamiltonian. However, since we are not interested in the environmental states, which are in general not known, we can trace over them if using the density matrix formalism. The time evolution of the open atom-cavity system is then described by the master equation [94, 98]

$$\frac{d\rho}{dt} = \mathcal{L}\rho \tag{4.17}$$

with the atom-cavity density operator ρ and the Liouvillian $\mathcal{L}$, which is defined as

$$\mathcal{L}\rho = -\frac{i}{\hbar}[H,\rho] + \widehat{C}\rho\,\widehat{C}^\dagger - \frac{1}{2}\widehat{C}^\dagger\widehat{C}\rho - \frac{1}{2}\rho\,\widehat{C}^\dagger\widehat{C}\,. \tag{4.18}$$

The Jaynes-Cummings Hamiltonian H now includes coherent driving of the cavity by a probe laser field $\varepsilon(t) = \varepsilon_0\, e^{i\omega_\mathrm{p}t}$ and can be expressed in a frame rotating at the probe frequency ω_p as

$$H = \hbar(\omega_\mathrm{a} - \omega_\mathrm{p})\sigma^\dagger\sigma + \hbar(\omega_\mathrm{c} - \omega_\mathrm{p})a^\dagger a + \hbar g(a^\dagger\sigma + a\,\sigma^\dagger) + \hbar\varepsilon_0(a + a^\dagger). \tag{4.19}$$

Dissipation is formally introduced in (4.18) by the collapse operator $\widehat{C}$ in the form [94, 99]

$$\widehat{C} = \sqrt{2\gamma}\,\sigma + \sqrt{2\kappa}\,a\,. \tag{4.20}$$

The two terms correspond to spontaneous emission from the atom and leakage from the cavity, respectively.

The master equation provides a valid description of the atom-cavity system in any range of parameters (g_0, κ, γ). In some limits it can be solved analytically, see e.g. [81] for the case of resonance between the atom and the cavity driven by a weak external field. In general we solve the master equation numerically by seeking for a steady-state solution for ρ such that $\mathcal{L}\rho = 0$. Since the expectation value of any operator $\widehat{O}$ can be found as

$$\langle\widehat{O}\rangle = \mathrm{Tr}(\rho\,\widehat{O}), \tag{4.21}$$

the density matrix provides us the complete information on the system. For instance, the intra-cavity field intensity is given by the expectation value of the photon number operator, $\langle\widehat{N}\rangle$, and thus the cavity output rate is $2\kappa\langle\widehat{N}\rangle = 2\kappa\,\mathrm{Tr}(\rho\,a^\dagger a)$.

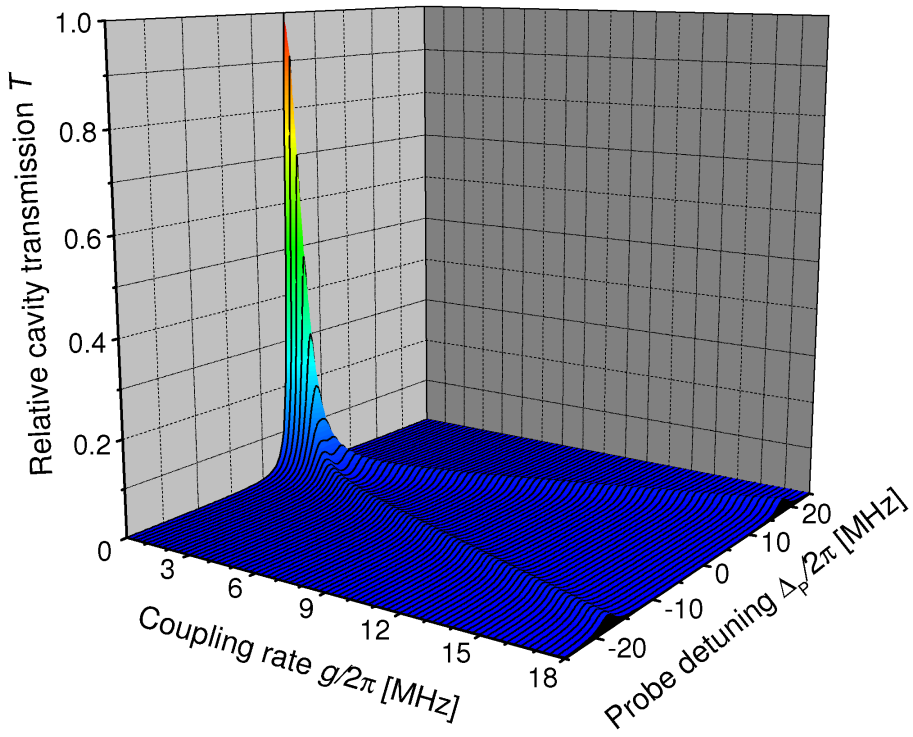

Figure 4.2: Vacuum Rabi splitting from a steady-state solution of the master equation for our experimental dissipation rates $(\kappa, \gamma) = 2\pi \times (0.43, 2.6)$ MHz. The system is probed with a weak external laser with a drive strength of $\overline{n} = 10^{-3}$ photons (i.e., the probe laser fills the resonant cavity mode with on average 10^{-3} photons).

4.2.4 Vacuum Rabi splitting

Before performing a numerical analysis of the master equation, we have to choose appropriate values of the main experimental parameters to use, namely the parameter set (g_0, κ, γ). Given by equation (4.5), the coupling rate depends on the atomic dipole moment and the mode volume. We consider the atomic cycling transition $|F = 4, m_F = \pm 4\rangle \rightarrow |F' = 5, m'_F = \pm 5\rangle$ in cesium. Its electric dipole moment reads

$$d = \sqrt{\frac{3\hbar\,\epsilon_0 \lambda^3 \Gamma}{8\pi^3}} = 3.167\, e a_0 \tag{4.22}$$

with λ and Γ denoting the wavelength and the natural line width of this transition, respectively. The cavity geometry gives us the mode volume of $V = 6.6 \times 10^4\ \mu\text{m}^3$, see Sec. 3.3.4, resulting in the coupling $g_0/2\pi = 18$ MHz.

According to equation (3.12), the decay rate of the cavity field is determined by the cavity finesse and for $\mathcal{F} = 1.12 \times 10^6$ equals $\kappa = 2\pi \times 0.43$ MHz. For a cesium atom $\gamma = 2\pi \times 2.6$ MHz. Consequently, the expected parameters of our atom-cavity system are

$$(g_0, \kappa, \gamma) = 2\pi \times (18, 0.43, 2.6)\,\text{MHz}\,. \tag{4.23}$$

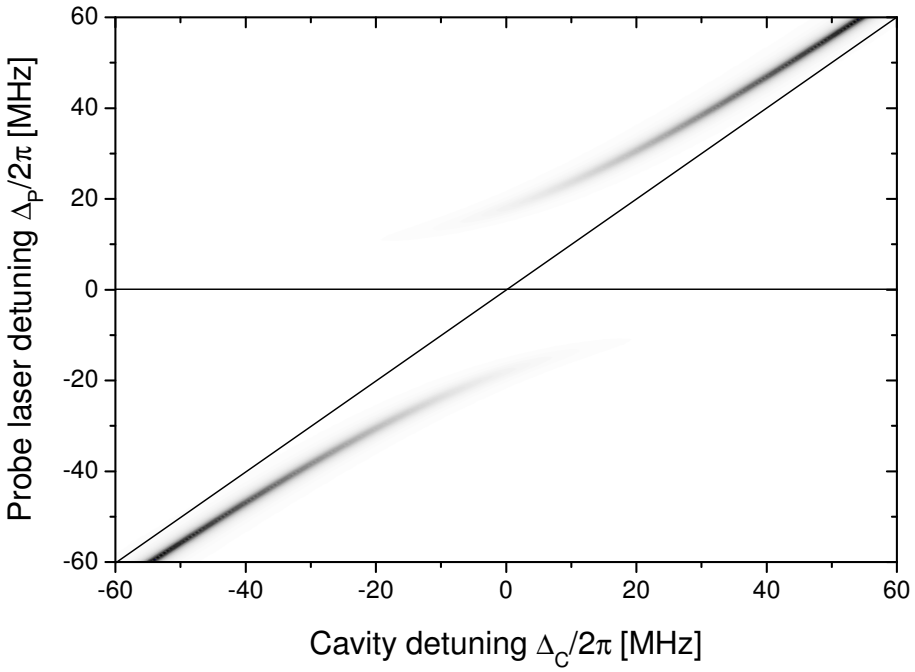

Figure 4.3: Energy levels of the coupled atom-cavity system for $(g_0, \kappa, \gamma) = 2\pi \times (18, 0.43, 2.6)$ MHz. The grey color gradient from white to black corresponds to the cavity transmission from 0 to 1. Two straight lines indicate the position of the uncoupled energy states.

Figure 4.2 shows the coupled atom-cavity transmission spectrum found via a steady-state numerical solution of the master equation (4.17) for the parameters (4.23). In this calculation the cavity is resonant with the atom and is driven by a weak probe laser. The transmission is calculated as a function of the coupling rate g and of the probe laser detuning from the atomic resonance $\Delta_\mathrm{p} = \omega_\mathrm{p} - \omega_\mathrm{a}$.

Without interaction between the atom and the cavity ($g = 0$), the transmission has a Lorenzian line profile of an empty cavity with a full width at half maximum of 2κ. As the coupling increases the peak splits into two lines reflecting the vacuum Rabi splitting (or normal-mode splitting). As predicted by equation (4.15), the splitting equals twice the coupling rate, i.e. $\Delta_\mathrm{split} = 2g$. The line width of the Rabi sidebands is given by twice the sum of all dissipation rates in the system, i.e. $\Delta_\mathrm{FWHM} = 2(\kappa + \gamma)$ [81]. The reduction of the height of the Rabi sidebands, T_Rabi, relative to the height of the Lorentzian peak, T_Lorentz, is given by

$$\frac{T_\mathrm{Rabi}}{T_\mathrm{Lorentz}} = \left(\frac{\kappa}{\kappa + \gamma}\right)^2 . \tag{4.24}$$

This relation is valid in the strong coupling regime when $g \gg (\kappa, \gamma)$ and does not depend on g. In our case of $(\kappa, \gamma) = 2\pi \times (0.43, 2.6)$ MHz, the reduced height of the sidebands is 2.0 % of the maximal. Note that a dependence similar to (4.24) has been observed in classical transmission of light through a Fabry-Perot resonator. According to equation (3.23b), the

presence of mirror absorption and scattering losses A reduces the cavity transmission by a factor of $T^2/(T+A)^2$. In the coupled atom-cavity system the atom with a decay rate γ plays a role of a photon scatterer, similar to A, leading to the same transmission law.

As seen from Fig. 4.2, the Rabi splitting cannot be observed if the coupling rate g is smaller than the system's linewidth, i.e. if $g \ll (\kappa + \gamma)$. In other words, in the weak-coupling regime the dissipation processes, represented by κ and γ, overwhelm the atom-field interaction, g. In contrast, if $g \gg (\kappa, \gamma)$, we get into the strong-coupling regime when the atom-cavity system has time to couple coherently before the energy in the system dissipates. This regime is of most interest for us since it allows us to explore coherent evolution in the atom-cavity system. The quality of atom-cavity system is often measured by the cooperativity parameter, defined as

$$C_N = \frac{N g^2}{2\kappa\gamma} \tag{4.25}$$

for N atoms simultaneously coupled to the cavity mode. It compares the atom-cavity coupling rate g with the cavity photon decay rate κ and the atom decay rate γ. Thus, in the strong coupling regime for one atom in the cavity $C_1 \gg 1$.

The transmission of the probe laser through the cavity detuned with respect to the atomic resonance is shown in Fig. 4.3. The two dark stripes of high cavity transmission represent the behavior of the energy states of the coupled system. The straight lines indicate the eigenstates of the uncoupled atom-cavity system: the horizontal and diagonal lines show the atom and the cavity resonances, respectively. In the resonance case of $\Delta_c = 0$, the spectrum demonstrates the vacuum Rabi splitting discussed above. The non-resonant atom-cavity coupling (i.e. in the so-called dispersive regime) of $|\Delta_c| = |\omega_c - \omega_a| \gg g$ results in a shift of the cavity resonance with respect to the empty-cavity by [78]

$$\Delta_{\text{shift}} = \frac{g^2}{\Delta_c}\,. \tag{4.26}$$

4.2.5 Atom oscillations in the dipole trap

Due to the finite atomic temperature an atom trapped in a potential well oscillates along its axial as well as two radial directions. Since the cavity field has a complex spatial structure, given by equation (4.3), an atom, which is placed into the cavity mode and simultaneously oscillates in the DT, experiences a time-dependent atom-cavity coupling rate, which is smaller than the maximum coupling g_0 given by (4.5). The axial oscillation (along the DT axis and the cavity holder) has a small amplitude due to the tight axial confinement in the standing-wave trap of better than $\lambda_{\text{DT}}/2 = 0.515\,\mu\text{m}$. Thus this oscillation does not significantly change the atom-cavity coupling.

In contrast, the radial atom confinement is weaker due to the larger radial extension of the trapping potential given by the width of the DT beams, $w_{\text{DT}} \gg \lambda_{\text{DT}}/2$. In harmonic approximation the radius of the atomic spatial distribution can be found as [51, Eq. (2.62)]

$$w_{\text{rad}} = \sqrt{\frac{k_B T}{m\,\Omega_{\text{rad}}^2}} \tag{4.27}$$

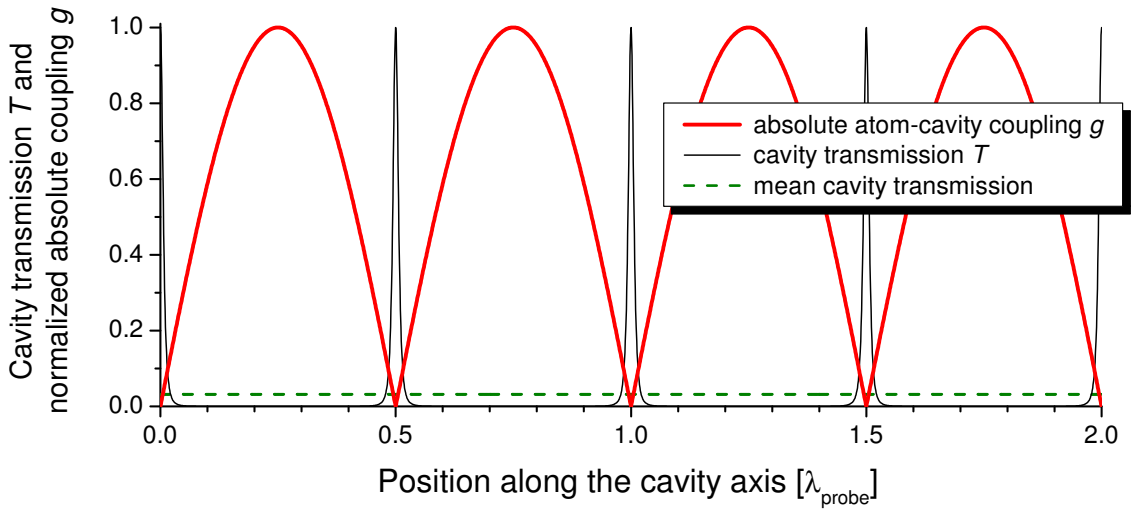

Figure 4.4: Expected cavity transmission for an atom oscillating along the cavity axis. If an atom would be permanently coupled to the cavity field with the coupling strength of $g_0/2\pi = 18$ MHz, we would expect no cavity transmission. However, due to oscillation of the atom, the expected mean cavity transmission is 3.2 % of the maximal one.

with T the atomic temperature and Ω_{rad} the radial oscillation frequency in the trap given by expression (1.16). For the realistic experimental parameters of $w_{\mathrm{DT}} = 42\,\mu$m and $U_0 = 1.4$ mK and supposing $T \approx 125\,\mu$K (the Doppler temperature),[1] we get $\Omega_{\mathrm{rad}} = 2\pi \times 2.3$ kHz and $w_{\mathrm{rad}} = 6.2\,\mu$m. Another way to determine w_{rad} would be to directly measure the width of the atomic fluorescence spot from the image of a trapped atom.

Since the oscillation amplitude w_{rad} is much larger than the periodicity of the cavity mode of $\lambda_{\mathrm{probe}}/2 = 0.426\,\mu$m, the atom oscillating in the DT along the cavity axis will probe all possible atom-cavity coupling strengths from zero to maximum. If the bandwidth of the transmission measurement is smaller than Ω_{rad}, which is the case in our experiment, the detected cavity transmission is an average over all possible transmission levels during one oscillation period.

To determine the mean transmission, we numerically calculate the cavity transmission while the atom moves along the cavity standing-wave mode. The numerical method is based on solving the master equation of the coupled atom-cavity system in the presence of dissipation, see Secs. 4.2.3 – 4.2.4. We consider the resonant case, i.e. when the cavity resonance, the probe laser frequency, and the atomic resonance frequency are all equal, and the maximum atom-cavity coupling strength of $g_0 = 2\pi \times 18$ MHz. The thick curve in Fig. 4.4 corresponds to the spatial variation of the coupling rate g along the cavity axis, which is proportional to the local field amplitude. The thin line is the cavity transmission, T, calculated for the local coupling g. Naturally the regions of high g and low T (and vice versa) coincide. The dashed horizontal line indicates the corresponding mean cavity transmission $\bar{T}$ of about 3.2 %.

[1] Note that the real atom temperature can be significantly different from the Doppler temperature due to complicated heating/cooling dynamics inside the cavity mode, see e.g. Sec. 4.5.3.

Let us now consider the radial oscillations of atoms transversal to the cavity mode (along y direction). Taking into account equations (4.2)–(4.3) and supposing for simplicity that an atom is trapped at an antinode of the cavity standing-wave field, the atom-cavity coupling rate along the y direction varies as

$$g(y) = g_0 \exp\left[-\frac{y^2}{w_0^2}\right]. \tag{4.28}$$

The average coupling experienced by an atom during its radial transversal oscillation can be found as

$$\overline{g} = \int_{-\infty}^{\infty} p(y)\, g(y)\, dy\,, \tag{4.29}$$

where $p(y)$ is the atomic distribution in the DT along y given by

$$p(y) = \frac{1}{\sqrt{2\pi}\, w_{\rm rad}} \exp\left[-\frac{y^2}{2w_{\rm rad}^2}\right]. \tag{4.30}$$

For our experimental parameters we get $\overline{g} \approx 0.965\, g_0$. Thus, the reduction of the coupling rate due to the radial transversal oscillations is 3.5 % and can be neglected compared to other effects reducing g_0.

In general, the coupling rate g can be smaller than the expected one, g_0, for instance because of not precisely placing the atom into the mode center. Moreover, the value of g_0 is calculated for the strongest transition in a cesium atom, namely between the outermost Zeeman states $|F=4,\, m_F=\pm 4\rangle \rightarrow |F'=5,\, m'_F=\pm 5\rangle$. Therefore, any mixing of m_F states (e.g., due to non-circular polarization of the probe laser) further reduces g and increases $\bar{T}$. For instance, if the maximal coupling is half the expected one, the mean transmission $\bar{T}$ is 6.4 % of $T_{\rm max}$. For the extreme case of $g = 0.1\, g_0$, $\bar{T} = 0.35\, T_{\rm max}$.

4.2.6 Conclusion

Summarizing, the presence of the atom-cavity coupling manifests itself via the splitting of the cavity transmission line in the resonant regime ($\omega_{\rm a} = \omega_{\rm c}$) or via the shift of the resonance in the dispersive regime ($|\omega_{\rm a} - \omega_{\rm c}| \gg g$). If the dissipation is strong, the broad resonance lines screen these spectrum changes. Whereas in the strong coupling regime, i.e. for $g \gg (\kappa, \gamma)$, the modifications to the spectrum of the coupled system are dramatic and should be directly observable.

In all experiments presented in this chapter (Secs. 4.4 – 4.5), we detect changes of the transmission of the probe laser through the cavity while transporting few or single atoms into and out of the cavity mode. The laser is resonant with the empty cavity providing high cavity transmission in the absence of atoms. Even one atom placed inside the cavity mode and coupled to it strongly modifies the system's spectrum and results in a reduction of the probe laser transmission. The degree of transmission changes gives us the information on the coupling strength in the system. Ideally, that is in the strong coupling regime, the transmission should completely vanish.

4.3 Locating the cavity mode

Obviously, after integrating the cavity holder into our main experimental setup, there are two main requirements to be fulfilled in order to allow deterministic transport of an atom into the cavity mode: The DT should pass through the center of the cavity mode and the position of the cavity mode along the DT axis should be known precisely. For that we first need to precisely locate the cavity mode relative to the DT and to the MOT. Then, we should move either the cavity or the DT beams such that the cavity mode perfectly crosses the DT axis.

The coarse pre-alignment of the cavity onto the DT is described in Sec. 3.4. Next, to locate the cavity mode precisely, we use transported atoms as a probe. Several experimental methods used for this purpose are presented below in the course of the section. Although using different physical processes, all of them are based on the interaction of trapped atoms with the probe laser coupled into the cavity.

After the separation between the cavity mode and the DT axis is determined, we make them intersect by horizontally shifting one of them or both. Large relative displacement can be achieved by moving the cavity horizontally, perpendicular to the DT axis by means of the 3-D positioner attached to the cavity holder, see Fig. 3.10. For displacements smaller than several tens of micrometer we shift the DT axis horizontally by synchronously tilting the last DT mirrors, see Fig. 2.8.

4.3.1 Using optical pumping

The cavity mode can be located by means of optical pumping induced by the probe laser which is coupled into the cavity and resonant with the atomic transition $F = 4 \rightarrow F' = 4$. Since the probe laser acts only on atoms in the $F = 4$ state, on average two scattered photons are enough to pump an atom placed inside the mode from the $F = 4$ ground state to $F = 3$. The maximum of the pumping efficiency measured for different cavity position relative to the DT and for different transportation distances indicates the location of the cavity mode.

Experimental sequence

The experimental sequence realizing this method consists of the following steps. First, we load the DT with several atoms and prepare them in the $F = 4$ state. For this purpose, we illuminate the atoms with the MOT repumping laser (resonant with the transition $F = 3 \rightarrow F' = 4$) for typically 10 ms after transferring them from the MOT into the DT. Then, we transport the atoms over a fixed distance towards the cavity mode excited by the probe laser. The power of the probe laser coupled to the cavity is typically 0.3 nW resulting in 0.16 mW intra-cavity power (see equation (3.27)). After a short waiting time of typically 1 ms, which is enough to pump the atoms placed at the field maximum to the $F = 3$ state, the standing wave is moved back to its original position. The hyperfine state of the atoms is detected by exposing them to a σ^+-polarized "push-out" laser, resonant with the $F = 4 \rightarrow F' = 5$ cycling transition [100, 19]. It pushes any atom in the $F = 4$ state out of the dipole trap, whereas atoms in $F = 3$ remain untouched and thus stay trapped. The

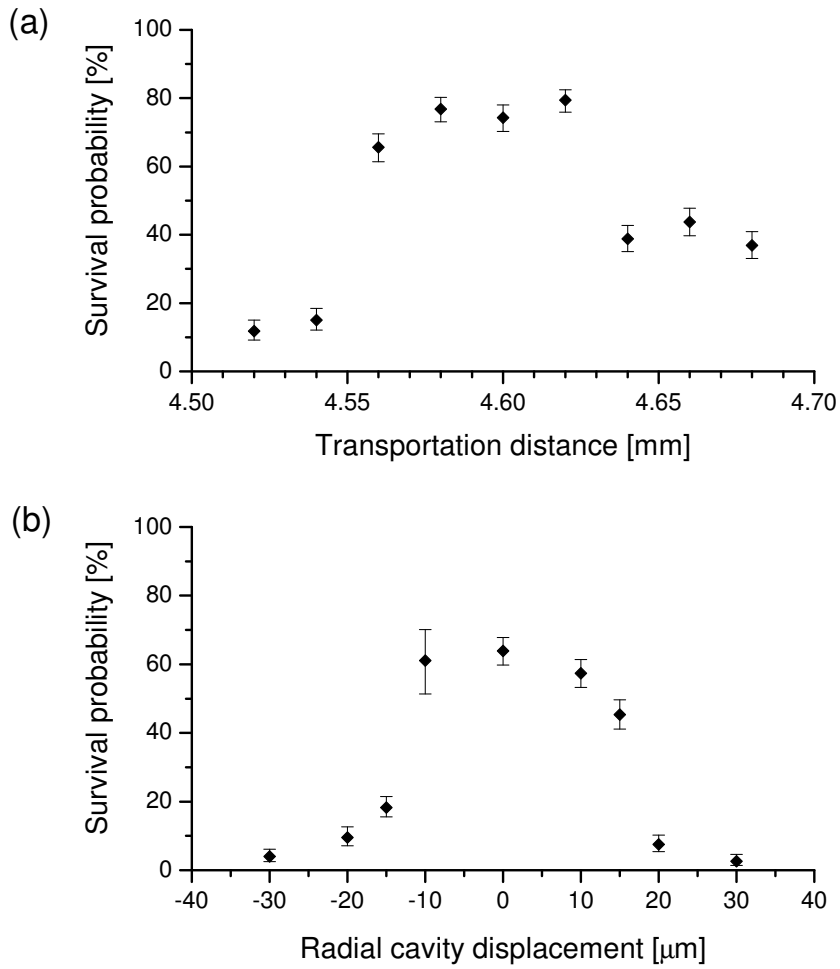

Figure 4.5: Locating the cavity mode using optical pumping by the probe laser. The measurement of the distance between the MOT and the cavity mode (a) and the alignment of the cavity mode onto the DT (b) are performed by maximizing the efficiency of the optical pumping for a fixed power of the probe laser.

survival probability of the atoms, which equals the probability of the population transfer between the two hyperfine states, is determined by transferring the surviving atoms back into the MOT and counting them there. The probability is measured for different radial position of the cavity relative to the trap and for different transportation distances. The maximum probability indicates the location of the cavity mode.

Results

The results of this method are presented in Fig. 4.5. Each data point contains a contribution from 30 experimental shots with on average 5 atoms each. In the first measurement (a) we vary the transportation distance. When it is too short, the atoms stop outside the cavity mode and stay unaffected by the probe laser. Thus, they do not change their $F = 4$

state and are subsequently removed out of the trap by applying the push-out laser. For the optimal transport, the atoms are pumped into the $F = 3$ state and thus remain trapped after the application of the push-out laser. If the transport is too long, the atoms are stopped on the other side of the cavity mode. However, they still temporarily interact with the cavity field while crossing it. That is why the survival probability for large distances is higher than that for short ones. To eliminate this asymmetry in the recorded signal, one can switch the probe laser on only when the atoms are fully stopped. Without applying the push-out laser, we detect about 80 % of atoms survived the loading of the DT and the transport. This determines the maximal survival probability measured here.

From the measured survival probability we determine the optimal transportation distance d_{trans} of 4.59($\pm$0.02) mm. Since after transferring the atoms into the DT they are spatially distributed along its axis over the size of the MOT of 10 μm, d_{trans} is defined here between the centers of the MOT and of the cavity mode. As long as the MOT size, which can be considered here as a size of our "atomic probe", is smaller than the error of d_{trans}, it does not influence the measurement precision for the present measurement statistics.

To precisely align the cavity mode onto the DT, we perform the same experiment with the fixed transportation distance of 4.59 mm, but for different radial displacements of the cavity (in the horizontal plane perpendicular to the DT axis). The result of this measurement is presented in Fig. 4.5(b). As in (a), the signal is saturated to about 70 %, measured independently. Yet, in contrast to (a), this signal is symmetric, since the atoms do not cross the cavity mode. By fitting the data with a Gaussian function we determine the optimal displacement of the cavity relative to its initial position set by a coarse prealignment with an uncertainty of about $\pm$2.0 μm. Although the choice of the fit function is arbitrary and does not properly describe the physics under the measured line form, it is still justified here for determining the center of the symmetric distribution.

The precision of both measurements presented is mainly limited by the statistical error and by the saturation of the measured signal, which broadens its maximum and makes it difficult to fit it with an appropriate peak function. The saturation can be reduced by using either a smaller probe laser power or a shorter waiting time in the cavity, whereas the statistical error can be decreased by using larger number of data points. Note that we cannot use much more atoms per shot, because of the impossibility of counting them in the MOT.

4.3.2 Using atom losses

The next two methods of locating the cavity mode do not require the manipulation of the atomic states, namely state preparation, optical pumping, and state detection. Instead, they are based on detecting the losses of atoms from the dipole trap induced by the intense probe laser coupled to the cavity mode and resonant with the $F = 4 \rightarrow F' = 5$ cycling transition of the trapped atoms. In both following methods we transport the trapped atoms over a known distance towards the cavity mode, induce strong scattering of the probe laser photons which leads to the heating of the atoms out of the DT, and detect their survival probability as a function of the transportation distance.

The easiest experimental sequence is the following. First, we load the DT with a

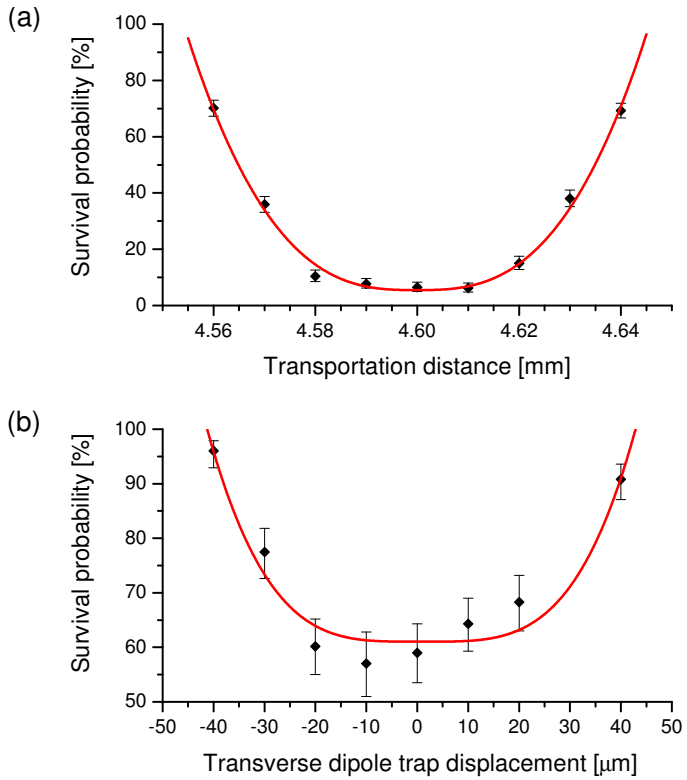

Figure 4.6: Locating the cavity mode by detecting atom losses induced by the intense probe laser. The trap displacement is measured relative to its original position set by the coarse DT pre-alignment. Straight lines are fits described by equation (4.31).

small known number of atoms, transport them over a known distance towards the cavity mode, switch on the probe laser for a time long enough to heat the strongly coupled atoms out of the trap, transport the surviving atoms back, and finally count them again after reloading into the MOT. In this way we measure the survival probability of the trapped atoms depending on the transportation distance. The maximum of the atom losses, i.e. the minimum survival probability, corresponds to the cavity mode position. To avoid atomic population in the $F = 3$ state, not coupled to the probe laser, we use an auxiliary repumping laser, resonant with the $F = 3 \rightarrow F' = 4$ transition and shined in along the DT axis during the experiment.

The measured dependencies are shown in Fig. 4.6. In (a) we vary the transportation distance. The graph (b) corresponds to the radial alignment of the DT onto the cavity mode. In contrast to the previous calibration method, where the cavity holder was displaced manually, here we displace the dipole trap axis in the horizontal plane (i.e. perpendicular to the cavity axis) in an automated way by synchronously tilting the last DT mirrors, see Fig. 2.8. Each point in (a) and (b) is measured from 20 shots with on average 14 and 5 atoms each, respectively. The difference in atom numbers results in different statistical errors in two graphs. The waiting time in the cavity is 10 ms. The intracavity

probe laser power in (a) is about 0.4 mW, whereas in (b) the power was slightly reduced in order not to saturate the measured minimum to zero.

To find the minimum of both dependencies we fit them with a suitably chosen fit function

$$y(x) = a\,|x - b|^{\,c} + d\,. \tag{4.31}$$

This function describes well the measured dependencies which do not show a prominent minimum, see straight lines in Fig. 4.6). The found optimal transportation distance is 4.610(±0.001) mm and the optimal DT alignment onto the cavity mode is found with a precision of about ±3.0 μm. Although the graph (a) is saturated almost to zero and (b) is not, the precision of the both measurements is about the same. As in the previous locating method, the transportation distance is measured between the centers of the MOT and of the cavity mode. The precision is better than that of the optical pumping method due to the use of a better fit function and can be increased by the same means, e.g., by increasing the number of the measured points.

Single atoms for probing the cavity mode

In principle, the two previous methods of locating the cavity mode are sensitive to the initial position of the atoms, since all of them are transported over the same distance towards the cavity regardless of their unknown initial locations. To get rid of this uncertainty we can use the technique of the precise position control of individual atoms for probing the cavity mode. Now, we load the the DT only with one atom using our number-locked loading technique (Sec. 1.4). Then, by means of our position control technique (Sec. 2.5) we shift the trapped atom to a chosen position along the DT axis close to the cavity mode which has to be probed. After switching on the intense probe laser, the standing-wave trap is moved back. As before, the survival of the atom is detected by loading it into the MOT. The typical calibration curves in this case look very similar to those shown in Sec. 4.3.2, although for achieving the same measurement error we can use about 5–6 times less atoms. However, requiring position control technique, this method takes longer experimental time because of the need to take an ICCD image for the initial position measurement.

4.3.3 Using losses of many atoms determined from CCD image

The last method we have developed for locating the cavity mode yields a small statistical error because of using a larger number of atoms and is insensitive to the initial atom position in the DT. As the previous method it is also based on detecting losses of atoms induced by the probe laser. However, here, the atom losses are detected by comparing two images of the trapped atoms recorded before and after transporting them towards the cavity, inducing their losses, and moving them back.

In the first step, we load a large number of typically several tens of atoms into the DT. To broaden their spatial distribution in the trap, which normally extends only over the MOT size of roughly 10 μm, we switch off one of the DT beams for 1 ms. In the absence

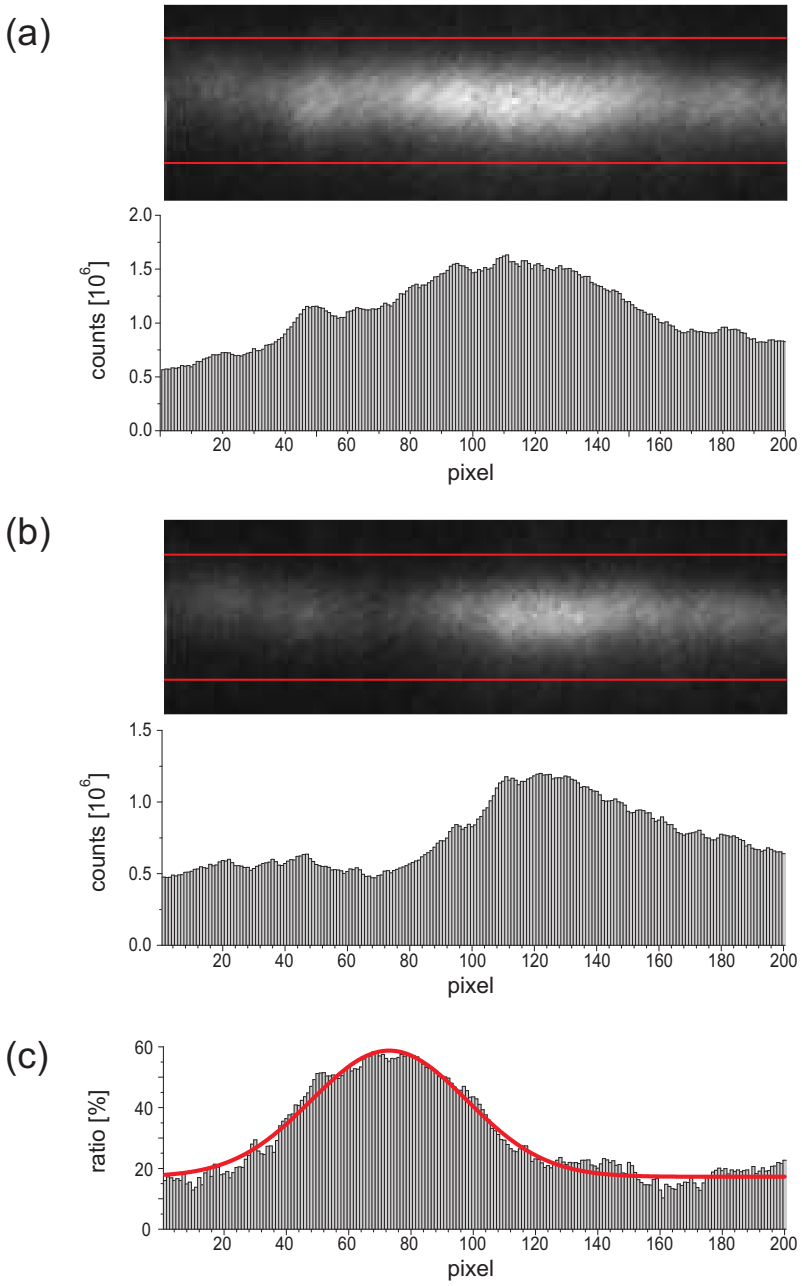

Figure 4.7: Locating the cavity mode by inducing the losses of many atoms and detecting them with a CCD camera. First, we load the DT with several tens atoms and take a CCD image of them. Then, we transport the atoms towards the cavity over a fixed transportation distance and induce their losses by shining in the probe laser through the cavity. Finally, we move the remaining atoms back and take the second image. We repeat this measurement 40 times and add up all initial images (a) and all final images (b). The atom losses are detected by building the ratio (c) of the two images. The position of the maximum losses corresponds to the location of the cavity mode. Note that here one CCD pixel corresponds to 0.4967 μm.

of the standing-wave structure, the atoms freely expand along the trap axis during this time. Next, we take a CCD image of the trapped atoms and then transport them over the fixed transportation distance of 4.6 mm in the direction of the cavity. By applying the intense probe laser for several milliseconds we remove those atoms from the trap, which are placed within the cavity mode. After transporting the remaining atoms back to their initial position we take the second image. For a better signal-to-noise ratio we repeat this experimental sequence 40 times and then add up all initial images and all final images.

The resulting two images are shown in Fig. 4.7. Image (a) shows the initial homogeneous distribution of the atoms along the DT axis. Yet, the final atom distribution in the image (b) has a dip corresponding to the absent atoms which were placed into the cavity mode and then lost after applying the probe laser. To analyze these images, we bin their pixel counts in the vertical direction within a narrow horizontal region denoted by two red lines. This procedure is the same as that applied for measuring the position of individual atoms, see Sec. 2.2. The obtained histograms are shown in Fig. 4.7 below the corresponding images.

To find the exact distribution of the lost atoms, we normalize the initial distribution of atoms onto their final distribution. For this purpose, we build a ratio of the initial histogram, N_{before}, to the final histogram, N_{after}, of the corresponding distributions after subtracting from them the background histogram, N_{bg}, as follows

$$R = \frac{N_{\mathrm{before}} - N_{\mathrm{bg}}}{N_{\mathrm{after}} - N_{\mathrm{bg}}} \,. \tag{4.32}$$

The background level N_{bg} is measured from the same images by binning their pixels within a horizontal stripe of the same width as that denoted by the horizontal lines, but located on the image away from the illuminated atoms. The obtained histogram R is shown in Fig. 4.6(c). A fit with a Gaussian function yields a peak position of $x_{\mathrm{peak}} = 36.46\,\mu$m with an uncertainty of $\pm 0.15\,\mu$m. Note that with this method we locate the cavity mode relative to the CCD image. Thus, for the transportation distance of $d_{\mathrm{tran}} = 4.6$ mm, the center of the cavity mode is located at a distance $d_{\mathrm{mode}} = x_{\mathrm{peak}} + d_{\mathrm{tran}} = 4636.5(\pm 0.2)\,\mu$m from the object point on the DT axis, which has the first pixel of the CCD camera as its image. The whole calibration procedure takes about 3–4 minutes.

Radial position of the cavity mode

To align the DT radially, i.e. perpendicularly to the cavity mode, we perform the experiment described above several times for different horizontal displacements of the trap axis. For each displacement we measure the height of the ratio histogram, see Fig. 4.8. The maximum of the measured dependence corresponds to the situation when the DT goes perfectly through the center of the cavity mode. Here, to determine the position of the maximum, we fit the data with a Gaussian function yielding the optimal DT position with a precision of $\pm 0.2\,\mu$m.

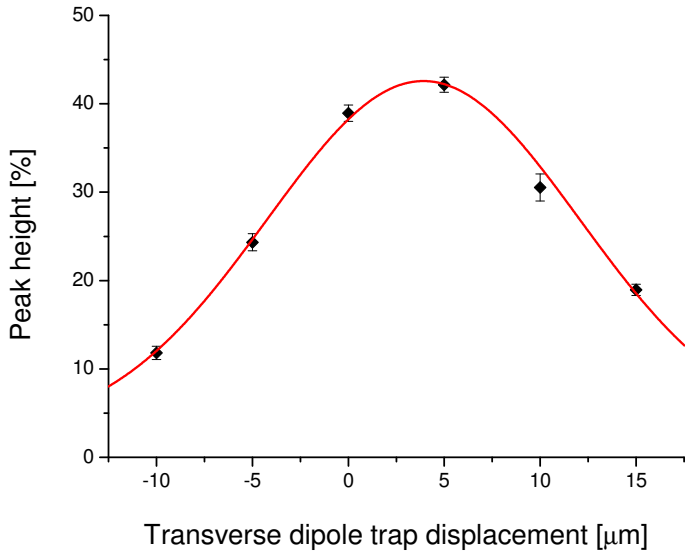

Figure 4.8: Aligning the DT onto the cavity mode using many atom losses. For each trap displacement we perform the measurement of Fig. 4.7 and determine the height of the ratio histogram (c). By fitting a Gaussian function to the obtained dependence, see the straight line, we determine the optimal horizontal alignment of the dipole trap.

4.3.4 Summary and discussion

Summarizing, we have developed and tested several different methods of locating the mode of our high-finesse optical cavity. Although all of them use atoms as a probe, they are based on different physical processes, use different experimental techniques, and have their own features and advantages.

The optical-pumping method is very sensitive to low laser intensities and thus can be also used to detect weak fields, i.e. weak light scattered off the mirrors. Besides, it is so-called background-free, since in the absence of the cavity mode or the light field the detected signal stays low.

The easiest in realization is the second method based on detecting the atom losses induced by the probe laser filling the cavity mode. It does not require the manipulation of atomic states and the only demand is to compare the final number of atoms with the initial one. In order to be not sensitive to the initial atom position in the DT, this method can be modified by applying the position control technique to precisely position single atoms inside the cavity mode. However, it requires the CCD camera and thus longer measurement times for getting sufficient statistics with single atoms.

Finally, the last calibration method allows us to use more (up to 10 times) atoms per shot, thus significantly reducing the statistical error of the measurement. Moreover, by taking CCD images of the atoms before and after the transport, we get not only the information about the survival probability of the atoms, but also about its position dependence. In this way, we effectively test all transportation distances simultaneously.

Because of the slow drifts of the experimental elements (the cavity holder, the DT mirrors, the ICCD camera, etc.) on the time scale of several days, the calibration of the mode position should be performed regularly. In the experiments described in the following part of this chapter we have alternately used all these methods, depending on the planned experiment. For instance, if the experiment does not require the use of the CCD camera, we calibrate the cavity position by the first two methods. In this way we do not need to look for the optimal parameters for illuminating the trapped atoms only in order to locate the cavity.

4.4 Transport of many atoms into the cavity

After the cavity is locked and its mode is located, we can tackle the main goal of the current research project – deterministic coupling of atoms to the mode of a high-finesse cavity and its detection. First, we examine our system with many (from few to several tens) atoms in order to qualitatively study the influence of different important experimental parameters onto the trapped atoms and the atom-cavity coupling.

For transporting several atoms we do not use the method of precise positioning of single atoms inside the cavity. Since the trapped atoms are distributed along the DT over about 10 μm (diameter of the MOT), after a correct transport all of them should be simultaneously coupled to the cavity mode, having a width of about 46 μm, although with different coupling rates. By transporting many atoms into the cavity, we are less sensitive to the local atom-cavity coupling strength experienced by each atom. Even if at least one of them is strongly coupled, the cavity transmission should completely vanish. Besides, according to equation (4.16), the simultaneous coupling of N atoms effectively increases the coupling strength by a factor of $\sqrt{N}$. Therefore, in our very first experiment we use several (on average 5) atoms and move them into the cavity mode while observing the transmission of the probe laser through the cavity, the decrease of which should be the evidence of atom-cavity coupling.

The experimental sequence consists of the following main steps. First, we load several atoms into the DT and optically pump them into the $F = 4$ ground state (the probe laser is resonant with the $F = 4 \rightarrow F' = 5$ transition). Then, we transport the atoms into the cavity mode while detecting the probe transmission through the cavity. After 3 ms waiting time the DT is moved back to its initial position and the remaining atoms, if any, are loaded back into the MOT and counted there.

One of the recorded transmission traces showing the complete vanish of the cavity transmission when the atoms are held inside the cavity is presented in Fig. 4.9. The transmitted probe power is measured with the analog APD, see Sec. 3.3.3. From its output voltage we subtract a constant background, which corresponds to the APD offset voltage and to not-filtered stray light. As indicated in the figure by the horizontal bar, the probe laser is switched on and then off again at about 1 ms and 14 ms, respectively, thus showing that the zero level indeed corresponds to no probe transmission. At 2 ms we start to transport the prepared atoms towards the cavity and after a 4 ms transportation

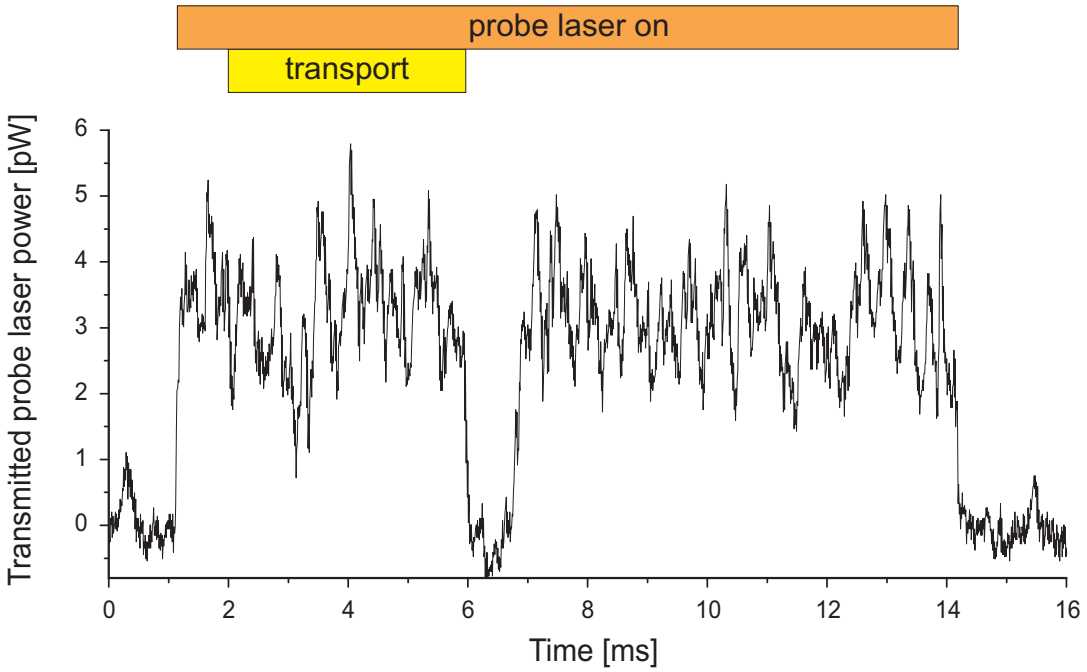

Figure 4.9: Vanishing cavity transmission in the presence of several (about 5) atoms in the cavity mode. The transmission of the probe laser is measured with the analog APD. Negative transmission appearing on the graph stems from subtracting the APD offset voltage and noisy stray light level from the measured signal. The atom transport starts at 2 ms and lasts 4 ms. The arrival of atoms into the cavity mode is accompanied by a vanishing probe transmission. After about 1 ms all atoms are lost and the high cavity transmission level is restored.

duration they arrive into the cavity mode. As a consequence of the atom-cavity coupling, the cavity transmission drops to zero at this moment.

The observed increase in transmission following the drop indicates that all atoms are lost from the DT. This is confirmed by detecting no surviving atoms in the MOT at the end of the sequence. On the other hand, about 90 % of the atoms survive the whole experimental sequence if the probe and lock lasers are blocked. Therefore, the atom losses are presumably induced by one or both of those lasers, as will be investigated below in Secs. 4.4.1 and 4.4.2.

Noteworthy, the increase of the transmission in traces, which show the transmission drop, is always sudden. This can be explained if a single atom leads to complete extinction of the transmission due to its strong coupling to the cavity mode. In this case, there is no transmission until the very last atom leaves the trap. However, if one atom does not saturate the cavity, the rapid transmission change can nevertheless occur if last atoms are lost so fast that the detection bandwidth does not allow us to resolve the intermediate transmission levels in the detected signal corresponding to different numbers of still coupled atoms. In the current experiment we cannot distinguish these two cases and only in Sec. 4.5 we will see that one atom does not make the cavity transmission vanish completely.

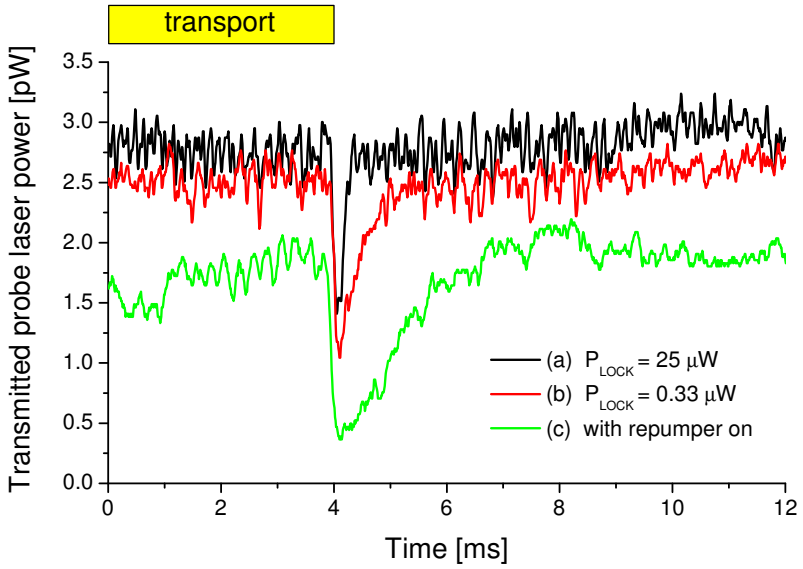

Figure 4.10: Influence of lock laser power and repumping laser on the transmission decrease. At 4 ms the atoms enter the cavity mode. The power of the lock laser coupled into the cavity is 25 μW in (a) and 0.33 μW in (b) and (c). An additional repumping laser is applied along the DT in (c). The transmission increase in each graph is not sudden as, e.g., in Fig. 4.9 because 64 individual traces have been averaged to yield each respective trace.

4.4.1 Lock laser and repumping laser

Different recorded and analyzed individual transmission signals have a different duration of the low-transmission phase. Yet, in some experimental shots no transmission drop is observed at all. In order to quantitatively characterized the observed transmission changes, we repeat the same experimental sequence many times and then average the measured APD signals. The result of averaging over 64 single traces for three different sets of experimental parameters is shown in Fig. 4.10.

In the measurement (a) the lock laser power coupled into the cavity is 25 μW. The transmission does not completely vanish when atoms enter the cavity mode at 4 ms indicating that not all traces out of 64 had a transmission drop to zero. The observed increase in transmission following the drop reveals the loss of all atoms within less than 0.3 ms.

Suspecting the lock laser to be one of the reasons for the atom losses, we reduce its power to about 0.33 μW in the next measurement (b). Indeed, the drop duration is extended to about 1 ms, although it is still short. After 3 ms we move the standing wave to its initial position and detect that about 25 % of the atoms have survived the whole experimental procedure, although the initial transmission level in Fig. 4.10(b) is quickly restored. This surprising result can be explained by optical pumping of the atoms into the $F=3$ ground state. The pumping is induced by the probe laser, which off-resonantly excites the atoms into the $F'=4$ state, from where their are free to decay into the dark $F=3$ state. There the atoms are not sensitive to the cavity field, resulting in the restored

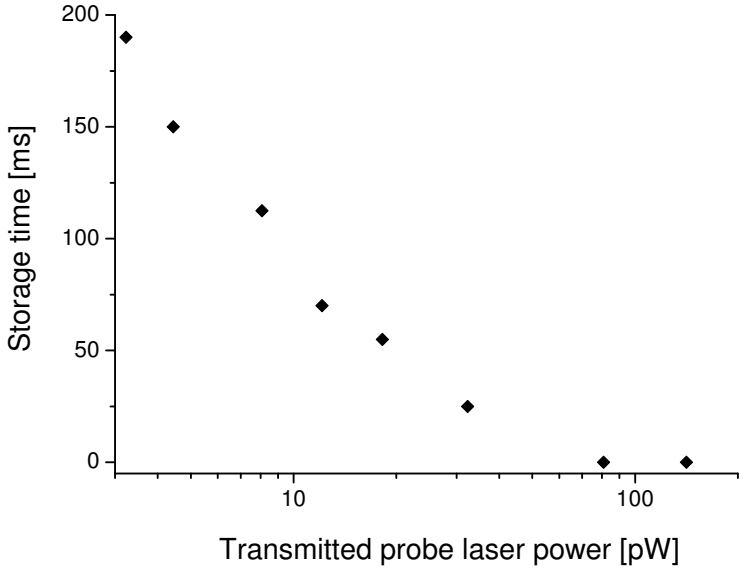

Figure 4.11: Storage time in the cavity depending on probe laser power. The storage time is defined as the time until all atoms are lost. Each point is measured from 20 transmission traces with several tens atoms each.

transmission. After moving the DT back, these atoms can be loaded into the MOT and subsequently detected there.

In order to depopulate the $F=3$ state we apply an additional repumping laser along the DT in the measurement (c). It is derived from the MOT repumper and is resonant with the $F=3 \rightarrow F'=4$ transition. Its power of $0.2\,\mu$W provides an efficient pumping rate while keeping the unwanted light scattering off the cavity mirrors low. Now, the drop in the cavity transmission is more significant compared to that of (b).

4.4.2 Reducing the probe laser power

In spite of the reduced lock laser power, the atoms are nevertheless lost after several milliseconds. Further lowering of the lock power does not improve the situation. Thus, we conclude that the main heating is now induced by a too high power of the probe laser. Despite the Rabi splitting in the coupled atom-cavity system, which shifts the system resonance away from the probe laser frequency, the small fraction of the probe power off-resonantly coupled into the cavity can still affect the atoms and eventually heat them out of the DT.

A straightforward way to increase the lifetime of atoms in the cavity is thus to reduce the power of the probe laser. Figure 4.11 shows the storage time for different powers of the probe laser. Here we define the storage time as the time until *all* atoms are lost and measure it between the transmission drop and its following increase to a half maximum level after averaging over many single traces. Note that in this measurement we have significantly increased the storage time relative to that of Fig. 4.10(c) by using more (about 50) atoms per shot, see next Sec. 4.4.3.

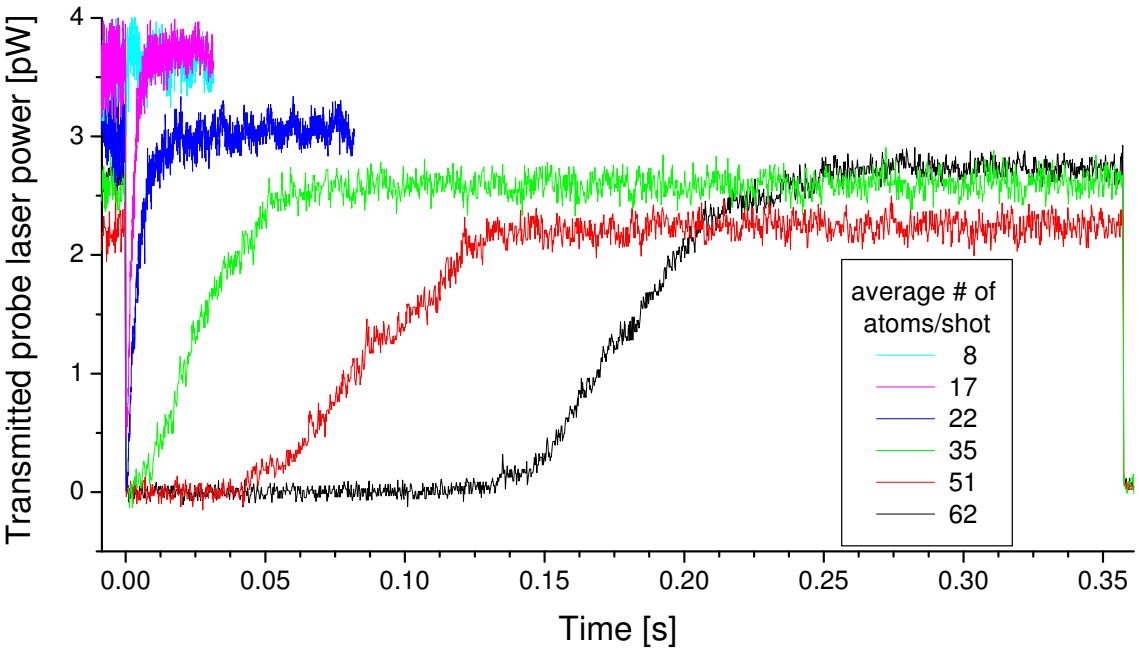

Figure 4.12: Cavity transmission for different numbers of coupled atoms. Each trace is an average over 50 individual measurements resulting in a slow transmission increase instead of an instantaneous one when all atoms are lost. See text for details.

By reducing the probe power, the storage time increases almost exponentially. Since no saturation in the storage time is observed, the probe laser power should be further reduced. However, since the minimal power detectable with the analog APD used here is about 0.5 pW, the use of an even lower probe powers requires a more sensitive light detector. We therefore use a single photon counting module in all measurements described in Sec. 4.5. This allows us to reduce the power of the probe laser by a factor of about 100 and consequently to increase the storage time of single atoms over several seconds, see e.g. Fig. 4.19.

4.4.3 More atoms, longer storage time

According to equation (4.16), the Rabi splitting is larger for a lager number of atoms. Thus, simultaneously coupling more atoms to the cavity mode shifts its resonance further away from the probe frequency resulting in less probe power coupled to the cavity. Consequently, one expects the increase of the storage time of the atoms.

Figure 4.12 shows the cavity transmission measured for different numbers of transported atoms. Each trace presented is an averaged over 50 single measurements. The average number of atoms for the three first measurements was measured as usually from the MOT fluorescence, while in the last three measurements it was estimated from the MOT loading time since the fluorescence from more than about 25 atoms saturates the APD and cannot be measured anymore. Since two-atom losses in the DT are more prob-

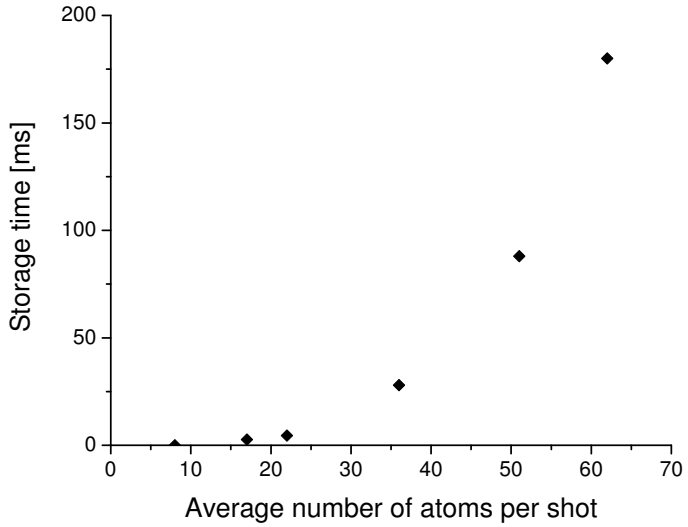

Figure 4.13: Storage time in the cavity depending on the atom number. The observed non-logarithmic dependence shows a collective effect of many atoms which significantly increases their storage time. See text for details.

able when loading more atoms [56], the estimated atom numbers in these measurements can be systematically higher than actual ones by up to 20 %.

The measured dependence of the storage time t_s on the number of atoms initially coupled to the cavity, N_0, is shown in Fig. 4.13. For large N_0, t_s increases steeply and non-linearly. This result is opposite to that of "usual" atom losses where each atom gets lost independent on the current number of trapped atoms. For instance, if the lifetime of atoms is limited by collisions with background gas, which is a probabilistic process, the atom number decays exponentially as $N(t) = N_0 e^{-t/\tau}$ and the time t_s when all atoms are on average lost reads $t_s = \tau \ln N_0$. For the case of the atom losses induced by a heating process [101], see e.g. Fig. 3.16 for the losses due to AOM phase noise, the atom decay can be still approximated by an exponential for large times, thus also leading to the logarithmically dependence of t_s.

The result in Fig. 4.13 looks more like exponential rather than logarithmic dependence. Therefore, we observe that the atoms simultaneously coupled to the cavity collectively protect themselves from quickly being lost. This result agrees with our assumption that the more atoms we couple to the cavity, the less probe power and thus heating they experience.

4.4.4 Multiple transport

In a demonstration experiment performed with many atoms, we shuttle several tens of atoms many times between the MOT position and the cavity mode. The cavity transmission is thereby "switched on and off", see Fig. 4.14. At the end of the sequence all atoms are lost. Note that, during this measurement, the atoms have passed more that 16 cm distance in total, which is indeed a macroscopic distance in atomic physics.

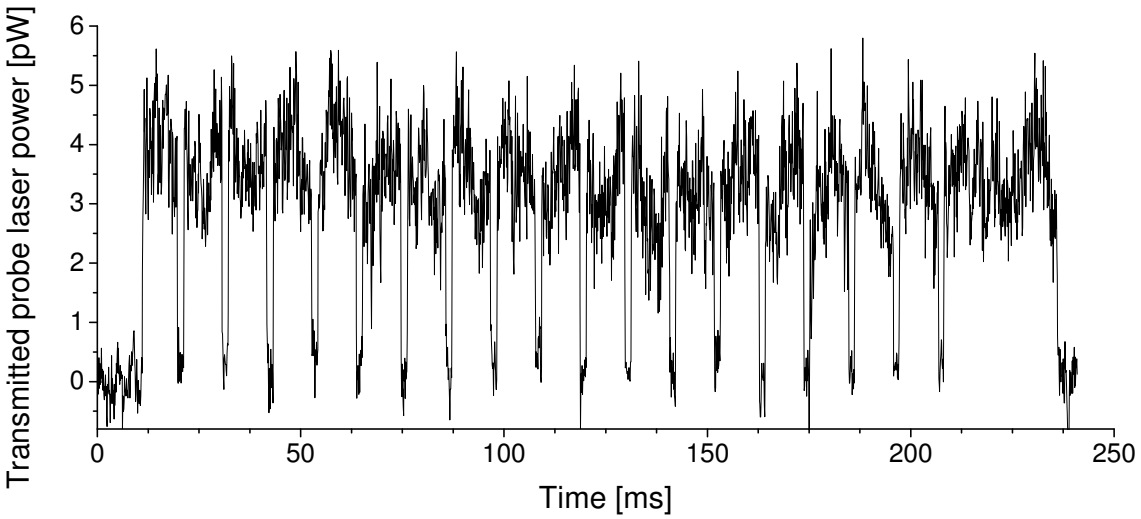

Figure 4.14: Multiple transport of a large number (several tens) of atoms into the cavity. The atoms are shuttled between the MOT position and the cavity mode staying inside the latter for 2 ms. The total transportation distance is about 16 cm.

Summarizing, in the first experiments, carried out with many atoms, we have found out the influence of some important experimental parameters on the lifetime of atoms in the DT while being coupled to the cavity. We have investigated the effect of the probe and lock laser power, of the presence of the repumping laser, and of the number of initially coupled atoms. In order to detect single atoms in the cavity, we have to further reduce the probe laser power and to use a single photon counting detector for observing the cavity transmission. This is realized in the next section where a series of measurements with only *one* atom coupled to the cavity is presented.

4.5 A single atom inside the cavity

In the following, I describe experiments on deterministic transport and coupling of *single* atoms to the cavity mode. The atoms are placed inside the cavity using our precise position control technique. The cavity transmission is detected by a single photon counting module, allowing us to significantly reduce the probe laser power and to avoid the loss of atoms during the measurement. The atom-cavity coupling is indicated by a reduction of the probe transmission.

4.5.1 Probe laser parameters

The main parameters of the probe laser which are of relevance to our experiments are its power, polarization, and detuning from the atomic resonance.

Power

The transmission of the probe laser is detected by the SPCM, see Sec. 3.3.3. The measured optical power is related to the detected count rate, R_{SPCM}, by

$$P_{\mathrm{SPCM}} = R_{\mathrm{SPCM}}\, h\nu_{\mathrm{probe}} \tag{4.33}$$

with ν_{probe} denoting the frequency of the probe laser. According to equation (3.28), the transmitted power is related to the intra-cavity power by the transmission of the cavity mirror T. The detection efficiency of the SPCM, including photon losses in the optical system between the cavity and the detector, is $\eta_{\mathrm{total}} \approx 0.089$, see equation (3.18). Thus, the intra-cavity light power is given by

$$P_{\mathrm{intra}} = \frac{1}{T}\,\frac{R_{\mathrm{SPCM}}\, h\nu_{\mathrm{probe}}}{\eta_{\mathrm{total}}}\,. \tag{4.34}$$

Similarly, we find the intra-cavity photon number of

$$N_{\mathrm{intra}} = \frac{1}{T}\,\frac{R_{\mathrm{SPCM}}\, \tau_{\mathrm{round-trip}}}{\eta_{\mathrm{total}}}\,, \tag{4.35}$$

where $\tau_{\mathrm{round-trip}} = 2L/c$ is the round-trip time in the cavity of a length L.

As an example, 10 kHz count rate of the SPCM corresponds to $P_{\mathrm{intra}} = 80$ nW and $N_{\mathrm{intra}} = 0.09$ photons. Typically, we use probe powers resulting in a detector count rate of 2–6$\times 10^4$ counts/s.

Polarization

The cavity shows birefringence induced by mechanical stress on the glued mirror substrates, see Sec. 3.3.4. The two birefringent modes have linear polarization and are oriented parallel and perpendicular to the cavity holder axis, respectively. All experiments in this chapter have been performed with the probe laser linearly polarized along the DT axis.

Frequency

The probe laser is derived from the MOT cooling laser locked to the $F = 4 \rightarrow F' = 3/5$ crossover transition, see Sec. 3.3.2, and is thus $\Delta_{4\rightarrow 3/5}/2\pi = -226.12$ MHz detuned below the $F = 4 \rightarrow F' = 5$ transition (for cesium level structure see Appendix A). Its frequency is further controlled by two AOMs, see Fig. 3.12, set up in a double-pass configuration. The first modulator, AOM 1, is driven in the -1^{st} diffraction order with a modulation frequency in the range of 80–170 MHz. The second modulator, AOM 3, is driven in the $+1^{\mathrm{st}}$ diffraction order with a frequency of 180–300 MHz. Thus, the combination of the two AOMs allows us to tune the probe laser frequency by $\Delta_{\mathrm{AOM}}/2\pi \approx \pm 200$ MHz about the atomic $F = 4 \rightarrow F' = 5$ transition.

Apart from the laser frequency, the detuning of the probe laser also depends on the exact atomic resonance frequency. In the far-off-resonance dipole trap, the atomic levels

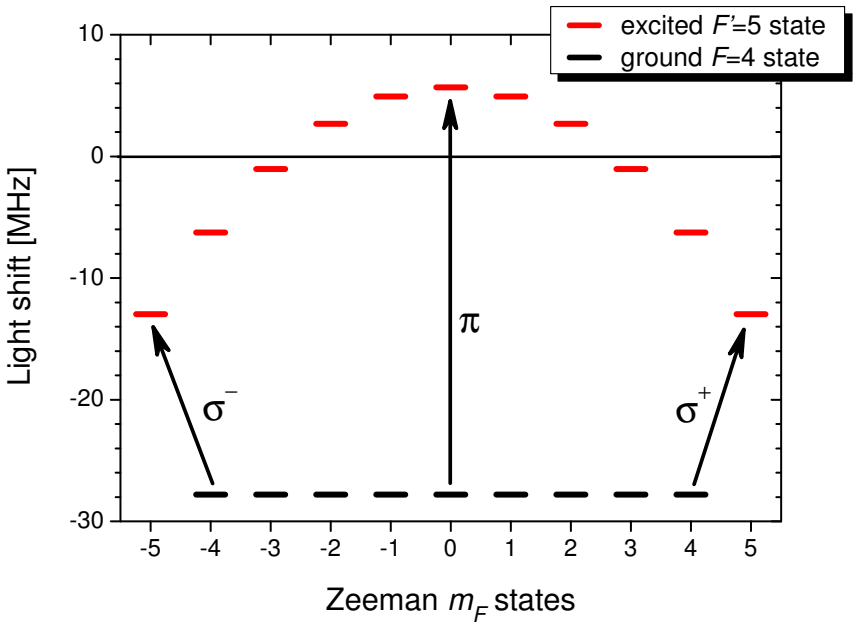

Figure 4.15: Light shift of the atomic excited and ground states in the presence of the linearly polarized DT laser (power of $P_{\mathrm{YAG}} = 3$ W per beam, beam radius of $w_{\mathrm{DT}} = 42\,\mu$m). The strongest σ^-, π, and σ^+ transitions are shown as arrows.

are subject to the ac Stark shift (light shift), see Fig. 4.15. The m_F-dependent shifts for the ground ($F = 4$) and the excited ($F' = 5$) atomic levels are calculated by taking into account the multi-level structure of a cesium atom interacting with a non-resonant classical electro-magnetic field [55, App. A]. The relevant DT parameters used are the power of each DT beam of $P_{\mathrm{YAG}} = 3$ W and the beam radius of $w_{\mathrm{DT}} = 42\,\mu$m.

While the light shift of the Zeeman multiplicity of the ($6S_{1/2}$, $F = 4$) ground state does not depend on the m_F sublevels, the excited ($6P_{3/2}$, $F' = 5$) state is split in m_F due to the coupling to the higher lying S and D states [55]. The light shift $\Delta_{\mathrm{ls}}/2\pi$ of a specific transition is then the difference of the shifts of the corresponding m_F sublevels. The largest shift of -33 MHz is found for the π-transition between the $m_F = 0$ states. The outer-most σ^+- and σ^--transitions have the smallest shift of -15 MHz.

In Ref. [102] a strong m_F- and position dependence of the transition frequency has been avoided by using the state-insensitive trapping of atoms with the DT operating at the "magic" wavelength of 935 nm for cesium. At this frequency, the sum of ac Stark shifts coming from different optical transitions results in the ground $6\mathrm{S}_{1/2}$ and excited $6\mathrm{P}_{3/2}$ states both being shifted downwards by comparable amounts. The dependence on (F', m'_F) is small and thus does not significantly change the atomic frequency.

Summing up the effects given above, the laser detuning from the atomic resonance, $\Delta_{\mathrm{p}} = \omega_{\mathrm{p}} - \omega_{\mathrm{a}}$, is given by

$$\Delta_{\mathrm{p}} = \Delta_{4\to 3/5} + \Delta_{\mathrm{AOM}} + \Delta_{\mathrm{ls}}\,. \tag{4.36}$$

Guiding magnetic field

The orientation of the guiding magnetic field sets the polarization of the probe laser: The linearly-polarized probe laser with a perpendicular magnetic field can induce σ^+- and σ^--transitions at the same time, whereas with a parallel orientation of the guiding field to the light polarization one can drive only π-transitions. Therefore, since the light shift Δ_{ls} is different for different transitions, the frequency detuning Δ_{p} depends on the orientation of the guiding field and on the m_F sublevel occupied.

The occupation of the Zeeman levels depends on the optical pumping caused by the probe laser. For instance, in the case of no Zeeman splitting, the π-light pumps about 34 % of the atomic population into the $m_F = 0$ state and about 24 % into each adjacent $m_F = \pm 1$ state. In contrast, if exposed to the $(\sigma^+ + \sigma^-)$ light, 39 % of the population is concentrated in each outermost Zeeman state. In this way one can calculate the effective light shift averaged over the atomic ensemble. However, since we do not know the real DT power affecting the atoms, the exact calculation of the light shifts in our system will be performed in the future after a more precise characterization of the system.

The atom-cavity coupling rate depends on the Zeeman states first of all because of the m_F dependence of the atom-cavity detuning. In addition, the transition strength defining the coupling rate depends on the specific $m_F \rightarrow m'_F$ transition: The coupling g_0, given by equation (4.22), is calculated for the strongest atomic transition $|F=4,\, m_F=4\rangle \rightarrow |F'=5,\, m'_F=5\rangle$, whereas the coupling for the transition $|F=4,\, m_F=0\rangle \rightarrow |F'=5,\, m'_F=0\rangle$ is $\sqrt{9/5}$ times weaker, see Table A.2 in Appendix A for dipole matrix elements.

Concluding, the orientation of the guiding magnetic field, which defines the polarization of the probe laser and thus the atomic distribution over the m_F states, has a direct influence on the atom-cavity coupling. Such an influence has been indeed experimentally observed in Sec. 4.5.5.

4.5.2 Experimental sequence

A typical experimental sequence for all experiments presented below consists of the following main steps. First, we use our technique of number-triggered loading of the DT in order to trap only one atom [56]. Next, we apply the position control procedure for placing the atom inside the cavity [25]: We take an image of the atom, determine its position in the trap, calculate the distance to the center of the cavity mode, and then transport the atom there. Shortly before the atom is transported, we start to observe the transmission of the probe laser through the cavity. After a fixed observation time (typically 2 s), the dipole trap is moved back to its original position and the second CCD image is recorded. Finally, the surviving atom, if any, is loaded back into the MOT. Thus, during each experiment, we obtain three different types of information on the system: first, the atom's position in the DT before and after transport inferred from the two CCD images; second, transmission of the probe and lock lasers through the cavity detected by the SPCM and the APD, respectively; third, survival of the atom, detected at the end of the sequence in the MOT.

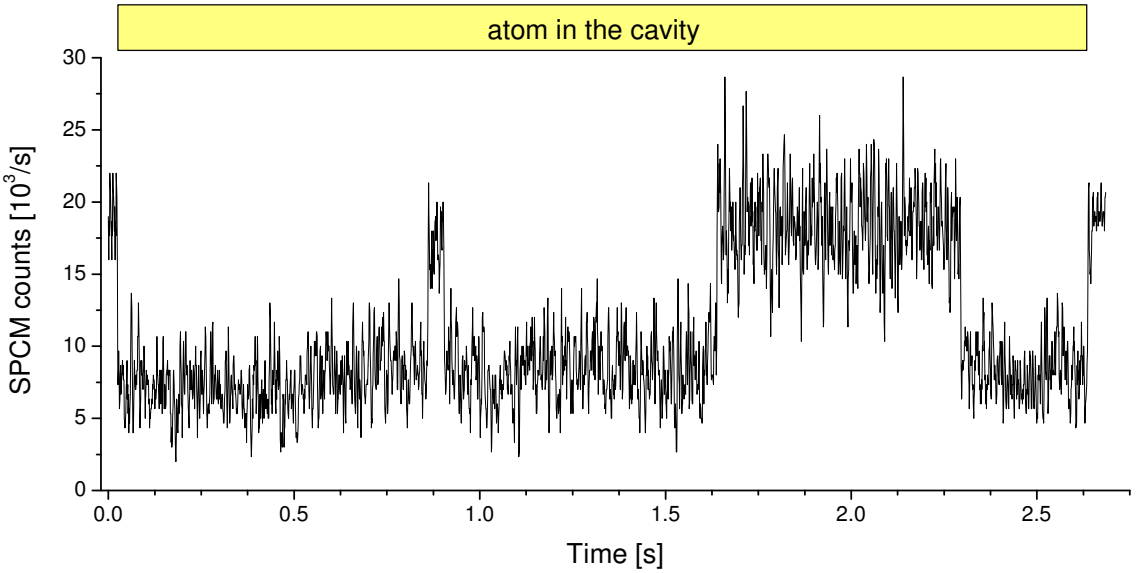

Figure 4.16: The rapid changes of the atom-cavity coupling seen in the cavity transmission signal are assigned to hopping of the atom between potential wells of the DT. The horizontal bar indicates the time when the atom is hold inside the cavity between two transports.

4.5.3 Hopping atoms

A typical cavity transmission signal in the presence of one atom can be seen in Fig. 4.16. Here, the atom enters the cavity at 0.03 s and is removed from the cavity mode at 2.64 s. These events are accompanied with the corresponding decrease and increase of the transmission. Other changes in the cavity transmission indicate rapid changes of the atom-cavity coupling strength which is proportional to the local probe laser intensity seen by the trapped atom. These changes can arise from the atom hopping between different potential wells of our standing-wave DT. Such hopping can move the atom away from or closer to the center of the cavity mode, thus changing its coupling.

The phenomenon of jumping atoms in the DT is often observed in our experiment during their continued imaging with the CCD camera when the illumination of the atoms is not optimal [55]. Any laser cooling process strongly depends on the laser detuning relative to the atomic resonance frequency. If it changes sign, the laser radiation can, e.g., induce heating of the atom instead of cooling. An atom trapped in the dipole potential and oscillating there has a complicated time dependence of the resonance frequency because of the position-dependent ac Stark shift of the atomic levels. Moreover, this variation depends on the atom temperature. Thus, in general, illuminating the atoms in the DT can result in alternating cooling and heating: At some moment the atom can be heated out of the trap and, being still under illumination of the cooling lasers, cooled down again and subsequently recaptured in a different potential well of the DT.

The same effect occurs inside the cavity mode where the probe laser plays a role of the illuminating laser field, although only along one direction. The trapped atom can undergo

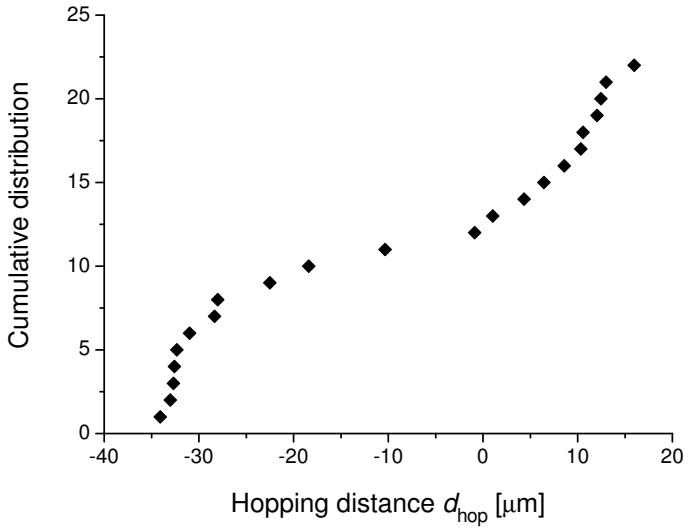

Figure 4.17: Hopping of atoms along the DT. The hopping distance d_{hop} is measured as the difference of the atom position before transporting the atom into the cavity mode and after moving it back by the same transportation distance.

complicated dynamics in the crossed fields of the probe laser and the DT including hopping between DT potential wells. As seen from the transmission traces, see e.g. Fig. 4.16, the atom can hop both into the region of a higher probe laser intensity and of a lower one.

A more direct way to observe the atom hopping is to compare the atom position before transporting it into the cavity mode and after moving it back over the same transportation distance. For this purpose, we measure the hopping distance, d_{hop}, as the difference between the final and initial position of the atom in the DT measured from two CCD images taken at the corresponding instants. Of course, we consider only those experimental shots where the atom is not lost until the end of the sequence, which happens in about 30 % of the cases.

A strong correlation between changes in the cavity transmission and the measured d_{hop} has been observed. If the transmission stays constant during the whole observation time, d_{hop} is always equal to zero within the measurement error. In contrast, Fig. 4.17 shows the cumulative distribution of the measured hopping distances d_{hop} only for the traces where the cavity transmission shows at least one change during the observation time. One can distinguish two regions of the most probable d_{hop}: around about $-30\,\mu$m and $10\,\mu$m, respectively. They are separated by about twice the waist of the cavity mode of $w_0 = 23.2\,\mu$m. We conclude that the atoms hop until they are trapped at the edges of the cavity mode At these points of reduced probe laser intensity, the heating of the atoms and thus their further hopping is suppressed. The asymmetry of the two regions with respect to the zero point can be explained by the unprecise knowledge on the location of the cavity mode along the DT. Indeed, before this set of measurements, we have not precisely located the cavity mode using one of the experimental procedures described in Sec. 4.3.2, but instead we have used an old calibration from a previous measurement day.

As a result, the atoms have been positioned about 10 μm from the center of the cavity mode in the MOT direction.

By performing the same measurements in the absence of the probe laser, we observe neither atom losses nor hopping. Thus, the heating of the atoms in these measurements as well as their subsequent cooling are induced with the assistance of the probe laser.

4.5.4 Influence of the lock laser

In Sec. 4.4.1 we have already seen evidence that the lock laser also affects the atoms placed inside the cavity mode. Below I present a more detailed investigation of these effects.

Dipole interaction

Being resonant with the cavity mode, the lock laser forms a standing wave between the cavity mirrors. Due to its blue detuning with respect to the atomic transition, the lock laser produces a repulsive standing-wave potential, given by equation (1.7), which pushes the atoms away from regions of high laser intensity, i.e. from its antinodes.

The dipole potential along the cavity axis formed by the lock laser and the DT is shown in Fig. 4.18. The slow varying envelope corresponds to the trapping potential of our DT in the vertical (radial) direction along the cavity axis with a width of $w_{\mathrm{DT}} = 42\,\mu$m and a maximum depth of 1.4 mK. This potential is modulated by the repulsive (i.e. positive) standing-wave potential formed by the lock laser. The height of the potential "hills" of $U_{\mathrm{lock}} = 0.8$ mK results from 1.4 μW of coupled lock laser power. Note that the wavelength of the lock laser in the figure is stretched by a factor of 5 to visualize the individual potential hills. From now on, we distinguish three cases: the lock laser dipole potential U_{lock} is smaller, about equal, or larger than the kinetic energy, E_{atom}, of the trapped atom oscillating vertically in the DT. This will define whether the atom will move along the cavity mode quasi-freely or if it will be confined between hills of the repulsive lock laser potential.

Figure 4.19 shows the experimental investigation of the influence of the atom confinement along the cavity axis caused by the lock laser standing wave on the cavity transmission. The lock laser powers coupled into the cavity mode are 0.28 μW (a), 1.4 μW (b), and 2.8 μW (c) producing 160 μK (a), 0.8 mK (b), and 1.6 mK (c) high dipole potential, respectively. The graphs on the left represent typical single transmission traces, while the right graphs are averages over about 20 individual measurements.

If $U_{\mathrm{lock}} < E_{\mathrm{atom}}$, the oscillations along the cavity axis are not suppressed. Then, according to the results of Sec. 4.2.5, the oscillating atom will probe regions of different atom-cavity coupling strength resulting in the measured average transmission which is significantly different from zero. Thus, the reduced, but not completely vanished cavity transmission will stay constant until the atom leaves the cavity.

This case is illustrated in the measurement (a) in Fig. 4.19, where the lock laser produces the dipole potential of a height of 160 μK. All recorded traces show constant transmission levels during the whole observation time until the atom is moved out of the

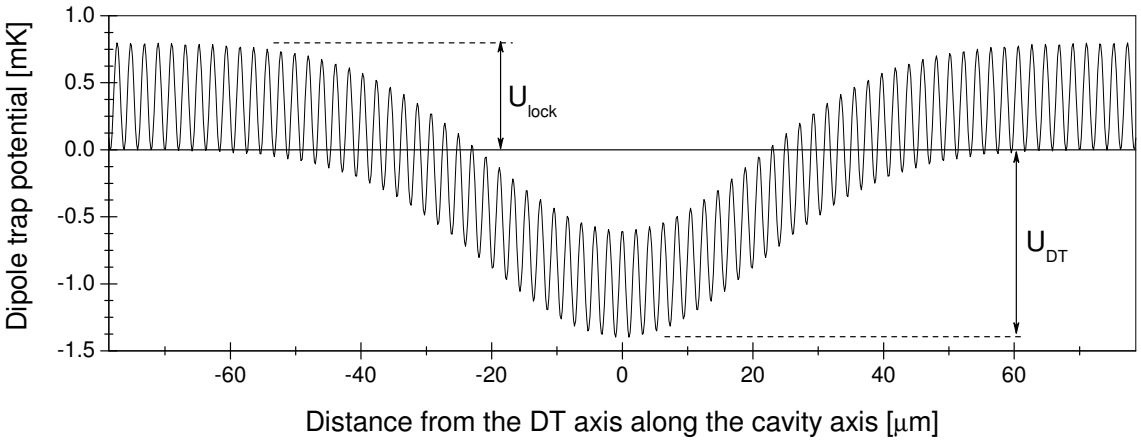

Figure 4.18: Dipole potential formed by crossed DT and lock laser. The wavelength of the lock laser is stretched by a factor of 5 to visualize the individual potential hills.

cavity. Noteworthy, none of them has a transmission lower than about 50 %. Therefore, we conclude that in this case the atomic kinetic energy is higher than the lock laser potential allowing the atom to oscillate along the probe laser standing wave, thus averaging the cavity transmission.

If the kinetic energy of the atom is about the lock laser potential ($U_{\mathrm{lock}} \approx E_{\mathrm{atom}}$), the atoms can hop between the different wells of the lock laser trap. The higher the temperature, the more frequent the hops. This happens because the atom temperature is not a static property, but changes permanently, both increasing and decreasing, depending on many experimental parameters, e.g., local light shift of the atomic transition, the probe laser power, the coupling strength, etc. Similar hops, although between the potential wells of the DT, have been observe before in Sec. 4.5.3.

In measurement (b) of Fig. 4.19 the lock laser potential of about 0.8 mK height which corresponds to the total dipole potential shown in Fig. 4.18. The cavity transmission shows rapid changes, similar to those in Fig. 4.16. However, the second image of the atoms taken after moving them out of the cavity shows no atom hopping along the DT axis. Therefore, the coupling strength changes due to hops of atoms along the cavity axis between different potential wells of the lock laser. Note that the transmission level now varies over a wide range of values from very low to maximum.

Finally, if $U_{\mathrm{lock}} > E_{\mathrm{atom}}$, the lock laser potential prevents the atom from moving along the cavity axis. In the combination with the attractive DT, the resulting potential confines the atoms along the cavity axis to better than $\lambda_{\mathrm{lock}}/2$ – the periodicity of the lock laser standing wave. The local atom-cavity coupling strength seen by an atom confined at the minimum of the lock laser field depends on the local power of the probe laser. Because of the difference in wavelength, the standing waves of the two lasers have different periods. The beat length between them, i.e. the distance between regions of the same phase, is

$$d_{\mathrm{beat}} = \frac{\lambda_{\mathrm{probe}}\lambda_{\mathrm{lock}}}{2(\lambda_{\mathrm{probe}} - \lambda_{\mathrm{lock}})} = 22.3\,\mu\mathrm{m}. \tag{4.37}$$

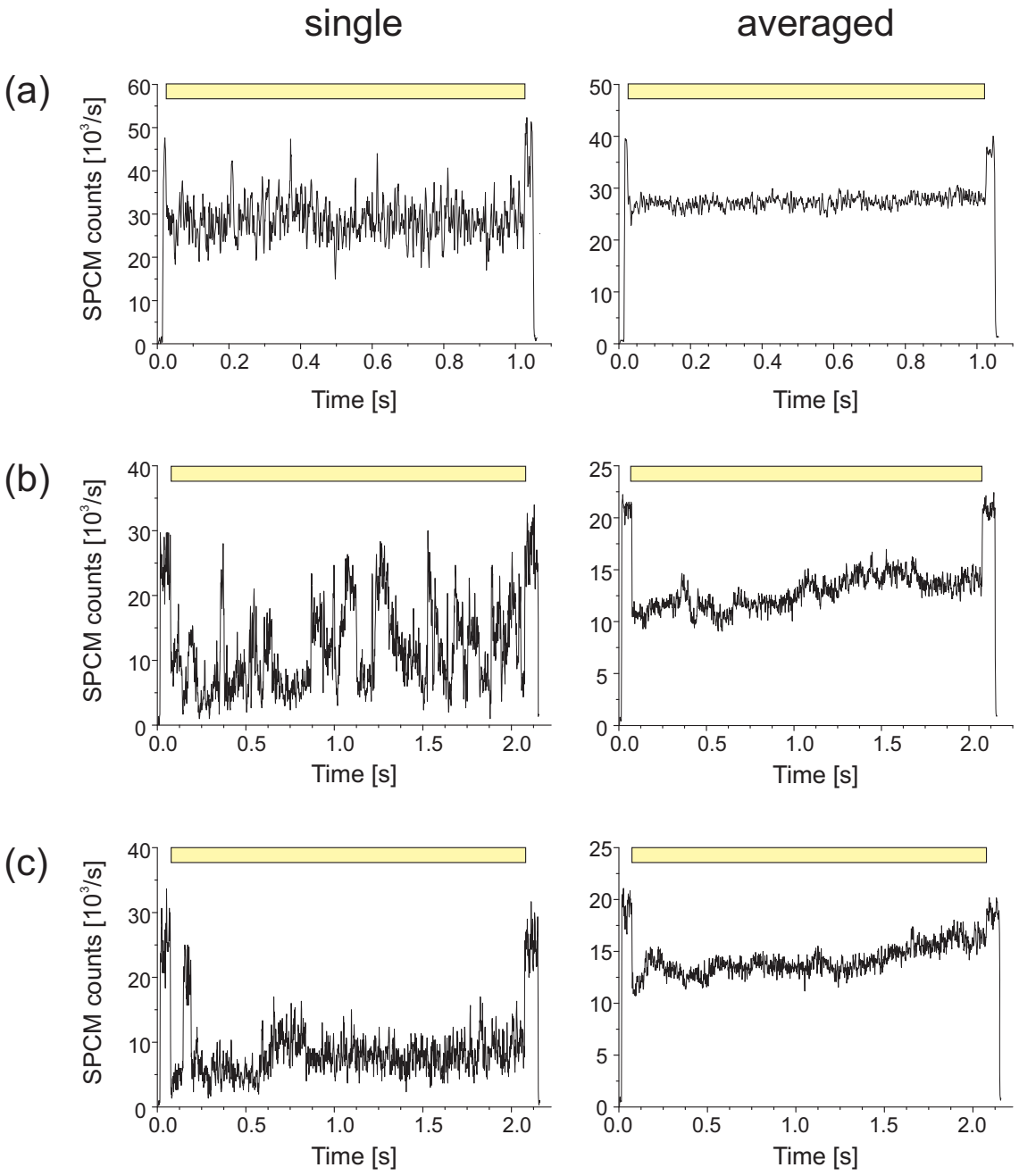

Figure 4.19: Cavity transmission for different powers of the lock laser: 0.28 μW (a), 1.4 μW (b), and 2.8 μW (c) producing a 160 μK (a), 0.8 mK (b), and 1.6 mK (c) high dipole potential, respectively. Left column: typical single traces, right column: averaged traces over about 20 single measurements. Horizontal bars indicate the time between moving an atom into and out of the cavity mode.

Thus, the distance between the regions of the maximum coupling of the confined atom to the cavity field and of no coupling is only $d_{\mathrm{beat}}/2 = 11.2\,\mu$m.

The case of a high lock laser potential is presented in the measurement (c) in Fig. 4.19. Although the hops are still probable (from time to time the atom can gain enough energy from some heating process to hop over the potential wall), they happen less often. For the time being the placing precision of an atom along the cavity axis is low and the atom may end up with different coupling strength to the cavity field. Therefore, any cavity transmission from low to high can be observed if placing the atom into the cavity which is indicated the still relatively hight averaged transmission.

Unfortunately, even higher powers of the lock laser could not be tested because of the significantly increased heating rate of the atoms caused by the lock laser which leads to fast atom loss. Already for the lock laser powers in (b) and (c) the survival probability is about 65 % and 30 %, respectively, measured by loading the surviving atoms back into the MOT at the end of the experimental sequence.

Placement precision

To insure a high coupling, the precision of the placement of an atom into the lock laser standing wave should be much better than $d_{\mathrm{beat}}/2$. This precision is mainly limited by the amplitude of the radial oscillations of atoms in the DT (along the cavity axis), w_{rad}, before entering the cavity mode, see Sec. 4.2.5. For the typical experimental parameters and for the Doppler temperature of atoms, $w_{\mathrm{rad}} \approx 7\,\mu$m which is comparable to the half beat length of $d_{\mathrm{beat}}/2$. Hence, even for perfect alignment of the DT, i.e., with its axis crossing the overlapping antinodes of the probe and lock laser standing waves, the radial oscillation of the atom in the DT will prevent a precise placement into the maximum of the cavity field. Note that the real atom temperature can be significantly higher than the Doppler one due to complicated heating/cooling dynamics of the probe and lock lasers, see Sec. 4.5.3.

The placing precision can be considerably improved by cooling the atom into its ground oscillatory state which has a radial spread of only

$$a_0 = \sqrt{\frac{\hbar}{2m\,\Omega_{\mathrm{rad}}}} = 130\,\mathrm{nm}, \tag{4.38}$$

where the radial oscillation frequency Ω_{rad} is given by expression (1.16). The corresponding cooling, which is also required for many realistic schemes of atom-atom entanglement in a cavity, is one of the next major projects in our group, see Outlook.

A further effect limiting the placing precision is the drifts of the DT position along the cavity axis due to, e.g., thermal drifts of optical elements in the beam path. The standard method to estimate this drift is to regularly take images on the DT loaded with many atoms, sum up the detected fluorescence along the trap axis, and determine the center of the obtained distribution, which gives us the vertical position of the DT axis. Typically these slow drifts are up to 5 μm per hour.

Scattering rate

Apart from the dispersive dipole interaction, the lock laser can also off-resonantly excite atoms. For instance, for an incoming laser power of 1 μW the scattering rate for an atom placed at the field maximum is 24 photons/s, see equation (1.8), and does not depend on the hyperfine ground state. The recoil energy of cesium is $E_{\mathrm{rad}}/k_{\mathrm{B}} = 99$ nK. Therefore, in the absence of all other loss mechanisms, the scattering of the lock laser should result in a lifetime of atoms stored in a 1 mK deep DT of at least several minutes and is thus negligible in our experiments.

Parametric heating of atoms

Although the scattering of the lock laser photons inside the cavity is low, we do observe a strong reduction of the storage time of atoms if using several ten μW of lock laser power or even less. For instance, in the measurement of Fig. 4.19(c) with 2.8 μW laser power, almost all atoms stay trapped inside the cavity for 2 seconds until we move them out of the cavity mode. However, the atoms are always lost if we switch the probe laser off for only 10 ms in this experimental sequence after the atoms are placed inside the cavity. This indicates strong heating of the atoms caused by the lock laser which is counteracted by some cooling mechanism originating from the probe laser.

The observed atom losses are attributed to parametric heating of atoms in the lock laser dipole trap.[2] This heating results from fluctuations of the depth of the lock laser potential appearing at the twice radial oscillation frequency of the DT (typically several kHz). The power fluctuations of the lock laser inside the cavity arise mainly from its fluctuating coupling into the cavity mode due to non-ideal stabilization of the cavity length onto the lock laser. Thus, the parametric heating can be reduced by improving the performance of the cavity stabilization scheme or by reducing the external noise.

4.5.5 Guiding magnetic field

The guiding magnetic field splits the atomic Zeeman levels and determines the quantization axis in the system. The probe laser is linearly polarized along the DT axis in all presented experiments. Thus, recalling Sec. 4.5.1, if the guiding field is applied parallel to the polarization of the probe laser, the laser can induce only π-transitions with $\Delta m_F = 0$, see Fig. 4.15. However, if the quantization axis is perpendicular to the laser linear polarization (e.g., oriented along the cavity or orthogonal to both the cavity and the DT), then both σ^+- and σ^--transitions with $\Delta m_F = \pm 1$ can be induced.

In our experiment the application of guiding fields is accomplished by three orthogonal pairs of coils surrounding the vacuum cell. Typically, we apply magnetic fields of about several Gauss. Figure 4.20 shows cavity transmission signals averaged over 20 single traces for three different orientations of the guiding field. In each trace the atoms enter the cavity mode at 0.075 s indicated by a drop in the detected transmission. After 2 s of observation the remaining atoms are removed from the mode.

[2] For analysis of various heating mechanisms in a dipole trap see Ref. [51].

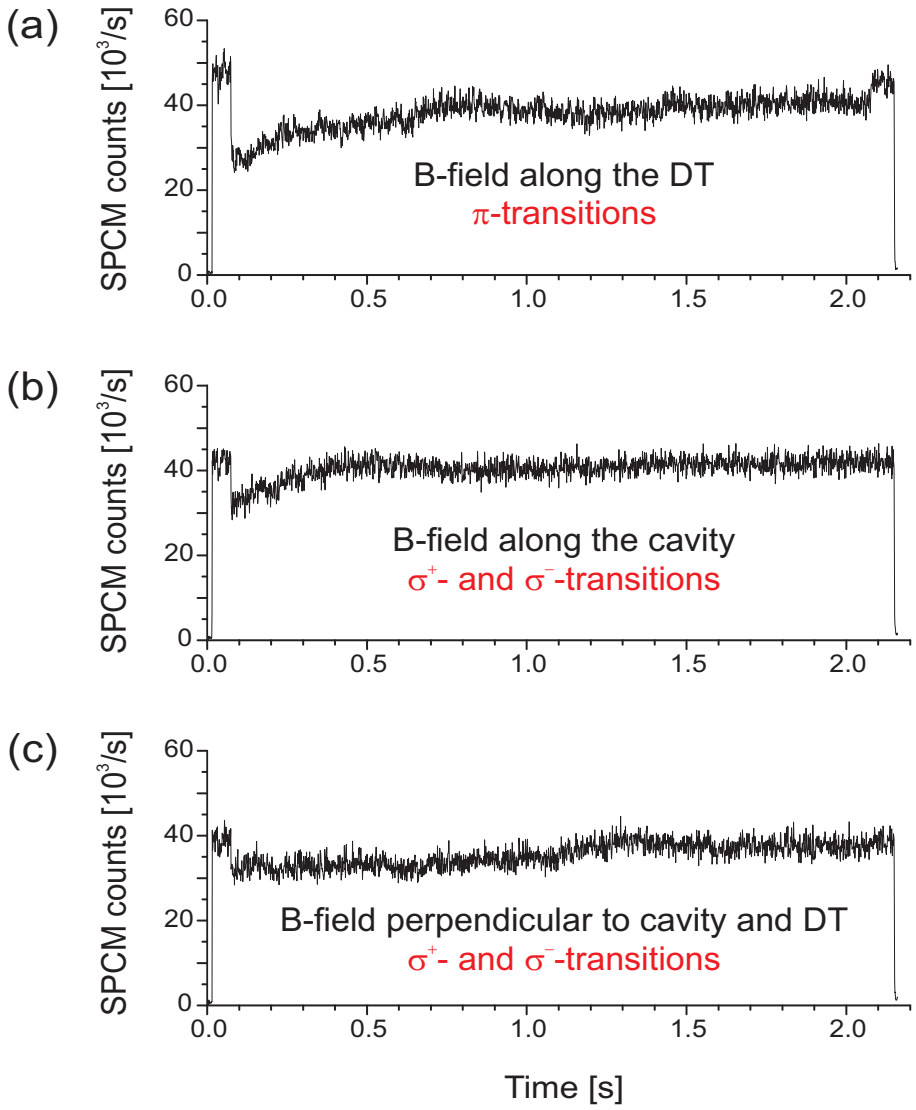

Figure 4.20: Averaged cavity transmission for different orientations of the guiding magnetic field.

The result of measurement (a) with only π-transitions possible differs strongly from other two measurements (b) and (c) where only σ^+- and σ^--transitions can be induced. Note that the strongest π-transition is $\sqrt{9/5}$ times weaker than the strongest σ-transition between outermost Zeeman states (see Table A.2). Thus, we would expect to observe the larger transmission drop for the measurements (b) and (c) compared to (a). This discrepancy can be qualitatively explained by different probe laser detuning for different light polarizations effecting the atom-cavity coupling strength as shown in Fig. 4.15.

The two AOMs in these measurements shift the probe laser frequency by $\Delta_{\mathrm{AOM}}/2\pi = 245$ MHz. Therefore, according to equation (4.36), the probe detun-

ing for the strongest π- and σ-transitions is $\Delta_{\mathrm{p}}^{\pi}/2\pi = -14.5$ MHz and $\Delta_{\mathrm{p}}^{\sigma}/2\pi = 4$ MHz, respectively (see Sec. 4.5.1). One sees that the large detuning $\Delta_{\mathrm{p}}^{\pi}$ should decrease the atom-cavity coupling even further, thus contradicting the results shown in Fig. 4.20. However, in the previous experiments [55] we have observed that due to abberations and diffraction the actual trap depth measured from the oscillation frequencies of the trap can be up to 3.3 times smaller than what we calculate from equation (1.7). If we suppose the real trap depth to be half of the expected one, then the corrected probe detunings are $\Delta_{\mathrm{p}}^{\pi}/2\pi = 2$ MHz and $\Delta_{\mathrm{p}}^{\sigma}/2\pi = 11.6$ MHz. Now, the larger atom-cavity coupling rate for the circularly polarized field can be diminished by the larger detuning from the atomic frequency. A more quantitative analysis of the expected coupling rate should include the atomic populations over m_F levels, the m_F-dependence of the light shifts and of the transition strengths, as well as the experimentally measured dipole trap depth.

4.6 Conclusion

Following significant achievements in controlling single atoms in our standing-wave dipole trap and a successful design, assembly, and stabilization of our high-finesse optical resonator, we are now able to realize deterministic atom-cavity coupling requiring rather complex experimental sequences. A typical sequence includes cooling and trapping of atoms in the MOT, loading them into the dipole trap, transporting over half a centimeter into the cavity mode, probing the atom-cavity system with an external probe laser, and finally moving the remaining atoms back and analyzing them in the MOT.

The first experiments using many atoms helped us to better understand our new system as well as to test the compatibility of different components and techniques. We have analyzed the influence of some important experimental parameters on the lifetime of atoms in the DT coupled to the cavity, mainly of the probe and lock laser power, of the presence of the repumping laser, and of the number of initially coupled atoms.

For coupling and detecting *one* atom in the cavity mode, we have further reduced the probe laser power and used a single photon counting detector for observing the cavity transmission. By means of number-triggered loading of the dipole trap with a single atoms and sub-micrometer position control we prepare and place single atoms into the cavity mode on demand. By observing the cavity transmission we obtain information on the coupling and dynamics in the system. A series of measurements presented shows that we are able to keep single atoms trapped inside the cavity for several seconds. Although the atoms hop inside the mode, their recapture indicates the presence of some cooling mechanisms preventing atom losses and keeping atoms coupled to the cavity.

Chapter 5

Conclusion and outlook

The major achievement of this work is the deterministic coupling of a single atom to the mode of a high-finesse optical resonator. I have presented a set of techniques allowing us to place and hold a single atom inside the cavity mode on demand. The coupling between atom and cavity field manifests itself by a strong reduction of the cavity transmission probed by a weak laser. Moveover, we are able to move the atom out of the cavity and to perform a final state analysis. All these steps are preparatory for deterministic cavity QED experiments with trapped atoms, in particular for possible applications in quantum information processing.

The first part of this thesis was devoted to establishing a sub-micrometer position control of single atoms using our "optical conveyor belt" technique and the fluorescence imaging of trapped atoms. It allows us to place single atoms precisely at the center of a distant cavity mode independently of their initial location in the dipole trap. Next, I have presented the manufacturing, assembly, and test of a miniature ultra-high finesse optical cavity stabilized to the atomic transition. Its properties allow us to optimally integrate the cavity into the present atom-trapping experiment and to operate the atom-cavity system in the strong coupling regime. After transporting a single atom into the cavity, its presence inside the mode is detected as a decrease of the cavity transmission. The atoms stay trapped and coupled to the cavity field for up to 2 seconds until we transport them out of the mode. The basic obstacles preventing the maximal coupling strength have been investigated in a set of experiments presented at the end of the thesis.

Constant coupling

The next main task is to achieve a constant and maximum atom-cavity coupling rate. We have determined that the basic effects reducing the coupling strength are the placing of an atom not precisely at an antinode of the standing-wave field of the cavity mode, the atomic oscillation in the dipole trap transverse to the cavity axis, a time-varying detuning between the cavity resonance frequency and the atomic transition resulting from the position- and m_F-dependent light shift, and driving an atom on all the differently coupled $|F =$

$4, m_F\rangle \rightarrow |F'=5, m'_F\rangle$ transitions. Based on this analysis, we are now planning a set of modifications to our experimental setup. We are still working on improving the relative frequency stability between the cavity and the lock laser. This measure should reduce the intra-cavity power fluctuations of the lock laser which lead to parametric heating of the atoms, and thus should allow us to increase the lock laser power in order to better confine trapped atoms along the cavity axis in order to avoid the oscillating coupling strength. Moreover, better confinement of atoms inside the cavity mode can be achieved by using a more sophisticated geometry of the intra-cavity dipole trap, e.g., by simultaneously using higher transversal modes of the cavity [103].

Spatial filtering of the dipole trap beams by using optical fibers is supposed to reduce heating of the cavity mirrors, thus improving the cavity stability. In addition, optical fibers should provide better pointing stability of the dipole trap leading to a constant trap depth and a reproducible atom-cavity coupling. Next, characterization of our dipole trap should allow us to precisely compensate ac Stark shifts of atomic levels in order to set the right atom-cavity detuning for the future experiments.

Even if the best possible external stability is achieved, one cannot avoid fluctuations of the coupling after inserting a thermal atom into the cavity. Thus the next project is to implement a method of cooling the atoms in the dipole trap and/or in the cavity.

Raman and cavity cooling

By cooling an atom far below the Doppler temperature, we can better localize it at the bottom of a trapping potential well. Besides making the atom-cavity coupling rate more constant, the cooling reduces an undesired variation of the ac Stark shift arising from the atomic thermal motion in the dipole trap. Moreover, some applications in quantum information processing require an atom to be in its oscillatory ground state, which is the ultimate cooling limit in an optical lattice.

Efficient ground state cooling of atoms in optical lattices has been achieved using Raman sideband cooling [104, 105]. We have demonstrated that we can resolve the motional sidebands due to the axial oscillation of the atoms in our dipole trap [100, 106], which is a necessary prerequisite for these cooling schemes to work.

The presence of the cavity mode, which is strongly coupled to the atom and which mechanically affects its motion [107], can give rise to novel cooling mechanisms [108] which are not observed in free space. Such cavity-induced cooling has been demonstrated experimentally in Refs. [102, 109]. The first evidence of a cooling process in our cavity is the recapture of hopping atoms. Presently, possible implementations of cavity cooling schemes are discussed in our group.

Atom-atom entanglement

The generation and the controlled manipulation of an entangled state is an important benchmark for quantum information processing experiments. In a cavity QED system the interaction between two atoms, which is required for their entangling, can be based on

the exchange of a cavity photon. Despite a simple concept and a wide range of possible applications, the entanglement between two ground-state atoms in an optical cavity has not been realized yet.

There are basically three main approaches to entangle atoms in a cavity: deterministic, adiabatic, and measurement-induced. Deterministic entanglement schemes rely on the coherent energy exchange between two atoms simultaneously coupled to the mode of a high-finesse cavity. One of the most promising schemes is based on a resonant four-photon Raman process involving the cavity mode and an auxiliary laser field [110]. However, the best possible fidelity of this scheme for our experimental parameters is at most 85 % under condition of a precise realization of a $\pi/2$ four-photon pulse [55]. In contrast, adiabatic entanglement schemes are not so sensitive to experimental parameters. However, being in general slower than resonant processes, they are still subject to dissipation [111]. A completely different class of entanglement schemes relies on measurement induced entanglement [112, 113], but being probabilistic they are not well suitable for quantum information processing.

Despite recent progress in manufacturing high-quality mirrors, the achievable values of the cooperativity parameter are still too low to permit the high fidelity generation of entangled atomic states with existing proposals. Therefore, we are still seeking for the most promising entanglement scheme that can be implemented in our system.

Appendix A

Atomic data for ^{133}Cs

The most important properties of the cesium atom relevant for this work are summarized in Table A.1, and a level scheme of the first excited states is shown in Fig. A.1. Most of the data is extracted from the data collection of D. Steck [114].

General properties		
Mass	m	2.21×10^{-25} kg
$6^2S_{1/2}$ ground state hyperfine splitting	ω_{hfs}	$2\pi \times 9.1926$ GHz
D_1-line		
Wavelength	λ_{D1}	894.35 nm
Natural lifetime $6^2P_{1/2}$	τ_{D1}	34.9 ns
Decay rate	Γ_{D1}	$2\pi \times 4.56$ MHz
D_2-line		
Wavelength	λ_{D2}	852.11 nm
Natural lifetime $6^2P_{3/2}$	τ_{D2}	30.5 ns
Decay rate	Γ_{D2}	$2\pi \times 5.22$ MHz
Transition dipole matrix element $\langle J = 1/2 \| \| er \| \| J' = 3/2 \rangle$		$4.479\ ea_0$ 3.797×10^{-29} C m
Dipole moment (see Table A.2) $\| F = 4, m_F = \pm 4 \rangle \rightarrow \| F' = 5, m'_F = \pm 5 \rangle$	d	$3.167\ ea_0$ 2.685×10^{-29} C m
Saturation intensity $\| F = 4, m_F = \pm 4 \rangle \rightarrow \| F' = 5, m'_F = \pm 5 \rangle$	I_0	11 W/m^2
Doppler temperature	T_{D}	125 µK
Recoil energy	$E_{\mathrm{rad}}/k_{\mathrm{B}}$	99 nK

Table A.1: Some physical properties of the ^{133}Cs atom.

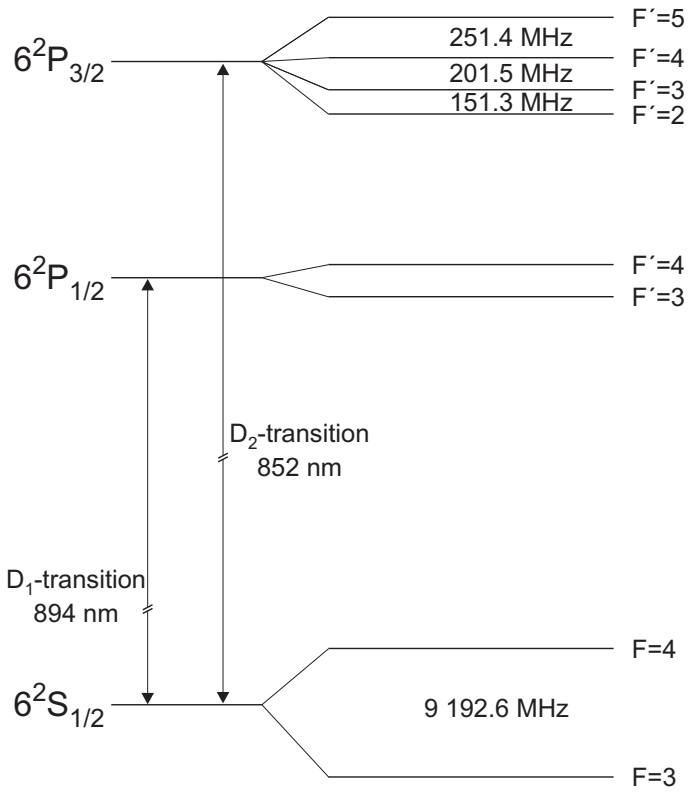

Figure A.1: Level scheme of the first excited states in ^{133}Cs.

The dipole matrix elements for specific $|F=4, m_F\rangle \rightarrow |F'=5, m'_F\rangle$ transitions are listed in Table A.2 as multiples of $\langle J=1/2||er||J'=3/2\rangle = 4.479\, ea_0$ [114]. The transitions $m_F \rightarrow m'_F = m_F$ are coupled by π-polarized light, whereas the transitions $m_F \rightarrow m'_F = m_F + 1$ are coupled by σ^+-polarized light.

	m_F=-4	m_F=-3	m_F=-2	m_F=-1	m_F=0	m_F=1	m_F=2	m_F=3	m_F=4
$m'_F=m_F+1$	$\sqrt{\frac{1}{90}}$	$\sqrt{\frac{1}{30}}$	$\sqrt{\frac{1}{15}}$	$\sqrt{\frac{1}{9}}$	$\sqrt{\frac{1}{6}}$	$\sqrt{\frac{7}{30}}$	$\sqrt{\frac{14}{45}}$	$\sqrt{\frac{2}{5}}$	$\sqrt{\frac{1}{2}}$
$m'_F=m_F$	$-\sqrt{\frac{1}{10}}$	$-\sqrt{\frac{8}{45}}$	$-\sqrt{\frac{7}{30}}$	$-\sqrt{\frac{4}{15}}$	$-\sqrt{\frac{5}{18}}$	$-\sqrt{\frac{4}{15}}$	$-\sqrt{\frac{7}{30}}$	$-\sqrt{\frac{8}{45}}$	$-\sqrt{\frac{1}{10}}$

Table A.2: Dipole matrix elements for $|6^2S_{1/2}, F=4, m_F\rangle \rightarrow |6^2P_{3/2}, F'=5, m'_F\rangle$ transitions in ^{133}Cs, expressed as multiples of $\langle J=1/2||er||J'=3/2\rangle$.

Appendix B

Cavity ringing

When the length of a cavity is scanned faster than the cavity decay time, while being excited by a monochromatic light field, the cavity output shows an amplitude oscillations in its normal decay profile (see Ref. [87] and references therein). This cavity ringing effect can be described classically. For this purpose, we consider the cavity as a damped harmonic oscillator with a time-dependent resonance frequency driven by an external periodic force. The differential equation describing the oscillator's dynamics reads

$$\frac{d^2}{dt^2}E(t) + 2\kappa\frac{d}{dt}E(t) + \omega^2(t)\,E(t) = A\,e^{i\omega_0 t}, \tag{B.1}$$

where κ is the cavity decay rate, $\omega(t)$ is its time-dependent resonance frequency, A and ω_0 are the amplitude and the frequency of an incident laser field, respectively. The intracavity field is given by

$$E(t) = \mathcal{E}(t)\,e^{-i\phi(t)}\,e^{i\omega_0 t} \tag{B.2}$$

with $\mathcal{E}(t)$ denoting the complex field amplitude and $\phi(t)$ denoting the phase. Since the cavity frequency is linearly scanned over ω_0, its frequency and phase can be expressed as

$$\phi(t) = S\,t^2/2 \tag{B.3a}$$
$$\omega(t) = \omega_0 - S\,t. \tag{B.3b}$$

The sweep rate S is defined as $S = \omega_{\mathrm{FWHM}}/\tau_{\mathrm{sweep}}$, where τ_{sweep} is the sweep time through the cavity linewidth. Since ω_{FWHM} is the inverse of the cavity ring-down time, τ_{CRD}, we get $S = (\tau_{\mathrm{sweep}}\ \tau_{\mathrm{CRD}})^{-1}$.

In an approximation of a slowly varying amplitude and phase of the intracavity field compared to ω_0, equation (B.1) can be rewritten as a first-order differential equation

$$\frac{d}{dt}\mathcal{E}(t) + \kappa\,\mathcal{E}(t) = -\frac{i\,A}{2\,\omega_0}\,e^{i\phi(t)}. \tag{B.4}$$

For the initial condition $\varepsilon(t = -\infty) = 0$ the solution to (B.4) reads

$$\mathcal{E}(t) = -\frac{i\,A}{2\omega_0}\int_0^\infty \exp\Big[-i\frac{S(t-\tau)^2}{2} - \kappa\,\tau\Big]d\tau. \tag{B.5}$$

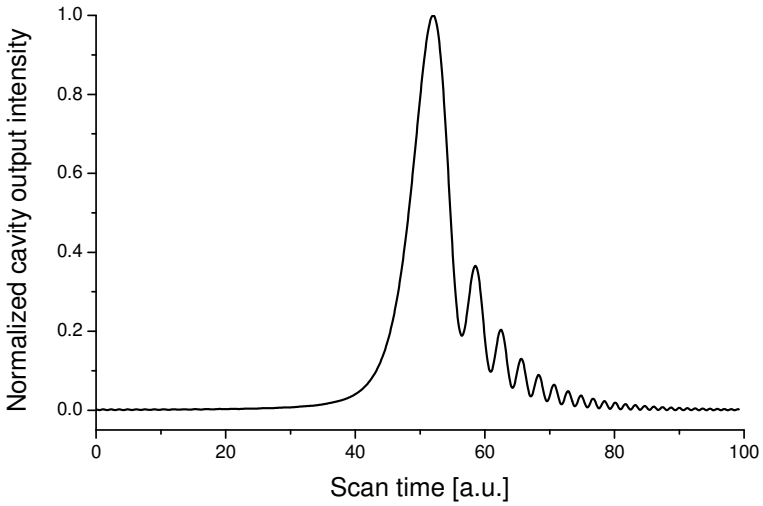

Figure B.1: Theoretical cavity ringing signal. The graph is the solution to equation (B.7) for $\kappa = 1$ and $\tau_{\text{sweep}} = 0.2\,\tau_{\text{CRD}}$.

This integral can be taken analytically in term of the error function[1]

$$\begin{aligned} \mathcal{E}(t) &= -\frac{i\,A}{2\omega_0}\frac{(1-i)\sqrt{\pi}}{2\sqrt{S}}\ \exp\Big[-i\frac{S\,t^2}{2}-i\frac{(\kappa-iS\,t)^2}{2S}\Big]\times \\ &\times \Big(1-\operatorname{erf}\Big[\frac{(1-i)}{\sqrt{S}}(\kappa-iS\,t)\Big]\Big). \end{aligned} \tag{B.6}$$

Finally, the intensity of the intracavity fields is $I(t) = \mathcal{E}^*(t)\,\mathcal{E}(t)$. Since the cavity output is proportional to its intracavity intensity, the cavity ringing signal can be described by

$$I_{\text{out}}(t) = T\,I_0\,\exp(-2\kappa t)\left|1-\operatorname{erf}\Big[\frac{(1-i)}{\sqrt{S}}(\kappa-iS\,t)\Big]\right|^2 \tag{B.7}$$

with $I_0 = (\pi A^2)/(8S\omega_0)$ and T the mirror transmission. The exponential term in (B.7) describes the cavity decay, while the term with the error function represents the cavity ringing, i.e. oscillations with increasing frequency. For $\kappa = 1/(2\tau_{\text{CRD}}) = 1$ and for $\tau_{\text{sweep}} = 0.2\,\tau_{\text{CRD}}$, which seems to be a reasonable proportion for our experiments, the time dependence of the cavity output intensity is shown in Fig. B.1.

[1]The error function is defined as $\operatorname{erf}(x) = 2/\sqrt{\pi}\int_0^x \exp(-t^2)\,dt$.

Bibliography

[1] E. M. Purcell, *Spontaneous transition probabilities in radio-frequency spectroscopy*, Phys. Rev. **69**, 681 (1946)

[2] E. T. Jaynes and F. W. Cummings, *Comparison of Quantum and Semiclassical Radiation Theory with Application to the Beam Maser*, Proc. IEEE **51**, 89 (1963)

[3] J. M. Raimond, M. Brune, and S. Haroche, *Manipulating quantum entanglement with atoms and photons in a cavity*, Rev. Mod. Phys. **73**, 565–582 (2001)

[4] G. Raithel, C. Wagner, H. Walter, L. M. Narducci, and M. O. Scully, *The micromaser: Providing ground for quantum physics*, in P. Berman, ed., *Cavity Quantum Electrodynamics*, p. 57, Academic Press, New York (1994)

[5] R. Miller, T. E. Northup, K. M. Birnbaum, A. Boca, A. D. Boozer, and H. J. Kimble, *Trapped atoms in cavity QED: coupling quantized light and matter*, J. Phys. B: At. Mol. Opt. Phys. **38**, S551–S565 (2005)

[6] G. Rempe, T. Fischer, M. Hennrich, A. Kuhn, T. Legero, P. Maunz, P. Pinkse, and T. Puppe, *Single atoms and single photons in cavity quantum electrodynamics*, in N. P. Bigelow, J. H. Eberly, C. R. Stroud, and I. A. Walmsley, eds., *Coherence and Quantum Optics VIII*, pp. 241–248, Kluwer Academic / Plenum Publishers, New York (2003)

[7] M. A. Nielsen and I. L. Chuang, *Quantum computation and quantum information*, Cambridge University Press (2000)

[8] P. Shor, *Polynomial-time algorithms for prime factorization and discrete logarithms on a quantum computer*, SIAM J. Comp. **26**, 1484 (1997)

[9] L. Grover, *Quantum mechanics helps in searching for a needle in a haystack*, Phys. Rev. Lett. **97**, 325 (1997)

[10] T. Pellizzari, S. A. Gardiner, J. I. Cirac, and P. Zoller, *Decoherence, Continous Observation and Quantum Computing: A Cavity QED Model*, Phys. Rev. Lett **75**, 3788 (1995)

[11] J. I. Cirac, P. Zoller, H. J. Kimble, and H. Mabuchi, *Quantum state transfer and entanglement distribution among distant nodes in a quantum network*, Phys. Rev. Lett. **78**, 3221 (1997)

[12] G. R. Guthörlein, M. Keller, K. Hayasaka, W. Lange, and H. Walther, *A single ion as a nanoscopic probe of an optical field*, Nature **414**, 49 (2001)

[13] J. Ye, D. W. Vernooy, and H. J. Kimble, *Trapping of Single Atoms in Cavity QED*, Phys. Rev. Lett. **83**, 4987 (1999)

[14] S. Nußmann, M. Hijlkema, B. Weber, F. Rohde, G. Rempe, and A. Kuhn, *Submicron Positioning of Single Atoms in a Microcavity*, Phys. Rev. Lett. **95**, 173602 (2005)

[15] C. J. Hood, T. W. Lynn, A. C. Doherty, A. S. Parkins, and H. J. Kimble, *The Atom-Cavity Microscope: Single Atoms Bound in Orbit by Single Photons*, Science **287**, 1447 (2000)

[16] P. W. H. Pinkse, T. Fischer, P. Maunz, and G. Rempe, *Trapping an atom with single photons*, Nature **404**, 365 (2000)

[17] D. P. DiVincenzo, *Quantum Computation*, Science **270**, 255 (1995)

[18] D. Schrader, I. Dotsenko, M. Khudaverdyan, Y. Miroshnychenko, A. Rauschenbeutel, and D. Meschede, *Neutral atom quantum register*, Phys. Rev. Lett. **93**, 150501 (2004)

[19] S. Kuhr, W. Alt, D. Schrader, I. Dotsenko, Y. Miroshnychenko, W. Rosenfeld, M. Khudaverdyan, V. Gomer, A. Rauschenbeutel, and D. Meschede, *Coherence properties and quantum state transportation in an optical conveyor belt*, Phys. Rev. Lett. **91**, 213002 (2003)

[20] H. Mabuchi, Q. A. Turchette, M. S. Chapman, and H. J. Kimble, *Real-time detection of individual atoms falling through a high-finesse optical cavity*, Opt. Lett. **21**, 1393 (1996)

[21] P. Münstermann, T. Fischer, P. W. H. Pinkse, and G. Rempe, *Single slow atoms from an atomic fountain observed in a high-finesse optical cavity*, Opt. Commun. **159**, 63 (1999)

[22] J. A. Sauer, K. M. Fortier, M. S. Chang, C. D. Hamley, and M. S. Chapman, *Cavity QED with optically transported atoms*, Phys. Rev. A **69**, 051804(R) (2004)

[23] S. Kuhr, W. Alt, D. Schrader, M. Müller, V. Gomer, and D. Meschede, *Deterministic delivery of a single atom*, Science **293**, 278 (2001)

[24] D. Schrader, S. Kuhr, W. Alt, M. Müller, V. Gomer, and D. Meschede, *An optical conveyor belt for single neutral atoms*, Appl. Phys. B **73**, 819 (2001)

[25] I. Dotsenko, W. Alt, M. Khudaverdyan, S. Kuhr, D. Meschede, Y. Miroshnychenko, D. Schrader, and A. Rauschenbeutel, *Submicrometer position control of single trapped neutral atoms*, Phys. Rev. Lett. **95**, 033002 (2005)

[26] Y. Miroshnychenko, W. Alt, I. Dotsenko, L. Förster, M. Khudaverdyan, D. Meschede, D. Schrader, and A. Rauschenbeutel, *An atom-sorting machine*, Nature **442**, 151 (2006)

[27] R. Hughes and T. Heinrichs, *A Quantum Information Science and Technology Roadmap, Neutral Atom Approaches to Quantum Information Processing and Quantum Computing* (2004), `http://qist.lanl.gov/pdfs/neutral_atom.pdf`

[28] T. W. Hänsch and A. Schawlow, *Cooling of Gases by Laser Radiation*, Opt. Commun. **13**, 68 (1975)

[29] D. Wineland and H. Dehmelt, *Proposed $10^{14}\Delta\nu < \nu$ Laser Fluorescence Spectroscopy on Tl^+ Mono-Ion Oscillator III (side band cooling)*, Bull. Am. Phys. Soc. **20**, 637 (1975)

[30] S. Chu, L. Hollberg, J. E. Bjorkholm, A. Cable, and A. Ashkin, *Three-dimensional Viscous Confinement and Cooling of Atoms by Resonance Radiation Pressure*, Phys. Rev. Lett. **55**, 48 (1985)

[31] E. L. Raab, M. Prentiss, A. Cable, S. Chu, and D. E. Pritchard, *Trapping of Neutral Sodium Atoms with Radiation Pressure*, Phys. Rev. Lett. **59**, 2631 (1987)

[32] M. H. Anderson, J. R. Ensher, M. R. Matthews, C. E. Wieman, and E. A. Cornell, *Observation of Bose-Einstein condensation in a dilute atomic vapor*, Science **269**, 198 (1995)

[33] K. B. Davis, M. O. Mewes, M. R. Andrews, N. J. van Druten, D. S. Durfee, D. M. Kurn, and W. Ketterle, *Bose-Einstein condensation in a gas of sodium atoms*, Phys. Rev. Lett. **75**, 3969 (1995)

[34] Z. Hu and H. J. Kimble, *Observation of a single atom in a magnetooptical trap*, Opt. Lett. **19**, 1888 (1994)

[35] F. Ruschewitz, D. Bettermann, J. L. Feng, and W. Ertmer, *Statistical investigations on single trapped neutral atoms*, Europhys. Lett. **34**, 651 (1996)

[36] D. Haubrich, H. Schadwinkel, F. Strauch, B. Ueberholz, R. Wynands, and D. Meschede, *Observation of individual neutral atoms in magnetic and magnetooptical traps*, Europhys. Lett. **34**, 663 (1996)

[37] G. A. Askaryan, *Effect of gradient of high-power electromagnetic field on electrons and atoms*, Sov. Phys. JETP **15**, 1088 (1962)

[38] R. Grimm, M. Weidemüller, and Y. B. Ovchinnikov, *Optical dipole traps for neutral atoms*, Adv. At. Mol. Opt. Phys. **42**, 95 (2000)

[39] M. J. Lang and S. M. Block, *Resource Letter: Laser-based optical tweezers*, Am. J. Phys. **71**, 201 (2003)

[40] I. Bloch, *Ultracold quantum gases in optical lattices*, Nature Physics **1**, 23 (2005)

[41] D. Jaksch, *Optical lattices, ultracold atoms and quantum information processing*, Contemp. Phys. **45**, 367–381 (2004)

[42] Masao Takamoto, Feng-Lei Hong, Ryoichi Higashi, and Hidetoshi Katori, *An optical lattice clock*, Nature **435**, 321 (2005)

[43] G. Binnig and H. Rohrer, *In touch with atoms*, Rev. Mod. Phys. **71**, 324 (1991)

[44] W. Neuhauser, M. Hohenstatt, P. Toschek, and H. Dehmelt, *Localized visible Ba^+ mono-ion oscillator*, Phys. Rev. A **22**, 1137 (1980)

[45] Y. Miroshnychenko, D. Schrader, S. Kuhr, W. Alt, I. Dotsenko, M. Khudaverdyan, A. Rauschenbeutel, and D. Meschede, *Continued imaging of the transport of a single neutral atom*, Optics Express **11**, 3498 (2003)

[46] H. J. Metcalf and P. van der Straten, *Laser Cooling and Trapping*, Springer (1999)

[47] V. I. Balykin, V. G. Minogin, and V. S. Letokhov, *Electromagnetic trapping of cold atoms*, Rep. Prog. Phys. **63**, 1429–1510 (2000)

[48] P. D. Lett, R. N. Watt, C. I. Westbrook, W. D. Phillips, P. L. Gould, and H. J. Metcalf, *Observation of Atoms Laser Cooled below the Doppler Limit*, Phys. Rev. Lett. **61**, 169 (1988)

[49] J. Dalibard and C. Cohen-Tannoudji, *Laser cooling below the Doppler limit by polarization gradients: simple theoretical models*, J. Opt. Soc. Amer. B **6**, 2023 (1989)

[50] S. Kuhr, *A controlled quantum system of individual neutral atoms*, Ph.D. thesis, Universität Bonn (2003), available at `http://hss.ulb.uni-bonn.de/diss_online/`

[51] W. Alt, *Optical control of single neutral atoms*, Ph.D. thesis, Universität Bonn (2004), available at `http://hss.ulb.uni-bonn.de/diss_online/`

[52] L. Ricci, M. Weidemüller, T. Esslinger, A. Hemmerich, C. Zimmermann, V. Vuletic, W. König, and T. W. Hänsch, *A compact grating-stabilized diode laser system for atomic physics*, Opt. Commun. **117**, 541 (1995)

[53] W. Alt, *An objective lens for efficient fluoresence detection of single atoms*, Optik **113**, 142 (2002)

[54] J. P. Gordon and A. Ashkin, *Motion of atoms in a radiation trap*, Phys. Rev. A **21**, 1606 (1980)

[55] D. Schrader, *A neutral atom quantum register*, Ph.D. thesis, Universität Bonn (2004), available at `http://hss.ulb.uni-bonn.de/diss_online/`

[56] L. Förster, W. Alt, I. Dotsenko, M. Khudaverdyan, D. Meschede, Y. Miroshnychenko, S. Reick, and A. Rauschenbeutel, *Number-triggered loading and collisional redistribution of neutral atoms in a standing wave dipole trap*, New J. Phys. **8**, 259 (2006)

[57] S. B. Hill and J. J. McClelland, *Atoms on demand: Fast, deterministic production of single Cr atoms*, Appl. Phys. Lett. **82**, 3128 (2003)

[58] N. Schlosser, G. Reymond, I. Protsenko, and P. Grangier, *Sub-poissonian loading of single atoms in a microscopic dipole trap*, Nature **411**, 1024 (2001)

[59] N. Schlosser, G. Reymond, and P. Grangier, *Collisional Blockade in Microscopic Optical Dipole Traps*, Phys. Rev. Lett. **89**, 023005 (2002)

[60] M. Khudaverdyan, W. Alt, I. Dotsenko, L. Förster, S. Kuhr, D. Meschede, Y. Miroshnychenko, D. Schrader, and A. Rauschenbeutel, *Adiabatic quantum state manipulation of single trapped atoms*, Phys. Rev. A **71**, 031404 (2004)

[61] M. Khudaverdyan, *Addressing of individual atoms in an optical dipole trap*, Master's thesis, Universität Bonn (2003)

[62] F. J. Giessibl, *Advances in atomic force microscopy*, Rev. Mod. Phys. **75**, 949 (2003)

[63] K. Suenaga, M. Tenc, C. Mory, C. Colliex, H. Kato, T. Okazaki, H. Shinohara, K. Hirahara, S. Bandow, and S. Iijima, *Element-selective single atom imaging*, Science **290**, 2280 (2000)

[64] G. R. Guthöhrlein, M. Keller, K. Hayasaka, W. Lange, and H. Walther, *A single ion as a nanoscopic probe of an optical field*, Nature **414**, 49 (2001)

[65] A. B. Mundt, A. Kreuter, C. Becher, D. Leibfried, J. Eschner, F. Schmidt-Kaler, and R. Blatt, *Coupling a Single Atomic Quantum Bit to a High Finesse Optical Cavity*, Phys. Rev. Lett. **89**, 103001 (2002)

[66] D. Leibfried, B. DeMarco, V. Meyer, D. Lucas, M. Barrett, J. Britton, W. M. Itano, B. Jelenkovi, C. Langer, T. Rosenband, and D. J. Wineland, *Experimental demonstration of robust, high-fidelity geometric two ion-qubit phase gate*, Nature **422**, 412 (2003)

[67] J. E. Thomas and L. J. Wang, *Absolute frequency measurement of the In^+ clock transition with a mode-locked laser*, Phys. Rep. **262**, 311 (1995)

[68] S. Bergamini, B. Darquié, M. Jones, L. Jacubowiez, A. Browaeys, and P. Grangier, *Holographic generation of microtrap arrays for single atoms by use of a programmable phase modulator*, J. Opt. Soc. Am. B **21**, 1889 (2004)

[69] J.-L. Starck, F. Murtagh, and A. Bijaoui, *Image processing and data analysis*, Cambridge University Press (1998)

[70] M. Bertero and P. Boccacci, *Introduction to inverse problems in imaging*, IOP Publishing Ltd (1998)

[71] W. Falk, *Data reduction from experimental histograms*, Nucl. Instrum. and Methods in Phys. Res. **220**, 473 (1984)

[72] O. Mandel, M. Greiner, A. Widera, T. Rom, T. W. Hänsch, and I. Bloch, *Controlled collisions for multiparticle entanglement of optically trapped atoms*, Nature **425**, 937 (2003)

[73] D. Jaksch, H.-J. Briegel, J. I. Cirac, C. W. Gardiner, and P. Zoller, *Entanglement of Atoms via Cold Controlled Collisions*, Phys. Rev. Lett. **82**, 1975 (1999)

[74] R. Raussendorf and H. J. Briegel, *A One-Way Quantum Computer*, Phys. Rev. Lett. **86**, 5188 (2001)

[75] R. Scheunemann, F. S. Cataliotti, T. W. Hänsch, and M. Weitz, *Resolving and addressing atoms in individual sites of a CO_2-laser optical lattice*, Phys. Rev. A **62**, 51801 (2000)

[76] Y. Miroshnychenko, W. Alt, I. Dotsenko, L. Förster, M. Khudaverdyan, A. Rauschenbeutel, and D. Meschede, *Precision preparation of strings of trapped neutral atoms*, New J. Phys. **8**, 191 (2006)

[77] Y. Miroshnychenko, W. Alt, I. Dotsenko, L. Förster, M. Khudaverdyan, D. Meschede, S. Reick, and A. Rauschenbeutel, *Inserting two atoms into a single optical micropotential*, Phys. Rev. Lett. **97**, 243003 (2006)

[78] P. R. Berman, ed., *Cavity Quantum Electrodynamics*, Advances in atomic, molecular, and optical physics, Academic Press, San Diego (1994)

[79] A. Siegman, *Lasers*, University Science Books, California (1986)

[80] Y. Miroshnychenko, *Design and test of a high finesse resonator for single atom experiments*, Master's thesis, Universität Bonn (2002)

[81] W. Rosenfeld, *A high finesse optical resonator for cavity QED experiments*, Master's thesis, Universität Bonn (2003)

[82] C. J. Hood, *Real-Time Measurement and Trapping of Single Atoms by Single Photons*, Ph.D. thesis, California Institute of Technology, CA (2000)

[83] C. J. Hood, H. J. Kimble, and J. Ye, *Characterization of high-finesse mirrors: Loss, phase shifts, and mode structure in an optical cavity*, Phys. Rev. A **64**, 33804 (2001)

[84] D. Z. Anderson, J. C. Frish, and C. S. Masser, *Mirror reflectometer based on optical cavity decay time*, Appl. Opt. **23**, 1238 (1984)

[85] G. Rempe, R. J. Thompson, H. J. Kimble, and R. Lalezari, *Measurement of ultralow losses in an optical interferometer*, Opt. Lett. **17**, 363 (1992)

[86] T. W. Lynn, *Measurement and Control of Individual Quanta in Cavity QED*, Ph.D. thesis, California Institute of Technology, CA (2003)

[87] J. Poirson, F. Bretenaker, M. Vallet, and A. L. Floch, *Analytical and experimental study of ringing effects in a Fabry-Perot cavity. Application to the measurement of high finesses*, J. Opt. Soc. Am. B **14**, 2811 (1997)

[88] K. An, C. Yang, R. R. Dasari, and M. S. Feld, *Cavity ring-down technique and its application to the measurement of ultraslow velocities*, Opt. Lett. **20**, 1068 (1995)

[89] R. Drever and J. Hall, *Laser phase and frequency stabilization using an optical resonator*, Appl. Phys. B **31**, 97 (1983)

[90] H. Mabuchi, J. Ye, and H. J. Kimble, *Full observation of single-atom dynamics in cavity QED*, Appl. Phys. B **68**, 1095 (1999)

[91] C. Wieman and T. W. Hänsch, *Doppler-Free Laser Polarization Spectroscopy*, Phys. Rev. Lett. **36**, 1170 (1976)

[92] C. P. Pearman, C. S. Adams, S. G. Cox, P. F. Griffin, D. A. Smith, and I. G. Hughes, *Polarization spectroscopy of a closed atomic transition: applications to laser frequency locking*, J. Phys. B: At. Mol. Opt. Phys. **35**, 5141 (2002)

[93] J. R. Buck, *Cavity QED in Microsphere and Fabry-Perot Cavities*, Ph.D. thesis, California Institute of Technology, CA (2000)

[94] H. Carmichael, *An Open Systems Approach to Quantum Optics*, Springer, Berlin (1993)

[95] S. M. Dutra, *Cavity Quantum Electrodynamics*, Wiley-Intersceince (2005)

[96] C. Cohen-Tannoudji, J. Dupont-Roc, and G. Grynberg, *Atom-Photon Interactions: Basic Processes and Applications*, Wiley, New York (1992)

[97] S. Haroche and J.-M. Raimond, *Exploring the Quantum*, Oxford University Press (2006)

[98] M. O. Scully and M. S. Zubairy, *Quantum Optics*, Cambridge University Press, Cambridge (1997)

[99] S. M. Tan, *A computational toolbox for quantum and atom optics*, J. Opt. B: Quant. Semiclass. Opt. **1**, 424 (1999)

[100] I. Dotsenko, *Raman spectroscopy of single atoms*, Master's thesis, Universität Bonn (2002)

[101] M. E. Gehm, K. M. O'Hara, T. A. Savard, and J. E. Thomas, *Dynamics of noise-induced heating in atom traps*, Phys. Rev. A **58**, 3914 (1998)

[102] J. McKeever, J. R. Buck, A. D. Boozer, A. Kuzmich, H.-C. Nägerl, D. M. Stamper-Kurn, and H. J. Kimble, *State-Insensitive Trapping of Single Atoms in an Optical Cavity*, Phys. Rev. Lett. **90**, 133602 (2003)

[103] T. Puppe, I. Schuster, A. Grothe, A. Kubanek, K. Murr, P.W.H. Pinkse, and G. Rempe, *Trapping and observing single atoms in the dark*, arXiv:quant-ph/0702162 (2007)

[104] H. Perrin, A. Kuhn, I. Bouchoule, and C. Salomon, *Sideband cooling of neutral atoms in a far-detuned optical lattice*, Europhys. Lett. **42**, 395 (1998)

[105] S. E. Hamann, D. L. Haycock, G. Klose, P. H. Pax, I. H. Deutsch, and P. S. Jessen, *Resolved Sideband Raman Cooling to the Ground State of an Optical Lattice*, Phys. Rev. Lett. **80**, 4149 (1998)

[106] I. Dotsenko, W. Alt, S. Kuhr, D. Schrader, M. Müller, Y. Miroshnychenko, V. Gomer, A. Rauschenbeutel, and D. Meschede, *Application of electro-optically generated light fields for Raman spectroscopy of trapped cesium atoms*, Appl. Phys. B **78**, 711 (2004)

[107] P. Domokos and H. Ritsch, *Mechanical effects of light in optical resonators*, JOSA B **20**, 1098–1130 (2003)

[108] P. Horak, G. Hechenblaikner, K. M. Gheri, H. Stecher, and H. Ritsch, *Cavity-Induced Atom Cooling in the Strong Coupling Regime*, Phys. Rev. Lett. **79**, 4974 (1997)

[109] P. Maunz, T. Puppe, I. Schuster, N. Syassen, P. W. H. Pinkse, and G. Rempe, *Cavity cooling of a single atom*, Nature **428**, 50 (2004)

[110] L. You, X. X. Yi, and X. H. Su, *Quantum logic between atoms inside a high-Q optical cavity*, Phys. Rev. A **67**, 032308 (2003)

[111] C. Marr, A. Beige, and G. Rempe, *Entangled-state preparation via dissipation-assisted adiabatic passages*, Phys. Rev. A **68**, 033817 (2003)

[112] A. S. Sørensen and K. Mølmer, *Measurement Induced Entanglement and Quantum Computation with Atoms in Optical Cavities*, Phys. Rev. Lett. **91**, 097905 (2003)

[113] J. Metz, M. Trupke, and A. Beige, *Robust Entanglement through Macroscopic Quantum Jumps*, Phys. Rev. Lett. **97**, 040503 (2006)

[114] D. A. Steck, *Cesium D Line Data* (23 January 1998, Revision 1.5, 21 November 2002), `http://steck.us/alkalidata/`

Publications

1. S. Kuhr, W. Alt, D. Schrader, I. Dotsenko, Y. Miroshnychenko, W. Rosenfeld, M. Khudaverdyan, V. Gomer, A. Rauschenbeutel, and D. Meschede, *Coherence properties and quantum state transportation in an optical conveyor belt*, Phys. Rev. Lett. **91**, 213002 (2003)

2. Y. Miroshnychenko, D. Schrader, S. Kuhr, W. Alt, I. Dotsenko, M. Khudaverdyan, A. Rauschenbeutel, and D. Meschede, *Continued imaging of the transport of a single neutral atom*, Optics Express **11**, 3498 (2003)

3. I. Dotsenko, W. Alt, S. Kuhr, D. Schrader, M. Müller, Y. Miroshnychenko, V. Gomer, A. Rauschenbeutel, and D. Meschede, *Application of electro-optically generated light fields for Raman spectroscopy of trapped Cesium atoms*, Appl. Phys. B **78**, 711 (2004)

4. D. Schrader, I. Dotsenko, M. Khudaverdyan, Y. Miroshnychenko, A. Rauschenbeutel, and D. Meschede, *A neutral atom quantum register*, Phys. Rev. Lett. **93**, 150501 (2004)

5. M. Khudaverdyan, W. Alt, I. Dotsenko, L. Förster, S. Kuhr, D. Meschede, Y. Miroshnychenko, D. Schrader, and A. Rauschenbeutel, *Adiabatic quantum state manipulation of single trapped atoms*, Phys. Rev. A **71**, 031404(R) (2005)

6. I. Dotsenko, W. Alt, M. Khudaverdyan, S. Kuhr, D. Meschede, Y. Miroshnychenko, D. Schrader, and A. Rauschenbeutel, *Submicrometer position control of single trapped neutral atoms*, Phys. Rev. Lett. **95**, 033002 (2005)

7. S. Kuhr, W. Alt, D. Schrader, I. Dotsenko, Y. Miroshnychenko, V. Gomer, A. Rauschenbeutel, and D. Meschede, *Analysis of dephasing mechanisms in a standing wave dipole trap*, Phys. Rev. A **72**, 023406 (2005)

8. Y. Miroshnychenko, W. Alt, I. Dotsenko, L. Frster, M. Khudaverdyan, D. Meschede, D. Schrader, and A. Rauschenbeutel, *An atom-sorting machine*, Nature **442**, 151 (2006)

9. Y. Miroshnychenko, W. Alt, I. Dotsenko, L. Förster, M. Khudaverdyan, D. Meschede, S. Reick, and A. Rauschenbeutel, *Inserting two atoms into a single optical micropotential*, Phys. Rev. Lett. **97**, 243003 (2006)

10. L. Förster, W. Alt, I. Dotsenko, M. Khudaverdyan, Y. Miroshnychenko, D. Meschede, S. Reick, and A. Rauschenbeutel, *Number-triggered loading and collisional redistribution of neutral atoms in a standing wave dipole trap*, New J. Phys. **8**, 259 (2006)

Acknowledgements

Many people deserve thanks for their help and support during my research in Bonn. First and foremost, I would like to thank my supervisor, Dieter Meschede, for providing me the opportunity to work on this exciting "single-atoms" experiment and to be a part of his research group. I am also grateful for his being a coordinator of the Bonn International Physics Programme, which gave me a chance to start my scientific career at the University of Bonn. I would like to thank Leonid Yatsenko for his accepting to review my thesis.

I want to sincerely thank our post-docs, Arno Rauschenbeutel and Wolfgang Alt, for their many years of guidance and support, for their supernatural feeling of the experiment, and their detailed answer to any question. I have particularly benefited from working alongside our senior generation of the PhD students: Stefan Kuhr, Wolfgang Alt, and Dominik Schrader. I acknowledge them for the inspiring atmosphere they created while working on the experiment with me, and for immeasurable amount of knowledge, both experimental and theoretical, I have learned from them.

I am grateful to have been a part of "ukrainian mafia" in the institute together with Yevhen Miroshnychenko, Wenja Rosenfeld, and Mika Khudaverdyan. The experiments on position control would be hardly possibly without Yevhen and Mika. My special thanks goes to Wenja for introducing me the cavity stabilization – a large net of wires, BNC cables, and aluminium "black boxes". I appreciate working with Leonid Förster during our experiments on juggling with single atoms.

The cavity results of my thesis could become possible owing to a coordinated team work and a friendly climate reigned in our lab. I thank Mika for his endless patience and optimism, even during the night measurements, when we tried to recognize and imagine the cavity mode in each noisy peak generated by the experiment on random. Who would ever have thought, that over more than a week Igor and Mika would look for the cavity on the wrong site from the MOT? I also deeply appreciate Sebastian Reick for his organization skills, which helped us a lot while opening the vacuum chamber, installing our "baby" inside the glass cell, or simply planning next measurements. Finally, I am thankful to Ariane Stiebeiner for her ability to quickly take the hint of what I am trying to explain during both numerous night measurements and the lab reconstruction. I deeply appreciate criticism and valuable suggestions of Sebastian, Mika, Wolfgang, and

Arno while reading the manuscript of my thesis.

Of course, I would like to thank all other members of the group of Prof. Meschede that I have been fortunate to have constant interaction with during my time here. Special acknowledgement goes to our "support team" – Annelise Miglo, Ilona Jaschke, Fien Latumahina, and Dietmar Haubrich, for their "parental care" of all of us, for their protecting us in the cruel and intricate world of bureaucracy, for providing us a careless place called "the Institute of Applied Physics", where we could concentrate on "building a quantum computer".

And finally, last but not least, I would like to thank my darling wife, Ira, and our daughter, Alyona, for their continuous love, support, and patience during these years.